UNIVERSITY OF READING
Department of Meteorology

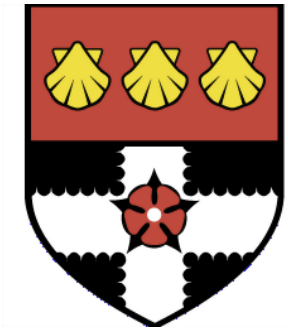

Multi-fluid modelling of dry convection

William Alexander McIntyre

A thesis submitted for the degree of Doctor of Philosophy

March 2020

Declaration

I confirm that this is my own work and the use of all material from other sources has been properly and fully acknowledged.

William A. McIntyre

Abstract

Convection schemes are a large source of error in existing climate and weather prediction models, likely because most schemes are not scale aware and because net mass transport by convection and convective memory are usually ignored. A relatively new approach called the multi-fluid method may be able to address this issue by modelling the convective updraft as a separate fluid from the rest of the atmosphere, allowing convective plumes to be modelled prognostically at any resolution. In this thesis, we investigate the properties of multi-fluid systems and create a 2-fluid model for dry convection where the fluids are defined by the sign of the vertical velocity.

We derive and analyse 20 numerical schemes for transferring mass between fluids (entrainment and detrainment). Two of these schemes, which transfer the mass and fluid properties implicitly, are accurate, bounded, conserve momentum and do not increase the total energy for any timestep. We also extend the stability analysis of Thuburn et al. (2019), who showed that a Kelvin-Helmholtz-like instability exists in the 2-fluid incompressible equations with a shared pressure. By using a pressure perturbation for each fluid proportional to fluid convergence, we show that the instability is significantly suppressed. Moreover, using transfer terms between fluids which are also proportional to convergence, the instability can be removed. We also analyse a high resolution dry convection test case and show that the convergence-based pressure and transfer assumptions are accurate. By using the transfer scheme and fluid pressure anomaly proportional to velocity divergence, the 2-fluid scheme was able to transport heat more effectively than the single-fluid scheme for multi-column grey-zone resolutions. Some errors remain for the multi-column test cases because parameters were tuned for the single-column set-up, for which the 2-fluid scheme is able to accurately model the dry rising bubble test case.

Acknowledgements

I would like to thank my supervisors Hilary Weller and Chris Holloway for all their help and guidance throughout the research project. They have helped me to understand various Meteorological terms, definitions and processes, helped debug countless OpenFOAM applications and have put up with my strange ideas at various times. I would also like to thank my monitoring committee (Bob Plant and Remi Tailleux) for their constructive feedback on my work and progress, and to Dan Shipley and John Thuburn for their thoughts and ideas about developing the multi-fluid model. Thanks also to my office and cohort as our interesting discussions provided valuable insights and ideas. A final thanks to my examiners (Mike Cullen and Remi Tailleux) for dedicating their time to help improve this thesis.

I could not have done this without the support of my family who have always trusted my judgement and have got me to where I am now. The same and more can be said for Emma Jones, who's relentless support has been instrumental in my progress for the past few years. She has always been there for reassurance and advice and has made my life considerably less stressful and more enjoyable throughout the project.

The test case set-ups for the simulations presented in this thesis can be accessed at:
github.com/statisdisc/partitionedShallowWater (Commit: 52422a2)

The source code for the applications used to run the test cases can be accessed at:
github.com/AtmosFOAM/AtmosFOAM-multiFluid (Commit: 92444d3)

Contents

Chapter 1

Introduction

1.1 Overview

The modelling of atmospheric convection is at the forefront of meteorological research due to the large errors caused by current convection schemes (Arakawa, 2004; Holloway et al., 2014; Yano et al., 2018). The inaccurate representation of cumulus convection is responsible for errors in surface temperature distributions, vertical energy transport and the water cycle, including the initiation and location of rainfall (Lean et al., 2008; Lancz et al., 2018). Due to these errors and biases, forecasts of convective rainfall which are more than 1-2 days in advance are typically inaccurate (Yano et al., 2018). It is crucial that convective clouds and their associated couplings are modelled accurately (with fewer assumptions than are currently used) in order to improve weather prediction and climate models (Arakawa, 2004).

The horizontal grid spacing in models has historically been much larger than the length-scales of convection, meaning convection could not be explicitly resolved (Gregory and Rowntree, 1990). Instead, shallow and deep convection are usually parameterised such that the collective effect of clouds within a column is approximated. Although the absence of convection parameterisations can have little effect on the total precipitation in climatological studies (Maher et al., 2018), the modelling of sub-grid convective processes is important for obtaining accurate spacial and temporal distributions of rain. In recent years, we have reached an age in which improved computational power allows convection to be partially resolved (Gerard et al., 2009). However, many assumptions made for parameterisations on large-scale grids become increasingly unrealistic at finer resolutions due to the increased significance of convective processes at smaller scales (Kwon and Hong, 2017) - this is known as the grey zone of convection.

There is thus a demand for a convection scheme which can be used at grey zone resolutions and performs better than the previous mass flux schemes designed for lower resolutions. Although many schemes are aimed at modelling convective processes at grey-zone resolutions (eg. Gerard and Geleyn, 2005; Kwon and Hong, 2017), there is still a need for a convection scheme which treats resolved and sub-grid-scale convection consistently, as most convection schemes do not converge at high resolutions. The

multi-fluid approach, which uses conditional filtering to separate the atmosphere into various fluid components (such as updrafts and downdrafts), is a potential candidate for a scheme which makes few assumptions and is accurate across a large range of resolutions (Thuburn et al., 2018). However, such a scheme is a significant departure from existing parameterisations, as the convection is computed as part of the dynamical core (Weller and McIntyre, 2019) and is not confined to a single vertical column, unlike many traditional mass flux convection schemes (such as Arakawa and Schubert, 1974; Betts, 1986; Gregory and Rowntree, 1990; Lappen and Randall, 2001). As such, an entirely new formulation of the numerics and closures are required to produce a multi-fluid convection scheme.

1.2 Atmospheric convection and the grey zone

1.2.1 What is convection?

Convection is a natural process where mass and heat are transported due to the bulk motion of molecules in response to anomalies in temperature or buoyancy (Schroeder, 2000). In the field of Meteorology, atmospheric convection is more specifically defined as buoyancy-driven circulations due to unstable vertical distributions of mass (Emanuel, 1994). Anomalies in density (ρ) can be used to express the buoyancy (B) for a parcel of air:

$$\boldsymbol{B} = \boldsymbol{g}\frac{\rho_p - \rho_{\text{env}}}{\rho_{\text{env}}} \left(= \boldsymbol{g}\frac{\theta_p - \theta_{\text{env}}}{\theta_{\text{env}}} \text{ for dry air} \right), \tag{1.1}$$

where $\boldsymbol{g}$ is the acceleration due to gravity, θ is the potential temperature and the subscripts represent the parcel (p) and the surrounding environment (env) (Ambaum, 2010). If a parcel of air has positive buoyancy it will rise and if it has negative buoyancy it will fall. For a dry parcel displaced vertically by δz and assuming an ideal gas, the acceleration of the parcel is given by

$$\begin{aligned} \frac{d^2(\delta z)}{dt^2} &= B_z \\ &= -N^2 \delta z, \end{aligned} \tag{1.2}$$

where B_z is the vertical component of the buoyancy, $N^2 = -\frac{g}{\theta_{\text{env}}}\frac{\theta_p - \theta_{\text{env}}}{\delta z}$ and N is known as the Brunt-Väisälä frequency (Ambaum, 2010). Taking the limit where δz and the parcel size tend to 0, we get

$$N^2 = \frac{g}{\theta}\frac{d\theta}{dz}. \tag{1.3}$$

Dry convection will occur if we have a region where $\frac{d\theta}{dz} < 0$ (and therefore $N^2 < 0$) - this means the air is unstable and will rise.

1.2.2 Unstable modes due to dry convection

Equations 1.1 and 1.3 summarise the conditions for when convection should occur, but they do not explain which scales are important when modelling convection. A linear stability analysis of a simplified system can help inform us about which wavemodes grow the fastest in an unstable convective system.

By combining examples from Chandrasekhar (1961), we will consider a system of two incompressible fluids of different densities, with fluid 0 on top of fluid 1 (see figure 1.1). The incompressible, inviscid Navier-Stokes equations are given by

$$\boldsymbol{\nabla}.\boldsymbol{u} = 0 \tag{1.4}$$

$$\frac{\partial \boldsymbol{u}}{\partial t} + \boldsymbol{u}.\boldsymbol{\nabla}\boldsymbol{u} = \boldsymbol{g} - \frac{1}{\rho}\boldsymbol{\nabla} p, \tag{1.5}$$

where $\boldsymbol{u}$ is the velocity, t is the time, $\boldsymbol{g} = -g\hat{\boldsymbol{e}}_z$ is the acceleration due to gravity (and $\hat{\boldsymbol{e}}_z$ is the unit vector in the z-direction), ρ is the density and p is the pressure. For each fluid, the subscript $i = \{0, 1\}$ will be used to label the fluid variables.

The advection term can be rewritten as $\boldsymbol{u}_i.\boldsymbol{\nabla}\boldsymbol{u}_i = \frac{1}{2}\boldsymbol{\nabla}(\boldsymbol{u}_i.\boldsymbol{u}_i) + (\boldsymbol{\nabla} \times \boldsymbol{u}_i) \times \boldsymbol{u}_i$. Assuming that the the flow in each fluid can be approximated by a potential (valid only for small perturbations of the fluid interface, figure 1.1), we can write $\boldsymbol{u}_i = \boldsymbol{\nabla}\Phi_i$ where Φ_i is the velocity potential of fluid i. This means that $\boldsymbol{\nabla} \times \boldsymbol{u}_i = 0$ and that equation 1.5 reduces to

$$\boldsymbol{\nabla}\left[\frac{\partial \Phi_i}{\partial t} + \frac{1}{2}\boldsymbol{u}_i.\boldsymbol{u}_i + gz + \frac{P_i}{\rho_i}\right] = 0 \tag{1.6}$$

$$\frac{\partial \Phi_i}{\partial t} + \frac{1}{2}\boldsymbol{u}_i.\boldsymbol{u}_i + gz + \frac{P_i}{\rho_i} = C, \tag{1.7}$$

where C is a constant and equation 1.7 is the Bernoulli equation for an unsteady potential flow. The mean flow for each fluid is in the x-direction (figure 1.1) such that

$$\boldsymbol{u}_i = \overline{\boldsymbol{u}}_i + \boldsymbol{u}_i' \tag{1.8}$$

$$= \overline{u}_i\hat{\boldsymbol{e}}_x + \boldsymbol{u}_i' \tag{1.9}$$

$$\implies \Phi_i = \overline{u}_i x + \phi_i', \tag{1.10}$$

where $\overline{u}_i = |\overline{\boldsymbol{u}}_i|$, $\hat{\boldsymbol{e}}_x$ is the unit vector in the x-direction and the velocity perturbation

(which is assumed to be small) is given by $\boldsymbol{u}_i' = \boldsymbol{\nabla}\phi_i'$. The mean velocity ($\overline{u}_i$) does not change in time or space but the perturbation velocity ($\boldsymbol{u}_i'$) does. We can therefore linearise equation 1.7 by neglecting second-order perturbation terms such that:

$$\frac{\partial \phi_i'}{\partial t} + \frac{1}{2}\overline{u}_i^2 + \overline{u}_i \frac{\partial \phi_i'}{\partial x} + gz + \frac{P_i}{\rho_i} = C \tag{1.11}$$

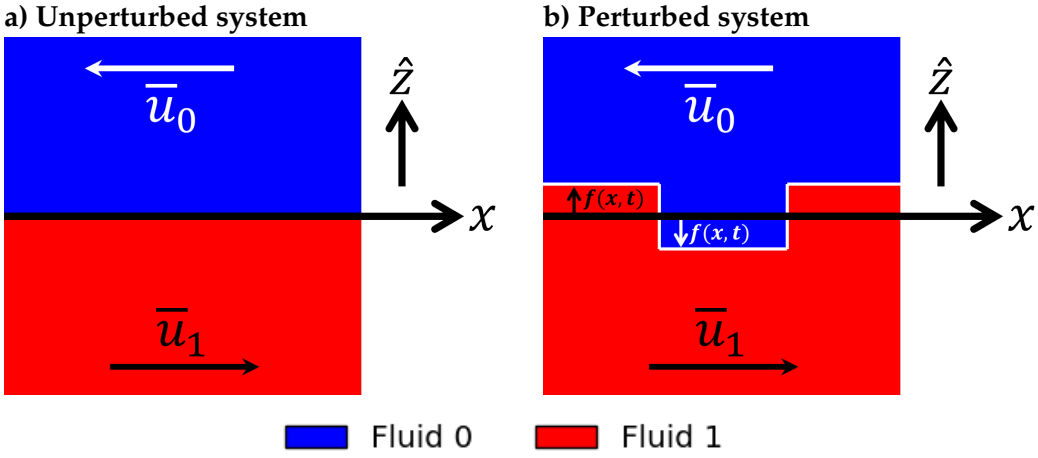

Figure 1.1: A system of two incompressible fluids on top of each other. Each fluid has its own density and velocity. The interface between the fluids is given by $f(x,t)$ which is a small perturbation about $z = 0$.

Let us now consider the boundary between the fluids, which has a height as a function of x and t:

$$z = f(x,t). \tag{1.12}$$

Given that equation 1.11 is constant, we can relate the fluid flow in the perturbed state to the flow when $f(x,t) = 0$:

$$\frac{\partial \phi_i'}{\partial t} + \frac{1}{2}\overline{u}_i^2 + \overline{u}_i \frac{\partial \phi_i'}{\partial x} + gf + \frac{P_i}{\rho_i} = \frac{1}{2}\overline{u}_i^2 + \frac{P_f}{\rho_i} \tag{1.13}$$

$$\implies \rho_i \frac{\partial \phi_i'}{\partial t} + \rho_i \overline{u}_i \frac{\partial \phi_i'}{\partial x} + \rho_i g f + P_i - P_f = 0, \tag{1.14}$$

where P_f is the pressure at the fluid boundary in the unperturbed state. At the fluid interface, the pressure is equal for both fluids ($P_0 = P_1$) which means we can write

$$\rho_0 \frac{\partial \phi_0'}{\partial t} + \rho_0 \overline{u}_0 \frac{\partial \phi_0'}{\partial x} + \rho_0 g f = \rho_1 \frac{\partial \phi_1'}{\partial t} + \rho_1 \overline{u}_1 \frac{\partial \phi_1'}{\partial x} + \rho_1 g f. \tag{1.15}$$

The rate of change of the fluid interface must also be considered:

$$\frac{Dz}{Dt} = \frac{Df(x,t)}{Dt} \tag{1.16}$$

$$\frac{\partial z}{\partial t} + \boldsymbol{u}_i.\boldsymbol{\nabla} z = \frac{\partial f}{\partial t} + \boldsymbol{u}_i.\boldsymbol{\nabla} f \tag{1.17}$$

$$\frac{\partial \phi_i'}{\partial z}\frac{\partial z}{\partial z} = \frac{\partial f}{\partial t} + (\overline{\boldsymbol{u}}_i + \boldsymbol{u}_i').\boldsymbol{\nabla} f. \tag{1.18}$$

Assuming that the fluid boundary perturbation is small, and removing second-order perturbation terms gives

$$\frac{\partial \phi_i'}{\partial z} = \frac{\partial f}{\partial t} + \overline{\boldsymbol{u}}_i \frac{\partial f}{\partial x}. \tag{1.19}$$

There are three equations (1.15 and 1.19) for three unknown perturbation variables (ϕ_0', ϕ_1' and f). One can solve the equation set be assuming solutions in the form

$$\phi_0' \propto G_A(x)G_{B0}(z)G_C(t) \tag{1.20}$$

$$\phi_1' \propto G_A(x)G_{B1}(z)G_C(t) \tag{1.21}$$

$$f \propto G_A(x)G_C(t), \tag{1.22}$$

where G_A, G_B and G_C are functions. Wave-like solutions are assumed such that $G_A(x) = e^{imx}$ and $G_C(t) = e^{-i\Omega t}$, where m is the wavenumber and Ω is the angular frequency. $G_B(z)$ is then constrained by equation 1.4:

$$\boldsymbol{\nabla}.\boldsymbol{u}_i = 0 \tag{1.23}$$

$$\implies \nabla^2 \phi_i' = 0 \tag{1.24}$$

$$\frac{\partial^2 \phi_i'}{\partial z^2} = -\frac{\partial^2 \phi_i'}{\partial x^2} \tag{1.25}$$

$$= m^2 \phi_i', \tag{1.26}$$

meaning that $G_{Bi}(z) = B_{i+}e^{mz} + B_{i-}e^{-mz}$, where B_{i+} and B_{i-} are constants and $|B_{i+}|^2 + |B_{i-}|^2 = 1$. The vertical velocities must tend to zero at the top and bottom boundaries (which adds the constraints $\boldsymbol{u}_0'.\hat{\boldsymbol{e}}_z \to 0$ as $z \to \infty$ and $\boldsymbol{u}_1'.\hat{\boldsymbol{e}}_z \to 0$ as $z \to -\infty$) meaning that $G_{B0}(z) = e^{-mz}$ and $G_{B1}(z) = e^{mz}$ (Taylor, 1950; Chandrasekhar, 1961).

Substituting the wave-like solutions into equations 1.15 and 1.19 results in

$$-i\Omega\rho_0\phi_0' + im\rho_0\overline{u}_0\phi_0' + \rho_0 g f = -i\Omega\rho_1\phi_1' + im\rho_1\overline{u}_1\phi_1' + \rho_1 g f \tag{1.27}$$

$$-i\Omega f + im\overline{u}_0 f = -m\phi_0' \tag{1.28}$$

$$-i\Omega f + im\overline{u}_1 f = -m\phi_1'. \tag{1.29}$$

Eliminating all perturbation terms results in a quadratic equation for the frequency,

$$(\rho_0+\rho_1)\Omega^2 - 2m(\rho_0\overline{u}_0+\rho_1\overline{u}_1)\Omega + \left[m^2(\rho_0\overline{u}_0^2+\rho_1\overline{u}_1^2) + mg(\rho_0-\rho_1)\right], \tag{1.30}$$

where the solution is

$$\Omega = \frac{\rho_0\overline{u}_0+\rho_1\overline{u}_1}{\rho_0+\rho_1}m \pm \sqrt{-\frac{\rho_0\rho_1(\overline{u}_0-\overline{u}_1)^2}{(\rho_0+\rho_1)^2}m^2 - \frac{\rho_0-\rho_1}{\rho_0+\rho_1}mg}. \tag{1.31}$$

Unstable solutions occur when there is an imaginary component of Ω, which results in an exponential growth of the wavemodes with time.

In the case where $\overline{u}_0 \neq \overline{u}_1$ and $(\rho_0-\rho_1)mg = 0$, we obtain the Kelvin-Helmholtz instability which describes the growth of perturbations at the surface of two fluids with wind shear parallel to the boundary (von Helmholtz, 1868; Thomson, 1871; Chandrasekhar, 1961) - this is applicable to the edges of convective updrafts and will be discussed further in chapter 2.

When there is no wind shear, the frequency reduces to

$$\Omega = \overline{u}m \pm \sqrt{-\frac{\rho_0-\rho_1}{\rho_0+\rho_1}mg}, \tag{1.32}$$

which is known as the Rayleigh-Taylor instability when the density of the lower fluid (ρ_1) is smaller than the density of the upper fluid (ρ_0) (Rayleigh, 1882; Taylor, 1950; Sharp, 1983; Youngs, 1989). This is also consistent with the condition for convection described in equation 1.1. The growth rate of the instability is proportional to the square root of the wavenumber (m), meaning that the smallest scale modes (largest m) grow the fastest - this would be the smallest scale available (the grid-scale) in any atmospheric model. The linear instabilities grow exponentially until the interface and velocity perturbations are no longer small relative to the domain and large-scale flow (where the non-linear terms become significant).

In reality, viscous forces are also significant as they suppress the smallest scale modes, resulting in a dominant wavemode which is not the largest scale or the smallest scale (Chandrasekhar, 1961). When modelling dry convection, the grid scale must be smaller than the length scale of the dominant wavemode, in order to prevent unrealistic grid-scale oscillations.

1.2.3 Moist convection and the need for parameterisation

Moist convection is a more complex process than dry convection due to latent heat released by the condensation of vapour into liquid (or ice). As saturated air rises it cools - some of the vapour condenses and releases latent heat, causing the air to cool more slowly than a parcel of dry air. This latent heat release therefore produces warmer air parcels and stronger updrafts - hence the largest convective processes all have saturated levels of moisture within the plumes.

In the atmosphere, moisture-driven convection produces shallow and deep convective clouds. Convective clouds are coupled to various processes in the atmosphere, including vertical momentum, heat and moisture transport, radiative effects and precipitation (Arakawa, 2004; Holloway et al., 2014). Convection is also responsible for large-scale atmospheric circulations (Gregory and Rowntree, 1990) such as mesoscale convective systems ($\sim$ 100 km), tropical cyclones ($\sim$ 1000 km) and the Madden-Julian oscillation ($\sim$ 10,000 km). Deep convection, where the largest convective plumes can reach the tropopause, can also produce extreme weather events such as heavy rain, hail showers and lightning. With such a significant influence on the atmosphere, it is important to have a realistic representation of convection in any weather or climate model.

Atmospheric convection is currently a large source of error in numerical weather prediction (NWP) (Lean et al., 2008; Holloway et al., 2014). This is predominantly due to two factors:

- As convection is coupled to so many atmospheric processes, an error in a convection scheme will produce errors in all of the other processes to which it is coupled.
- The horizontal length scales of shallow and deep convective plumes are $\sim$ 100 m and $\sim$ 1 km respectively. However, the horizontal grid spacing of local and global models is usually in the range of $1 - 100$ km. Given that the resolutions of general circulation models (the smallest scale) are typically larger than the dominant wavemode (the horizontal length scale of convection), the convection will alias onto the grid scale which results in unrealistically large vertical mass fluxes (often referred to as the conditional stability of the second kind which can produce unrealistic grid-point storms: Charney and Eliassen, 1964; Han and Pan, 2011). This is a long-standing issue in convection modelling for local and global forecasts (Betts, 1986; Bechtold et al., 2001; Held et al., 2007). Parameterisations of convection must therefore accurately model sub-grid scale processes in order to remove the unrealistic grid-scale circulations.

Accurate weather or climate models therefore require an accurate convection scheme,

which in turn requires an accurate representation of sub-grid-scale processes.

1.2.4 Modelling sub-grid-scale processes

As the horizontal resolution of models has historically been too coarse to resolve convection, many convection parameterisations attempt to approximate the sub-grid-scale processes including heat fluxes. Sub-grid-scale processes are often modelled using Reynolds averaging which helps to quantify contributions from the resolved and sub-grid-scale variables. Let us consider the budget equation for some mass-weighted variable ϕ in flux form:

$$\frac{\partial \phi}{\partial t} = -\boldsymbol{\nabla}.(\phi \boldsymbol{u}) + f_\phi, \tag{1.33}$$

where $\boldsymbol{u}$ is the velocity and f_ϕ is a source/sink term which may represent a variety of physical processes. We can decompose ϕ into an averaged mean value $\overline{\phi}$ (which could be over time, space or both) and a deviation from the mean ϕ' such that $\phi = \overline{\phi} + \phi'$. This is known as Reynolds decomposition in the time-averaging case (Stull, 1988). Time averaging the velocity gives us $\boldsymbol{u} = \overline{\boldsymbol{u}} + \boldsymbol{u}'$ as well as

$$\frac{\partial(\overline{\phi} + \phi')}{\partial t} = -\boldsymbol{\nabla}.\left(\overline{\phi}\overline{\boldsymbol{u}}\right) - \boldsymbol{\nabla}.\left(\overline{\phi}\boldsymbol{u}'\right) - \boldsymbol{\nabla}.\left(\phi'\overline{\boldsymbol{u}}\right) - \boldsymbol{\nabla}.\left(\phi'\boldsymbol{u}'\right) + f_\phi. \tag{1.34}$$

We Reynolds-average the equation by applying another time average to all terms. By using $\overline{a+b} = \overline{a} + \overline{b}$, $\overline{(\overline{a})} = \overline{a}$, $\overline{a'} = 0$, $\overline{a}\overline{b'} = \overline{a}\overline{b'} = 0$ and assuming the averages are independent of derivatives (Stull, 1988), we get

$$\frac{\partial \overline{\phi}}{\partial t} = -\boldsymbol{\nabla}.\left(\overline{\phi}\overline{\boldsymbol{u}}\right) - \boldsymbol{\nabla}.\left(\overline{\phi'\boldsymbol{u}'}\right) + F_\phi. \tag{1.35}$$

where $F_\phi = \overline{f_\phi}$. The resolved transport of ϕ is represented by the $\boldsymbol{\nabla}.\left(\overline{\phi}\overline{\boldsymbol{u}}\right)$ term whereas $\overline{\phi'\boldsymbol{u}'}$ is a contribution from the sub-grid-scale processes. $\overline{\phi'\boldsymbol{u}'}$ is usually modelled as a term proportional to the gradient of $\overline{\phi}$ when the sub-grid-scale flow is turbulent, which acts to diffuse $\overline{\phi}$ (eddy diffusion; Siebesma et al., 2007).

Although convection is a large source of turbulence, it predominantly acts in the z-direction due to vertical instabilies in the atmosphere. Convective circulations in the atmosphere differ further from turbulence because updraft regions are much narrower (with larger vertical velocities) than downdraft regions or regions of compensating subsidence. Siebesma et al. (2007) note that eddy diffusion is not sufficient to accurately model vertical heat fluxes meaning alternative assumptions (such as convective mass fluxes; Siebesma et al., 2007; Arakawa and Wu, 2013) are needed to model sub-grid-scale convection. Like Reynolds-averaged turbulence, these assumptions and parameterisations are only valid if the circulations are much smaller than the grid scale, which is

assumed in Arakawa and Schubert (1974); Tiedtke (1989); Gregory and Rowntree (1990); Kain and Fritsch (1990), for example.

The problem of modelling sub-grid convection is made more difficult because the resolution of weather prediction models has increased in recent years, to the extent that some of the largest convection-driven circulations are now partially resolved (Yano et al., 2018). This means that convection should be partly represented via both the resolved terms ($\overline{\phi}\overline{\boldsymbol{u}}$) and sub-grid terms ($\overline{\phi'\boldsymbol{u}'}$), but it is not always obvious how much each term should contribute to the overall solution. The convective "grey zone" refers to this transition where horizontal resolution is comparable to the length scales of convection (Holloway et al., 2014). In the grey zone, many parameterisation assumptions used for coarser resolutions are no longer valid and there is a risk of double-counting certain processes which are represented by both the resolved and the sub-grid-scale flow (Arakawa and Wu, 2013).

1.3 Numerical modelling of convection

In this section we summarise some of the most popular convection parameterisation methods of past and present, as well as some new techniques which are currently being developed.

1.3.1 Explicitly resolving convection

Perhaps the most intuitive approach to modelling convection is to explicitly resolve it. Cloud-resolving models (CRMs) or global cloud resolving models (GCRMs) avoid using any convection parameterisations by assuming that the resolved convective circulations are represented by the dynamical core (Satoh et al., 2019). In order to correctly resolve the most prominent features of convective plumes, the grid spacing must be smaller-than (or equal-to) the length-scales of convective clouds ($\sim$ 1 km for deep convection and $\sim$ 100 m for shallow convection) in order to avoid spurious features such as gridpoint storms - but just how fine do resolutions need to be in order to produce accurate statistics and forecasts?

In order to resolve the smallest eddies present in convective clouds, grid spacings down to the Kolmogorov scale would be required (the scale at which viscosity dominates and turbulent kinetic energy is dissipated, of order $\sim$ 1 mm; Landahl et al., 1989; Satoh et al., 2019). However, Mellado et al. (2018) showed that direct numerical

simulations (DNSs) with grid spacings $\Delta x \sim 1$ m were sufficient for representing the entrainment/detrainment at cloud boundaries. These results are promising but current computational capabilities mean that regional or global models with these resolutions are far out of reach (and such high resolution observational data for initialising these simulations does not exist).

For the purposes of representing basic cloud structures, it is often sufficient to use large eddy simulations (LESs) which resolve the largest turbulent eddies present in convective clouds (Satoh et al., 2019). The required resolution for accurate LESs varies between studies; Petch et al. (2002) achieved convergent convective initiation using $\Delta x \sim 100$ m, Matheou et al. (2011) show that convergence of LES schemes is achieved with $\Delta x \sim 20$ m for non-precipitating cases, but Satoh et al. (2019) note that even a spacing of 10 m is not sufficient for modelling more complicated cloud systems. Although large eddy simulations are used to research the properties of convection, these resolutions are still too fine for use in global or regional models.

Several meteorological institutions now use ~ 5 km horizontal grid spacings in their global models or plan to in the near future (Yano et al., 2018); for example, the European Centre for Medium-range Weather Forecast (ECMWF) are aiming for a 5km global resolution by 2025. At these resolutions, deep convection (which has horizontal length scales of ~ 1 km) is partially resolved.

Regional forecasts are computed at finer resolutions than global models. For example, the Meteorological Services of Canada use a 2.5 km resolution over much of Canada (Milbrandt et al., 2016) and the UK Met Office's high resolution model (UKV) runs at 1.6 km (Hanley et al., 2019). At these resolutions significant inaccuracies exist. For example, the UKV currently produces too much heavy rain and not enough light rain (Hanley et al., 2019). Even higher resolutions are being tested with the Met Office's London Model (Boutle et al., 2016) which uses a ~ 300 m resolution over London within a nested suite. Although some institutions are starting to explicitly resolve convection, significant errors and biases still exist meaning convection parameterisations remain a viable alternative.

1.3.2 Adjustment schemes

Some of the earliest attempts to model atmospheric convection involved relaxing grid-scale variables to known stable profiles (Manabe and Strickler, 1964). Known as convective adjustment, these schemes typically adjust the vertical potential temperature and moisture profiles towards pre-defined stable profile shapes over a given timescale (Betts,

1986; Betts and Miller, 1986; Kain and Fritsch, 1990). Excess moisture falls as rain and latent heat warms the temperature profile. This produces a similar effect to convective clouds which also act to stabilise the atmosphere and release latent heat. The simplified equations for convective adjustment typically take the form

$$\frac{\partial \phi}{\partial t} = \frac{1}{\tau}(\phi_S - \phi), \tag{1.36}$$

where ϕ is a grid-scale variable, ϕ_S is the reference profile structure/shape which ϕ tends towards and τ is a timescale related to convective processes. Additional complexity can be added to adjustment parameterisations, as done in the Kain and Fritsch (1990) scheme (later modified in Kain and Fritsch, 1992) which is used in the Canadian High Resolution Deterministic Prediction System (HRDPS) (Milbrandt et al., 2016). Some extra modifications for modelling of deep convection in HRDPS have also been made such as using a smaller cloud radius over oceans to match observations (McTaggart-Cowan et al., 2019).

Convective adjustment schemes are simple to implement and computationally cheap but the behaviour of the schemes are entirely dependent on the chosen relaxation profiles which may not be valid everywhere on the planet. Although adjustment schemes are able to replicate the general tendency of the atmosphere to stabilise (such as adjusting towards a dry adiabat for dry convection), they often fail to produce accurate spacial and temporal distributions of rainfall due to moist convection in both weather and climate forecasts.

1.3.3 Bulk mass flux schemes

Most current convection schemes used in weather prediction are bulk mass flux parameterisations (Plant, 2010), such as Yanai et al. (1973), Tiedtke (1989) and Gregory and Rowntree (1990). Bulk schemes are single-column models which typically assume that many clouds exist per column, but they are modelled as a single entraining-detraining plume (an ensemble). Like all parameterisations, bulk schemes use the grid-scale variables (such as temperature, humidity, velocity and pressure) to deduce the net effect of non-linear sub-grid-scale processes and circulations.

For a mass-weighted variable ϕ in a vertical column, the sub-grid-scale forcing from equation 1.35 is assumed to be $\overline{\phi' w'} = M\phi'/\rho_1$ (the mass flux approximation; Swann, 2001), where w is the vertical velocity, ρ_1 is the density of the updraft and M is the updraft mass flux per unit volume. $\partial\overline{\phi' w'}/\partial z$ is therefore like an additional advection term which transports mass upwards or downwards. Bulk schemes generally use a budget equation

for the total convective mass flux similar to

$$\frac{1}{M}\frac{\partial M}{\partial z} = \epsilon - \delta, \tag{1.37}$$

where z is the height coordinate, ϵ is the fractional entrainment rate and δ is the fractional detrainment rate. The mass flux can be calculated by $M = \sigma_1 \rho_1 w_1$ where σ_1, ρ_1 and w_1 are the area fraction, mean density and mean vertical velocity of the convective updrafts. However, none of these variables are known so M is usually diagnosed using other variables. As the mass flux equation is a differential with respect to z, we only need to know M at one height in order to calculate M everywhere else (if ϵ and δ are defined). Most schemes approximate the cloud-base mass flux for their closure (including Bechtold et al., 2014) but some mass flux schemes use the surface flux (Pergaud et al., 2009). Many schemes calculate the mass-flux closure from the convective available potential energy (CAPE) (such as Bechtold et al., 2014), which is a measure of how much energy a parcel of air would have if allowed to convect. Various other energy and flux-based closures have also been used (eg Arakawa and Schubert, 1974; Pergaud et al., 2009). Note that there is no time-dependence in equation 1.37, meaning the mass flux at one timestep is independent of M at another timestep. If the available energy is close to the level required for triggering convection, mass flux schemes can exhibit intermittent behaviour where the convection scheme switches on and off between timesteps in a non-physical way (Willett and Whitall, 2017).

The form of the fractional entrainment rate (ϵ) for bulk schemes and other mass flux schemes has been the subject of debate of various studies and varies considerably when different assumptions are made. These include:

- $\epsilon \propto \frac{1}{R}$, where R is the plume radius (used in Simpson and Wiggert, 1969; Arakawa and Schubert, 1974; Tiedtke, 1989; De Rooy et al., 2013).
- $\epsilon \propto \rho p$, where p is the pressure (Gregory and Rowntree, 1990).
- $\epsilon \propto \frac{1}{z}$, as often used in the dry convective boundary layer with tuning from LES results (Soares et al., 2004; Siebesma et al., 2007).
- $\epsilon \propto RH$, where RH is the relative humidity (Stirling and Stratton, 2012; Bechtold et al., 2014).
- $\epsilon \propto \frac{B_1}{w_1^2}$, which represents entrainment due to buoyant regions for dry convection (B_1 is the buoyancy of the updraft) (Pergaud et al., 2009).
- $\epsilon \propto \frac{\partial w_1}{\partial z}$, which assumes the convection attempts to maintain its area fraction when accelerating (Houghton and Cramer, 1951, and personal communication

with Whitall, 2017[1]).

Models are extremely sensitive to the value of the entrainment rate (Knight et al., 2007) but there is no unanimous agreement for its functional form. This is because entrainment is a complex process which is completely dependent on the definition of the plume-environment interface (De Rooy et al., 2013) as well as the structure of the plume (Mellado et al., 2018; Satoh et al., 2019). The form of the fractional detrainment rate usually takes a similar functional form to the entrainment rate in models (such as Pergaud et al., 2009), although differences in the properties of moist plumes and the surrounding environment mean that subtle changes are often made (and separate terms are needed for cloud top detrainment).

The simplistic formulation and implementation of bulk schemes has made them popular with model developers, and they are computationally cheap to run. However, bulk mass flux schemes are known to underestimate vertical fluxes of momentum, heat and moisture due to deep convection (Yano et al., 2004). Moreover, by assuming many clouds per column and a small updraft area fraction, the method becomes error-prone when column-widths comparable to the length scales of convective clouds are used. A high spacial resolution is usually accompanied with a small timestep but equilibrium and quasi-equilibrium assumptions are often made in bulk schemes. These assumptions mean that an equilbrium is reached between convection and the large scale flow/forcing within a single timestep or over some timescale (Yano and Plant, 2012) - these assumptions may be valid for large timesteps but become increasingly unrealistic in modern models (Holloway et al., 2014).

1.3.4 Spectral mass flux schemes

Like bulk schemes, spectral schemes also assume many plumes per column but do not model them as a single entraining-detraining plume (Arakawa and Schubert, 1974; Plant, 2010). Instead, a spectral scheme may use several plume types which have different properties (such as shallow vs deep convection). A particular plume type (with subscript i) may have a mass flux budget according to

$$\frac{1}{M_i}\frac{\partial M_i}{\partial z} = \epsilon_i - \delta_i. \tag{1.38}$$

Due to the added complexity of using many plumes, spectral schemes are not as easy to implement as bulk schemes and are more computationally expensive (Gregory and

[1] http://www.ecmwf.int/sites/default/files/elibrary/2017/17786-new-stochastic-scale-aware-convection-scheme-met-office-unified-model.pdf (Accessed: 17/02/2020)

Rowntree, 1990). Entrainment and detrainment rates can have the same functional form as bulk schemes (see section 1.3.3) but can also be tuned to each plume type. Plant (2010) notes that this is one of the key advantages of spectral schemes; by using simple entrainment functions tuned for each cloud type, the total entrainment rate for the column will be a complicated function which is not trivial to model using a bulk scheme. Similar advantages exist with the quasi-equilibrium assumptions, where the timescales can be optimised for each type of convective cloud (Plant, 2010). However, like most mass flux schemes, spectral schemes typically act on a single vertical column and assume compensating subsidence occurs in the same column as an updraft. Spectral schemes are therefore inaccurate in the grey zone.

1.3.5 Eddy diffusivity mass flux schemes

Eddy diffusivity mass flux (EDMF) schemes are an extension of traditional mass flux schemes (Deardorff, 1966) and are often used in the convective boundary layer. Whilst mass flux schemes quantify the net effect of the largest sub-grid eddies and thermals, an eddy-diffusivity approximation can be used to represent the mixing effects due to the smallest turbulent eddies - this contribution is assumed to be diffusive (Deardorff, 1966; Soares et al., 2004; Siebesma et al., 2007). The net effect of the sub-grid contribution therefore becomes

$$\overline{\phi' w'} = - \underbrace{K \frac{\partial \overline{\phi}}{\partial z}}_{\text{Eddy diffusivity}} + \underbrace{\frac{M}{\rho_1}(\phi_1 - \overline{\phi})}_{\text{Mass flux}}, \tag{1.39}$$

where K is a diffusion coefficient which is usually related to the turbulent kinetic energy (Soares et al., 2004) or is instead set to vary with height (Siebesma et al., 2007). An important part of an EDMF scheme is making sure that there is no double-counting between the "ED" and "MF" components of the parameterisation, which can be achieved by using only the strongest updraft regions in the mass flux component.

EDMF schemes have been shown to yield improved transport properties, produce more accurate temperature-velocity covariances in the boundary layer and can be used for multi-plume systems (Siebesma et al., 2007). However, eddy diffusivity schemes do not incorporate net mass transport by convection and, like most mass flux approaches, the schemes do not converge at high resolutions. The EDMF approach has been used at ECMWF (Siebesma et al., 2007) as well as Météo France in the AROME model (Application of Research to Operations at Mesoscale) (Lancz et al., 2018).

1.3.6 Stochastic schemes

Stochastic schemes randomly sample statistical distributions of cloud properties in order to model the variability and interactions of convective processes within a column - in some cases these are calculated using Markov Chain Monte Carlo (MCMC) methods (Khouider et al., 2010). These schemes help to address some limitations of traditional mass flux schemes such as the underestimation of vertical fluxes and intermittency, by sampling a range of possible states within a column. Many different types of stochastic parameterisations exist, such as Plant and Craig (2008) who assume a probability distribution for cloud sizes/strengths, similar to spectral schemes. In the Plant & Craig scheme, the distribution for the cloud base mass flux is given by:

$$P(M)\, dM = \frac{1}{\overline{M}} \exp\left(-\frac{M}{\overline{M}}\right) dM, \tag{1.40}$$

where P is the mass flux probability of a single cloud and $\overline{M}$ is the diagnosed mean mass flux of that particular cloud type. By assuming that the clouds are randomly distributed in space, a mean column mass flux is calculated which can be used as a closure for existing bulk or spectral schemes (Plant and Craig, 2008). By sampling a large range of sub-grid-scale distributions (instead of a single state), stochastic schemes are less likely to be intermittent and can help initiate convection where other methods may fail to do so.

Alternative stochastic methods also exist such as the stochastic multi-cloud model from Khouider et al. (2010), which divides a column into an $N \times N$ lattice, where N is an integer and each lattice point labels a cloud type or clear sky. Each lattice state is given a transition probability to change to a different cloud state which is calculated using MCMC. For example, shallow convection is highly probable at a clear site if there is a large amount of CAPE present, and deep convection can occur if the mid-troposphere is also moist. As well as modelling the convective variability within a column, the scheme can compute area fractions for each cloud type (i) using $\sigma_i = N_i/N^2$, where N_i is the number of lattice elements labelled as cloud type i.

Due to the statistical modelling of variability within a column, stochastic schemes are a potential solution to the grey zone problem. For example, Grell et al. (2014) (which is based on Grell and Dévényi, 2002) propose a stochastic scheme which is scale aware and allows mass transport due to convection between columns. Moreover, the UK Met Office are currently developing CoMorph (personal communication with Whitall, 2017[2]) - a stochastic mass flux scheme which assumes sub-grid-scale variability in the vertical velocity which informs what fraction of an updraft can overcome the energy

[2]http://www.ecmwf.int/sites/default/files/elibrary/2017/17786-new-stochastic-scale-aware-convection-scheme-met-office-unified-model.pdf (Accessed: 17/02/2020)

barrier for convection to occur (convective inhibition, CIN). The scheme assumes a dynamical entrainment rate proportional to $\partial w/\partial z$ and can model shallow convection, deep convection and congestus clouds (like a spectral scheme). Convective clouds can also be initiated at any height.

Although stochastic schemes are more expensive than many bulk and spectral schemes, their improved accuracy often justifies their use. However, stochastic schemes are typically single-column models and do not incorporate net mass transport by convection (Grell et al., 2014, is an exception).

1.3.7 Super-parameterisation

Another technique for representing sub-grid-scale convection is super-parameterisation which involves running high resolution CRMs within each model column (Li et al., 2012). Explicitly resolving the convective circulations is computationally expensive so two-dimensional (2D) models are usually employed for the super-parameterisation, although 3D versions have also been tested (Khairoutdinov et al., 2005). As well as the high spatial resolution, a small timestep is also needed, such as Khairoutdinov and Randall (2001) who use 180 sub-timesteps for each GCM timestep. The high resolution CRM fields are initialised from the coarser GCM prognostic fields. At the end of the CRM simulation, the fields within each GCM column are horizontally averaged and are subsequently used to update the GCM. Similar to some stochastic schemes, super-parameterisation can be used to calculate the updraft area fraction within a column from the high resolution data and can be used to calculate radiative effects and other cloud properties (Khairoutdinov and Randall, 2001).

The super-parameterisation technique is able to accurately simulate the vertical transport properties of convective plumes (Khairoutdinov and Randall, 2001), reproduce large-scale organised convection in the tropics (Khairoutdinov et al., 2005) and accurately model the intensity and spatial distribution of extreme precipitation events (Li et al., 2012). However, the exceedingly high spatial and temporal resolutions mean that super-parameterisations are significantly more expensive than any other convection modelling method we have mentioned, with the exception of a global CRM. Moreover, super-parameterisation acts on each column independently and therefore does not model net mass flux by convection. Given that stochastic schemes such as Khouider et al. (2010) also model columns independently and can approximate cloud area fractions and other cloud statistics at a fraction of the computational cost, it is perhaps more intuitive to use a cheaper parameterisation with a higher resolution GCM.

1.3.8 Machine learning techniques

Machine learning (and deep learning) techniques have recently been considered for improving the representation of sub-grid processes in models (Rasp et al., 2018; Bolton and Zanna, 2019). The method involves using a neural network to learn tendencies and patterns within a large amount of training data and apply the network to a new data set to predict the output. In the case of convection (and once the network is trained), we could ask: "*Given the resolved pressure, temperature and velocity fields, what will be the value of* $\overline{\phi' w'}$*?*" Alternatively, we could simply enter our input fields and receive the convection-adjusted output fields.

The input data and outputs are separated via "layers" of intermediate data points known as "nodes" (Nielsen, 2015). Matrix convolutions are used to calculate the subsequent layers of nodes - the matrix values represent the weights and biases which connect nodes between layers. Figure 1.2 shows a diagram of the layers of nodes/neurons between the input and output data sets.

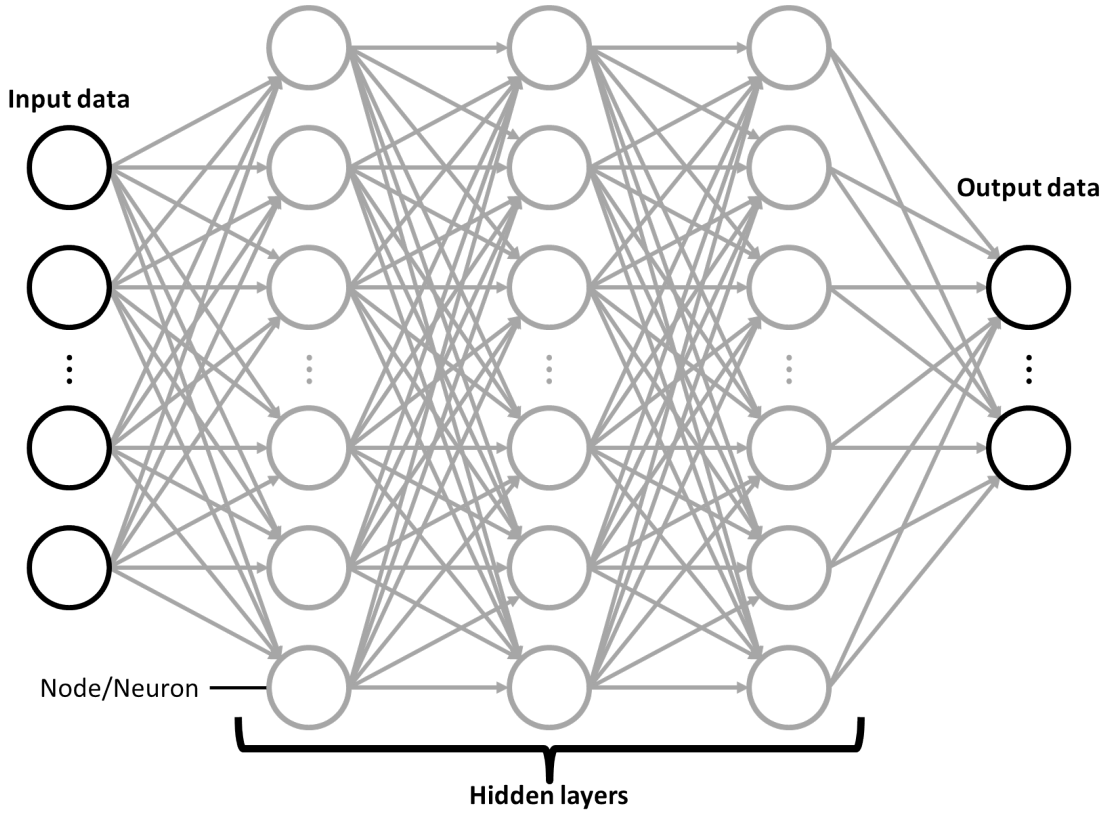

Figure 1.2: A diagram of a neural network which converts input data into an output via matrix convolutions to intermediate (hidden) layers. Each node in one layer is connected to each node in the previous and subsequent layer. The weight of a neuron determines how strongly the nodes are coupled.

For a given training data set, the output can be compared with the observed solution. By calculating the error relative to the observations, the weights and biases can be adjusted to minimise the error - this is known as back-propagation (Nielsen, 2015). Using large sets of training data ensures that the errors are minimised for a large range of scenarios such as moist convection with wind shear and dry conditions, for example.

Machine learning could help to automatically represent processes and phenomena not yet understood or observed as the algorithms will recognise patterns from hundreds or thousands of sets of training data (instead of a handful of test cases analysed by humans). To conduct this analysis, a large amount of computational resources are required. However, once calculated, the convolution matrices are stored and the parameterisation itself is relatively cost-effective to run.

There are some concerns for the use of machine learning in weather or climate modelling:

- As the method works automatically, we have no knowledge of what the algorithm is doing without an extensive analysis of the hidden layers and the convolution matrices.
- The neural network has no concept of physics, meaning properties such as energy conservation may not be obeyed which can be problematic for long-running climatological simulations (Gentine et al., 2018). Energy conservation is also important for model stability and for avoiding overly diffusive solutions in weather and climate forecasts.
- Training data is used to teach the neural network, but how will the scheme react to situations which it has not encountered before (Bolton and Zanna, 2019)? This is a concern for modelling a warmer atmosphere due to climate change.
- Stability issues can arise when coupling a machine learning parameterisation to the dynamical core of a model (Rasp et al., 2018).

Although issues exist, progress has been made in recent years. Bolton and Zanna (2019) used deep learning methods to predict the sub-grid-scale forcing terms for coarse-grained ocean currents. Their methods accurately reproduced conservation properties and low-energy flows when trained on the most turbulent regions, and was also able to predict behaviour at different viscosity settings. However, Bolton and Zanna (2019) did not couple their scheme to the model dynamics.

The deep learning algorithm from Rasp et al. (2018) models sub-grid-scale processes in the atmosphere by learning from super-parameterised simulations. The scheme

was able to approximately achieve moist static energy conservation without prior programming and was able to run in a stable manner when coupled with the dynamical core (but was not able to adapt to different climate conditions). This method could therefore be a cheap alternative to running an expensive super-parameterisation scheme.

O'Gorman and Dwyer (2018) were also successful in stably running a global circulation model (GCM) coupled to a neural network, which was trained with a variant of the Arakawa-Schubert convection scheme (Arakawa and Schubert, 1974). The scheme was energy-conserving and was able to accurately model warmer climates, but training the neural network on parameterisations does not eliminate the existing errors and biases in models.

Another option is to use machine learning to predict the individual closures instead of the whole parameterisation (Schneider et al., 2017). This avoids conservation issues and makes the output of the neural network simpler to analyse.

1.3.9 Summary of existing methods

There are many ways of parameterising convection, many of which approximate the sub-grid-scale terms (such as $\overline{\phi' w'}$). There is currently no convection parameterisation which is accurate and converges to the correct solution in the grey zone, and it is unclear whether such a scheme will be produced before computational resources enable convection to be explicitly modelled in NWP over limited areas.

It is clear that current convection schemes should make fewer assumptions (Arakawa, 2004) and there is some consensus for the features needed for an accurate convection scheme:

- Modern convection schemes should be based on **non-equilibrium** dynamics (Holloway et al., 2014). Equilibrium-based assumptions mean that schemes do not converge to the physical solution for high spacial/temporal resolutions.
- **Net mass transport by convection** is an important process as it distributes mass to neighbouring columns and is a gravity wave source if a plume is of a similar scale to (or larger than) the column width. Most parameterisations are single-column models which assume that convective updrafts are balanced by subsidence in each column which is a poor assumption at grey-zone resolutions. Convection schemes should therefore avoid the single-column assumption.
- Schemes should also ideally use **convective memory** where the convective updraft

properties (such as area fraction, temperature, velocity) are stored from the previous timestep to inform the new fields (such as prognostic schemes). Schemes like Arakawa and Schubert (1974) and Siebesma et al. (2007) instead diagnose these properties independently at each timestep which can lead to intermittency.

- It is also important to have **separate information for the updraft and downdraft** components within a column as the mean grid-box vertical velocity is typically zero for horizontal grid lengths greater than $\sim$ 1 km (Fitch, 2019).
- Convection schemes should be **scale aware** so that they automatically adjust to different resolutions and treat resolved and sub-grid processes consistently (Holloway et al., 2014). Arakawa (2004) notes that traditional cumulus convection parameterisations do not converge at high resolutions due to their statistical, large-scale assumptions and that a completely new framework is required in order produce a scale-aware and consistent scheme.

A convection scheme which can incorporate the above features and is relatively inexpensive to compute may be able to break the convection modelling deadlock.

1.4 Modelling convection with the multi-fluid approach

We have discussed various techniques for modelling and parameterising convection which generally either make the single-column assumption, use too much computational resources, or do not converge in the grey zone. For bulk mass flux schemes in particular, the weaknesses originate from neglecting net vertical mass transport by convection (due to the single-column assumption), neglecting non-equilibrium dynamics, and not incorporating convective memory. It has been proposed that all of these issues can be addressed by using conditional averaging (or conditional filtering) and the multi-fluid approach (Thuburn et al., 2018).

Conditional averaging involves dividing space into various defined fluids (labelled by i) and integrating over these regions (whether it be volume averaging or more complicated techniques) to obtain the fluid properties (Thuburn et al., 2018). In the case of convection, for example, one could use fluid 0 for the neutrally buoyant air, fluid 1 for the convective updraft regions, fluid 2 for the downdraft regions (see figure 1.3). Each fluid has its own properties such as volume fraction, density, temperature and velocity, and by calculating these fields prognostically we can model the sub-grid-scale convection at any resolution - this is the multi-fluid approach.

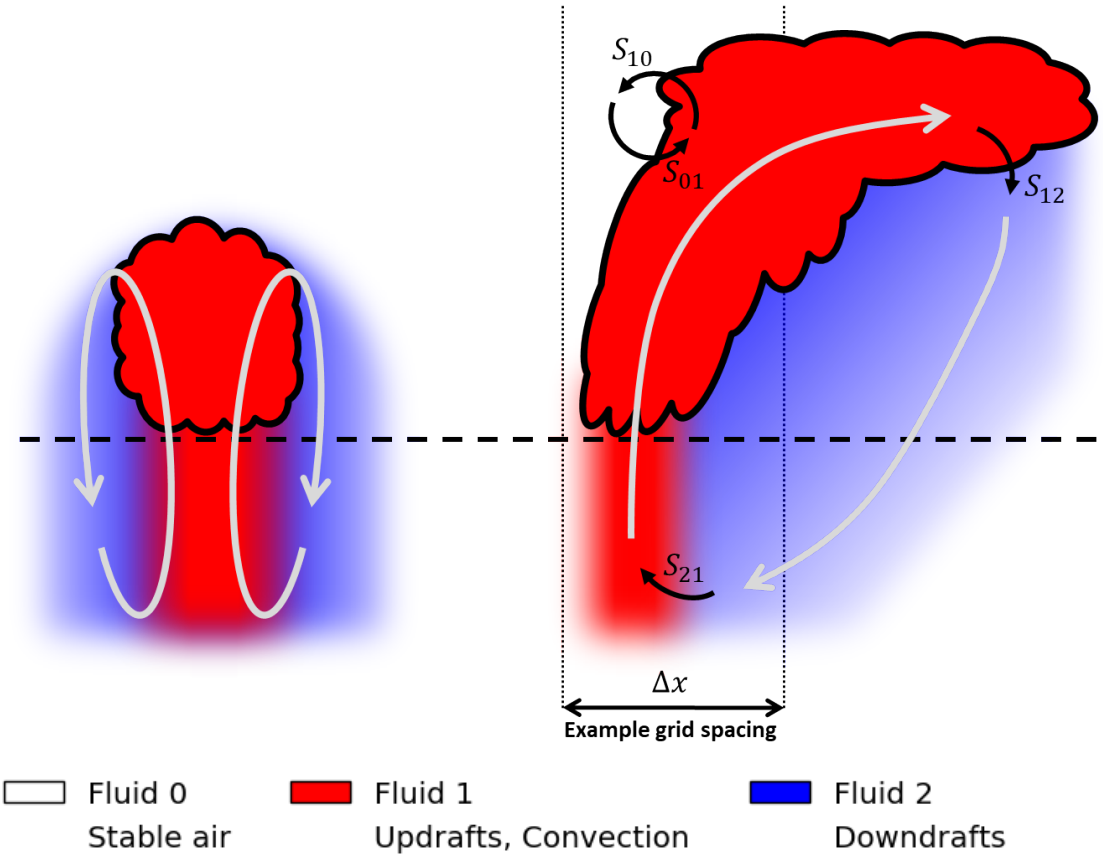

Figure 1.3: The multi-fluid approach aims to model the convective updrafts as a separate fluid (fluid 1 in sketch) from the surrounding environment (fluid 0) and downdrafts (fluid 2). The solid black lines indicate cloud boundaries and the dashed line represents the condensation level. S_{ij} represents the transfer rate of fluid i to fluid j. The multi-fluid method should allow convection to transport mass vertically and between neighbouring columns (which have a horizontal grid spacing Δx), unlike most conventional parameterisations which are single-column models.

Conditional filtering has already been used in various fields of science and engineering. Dopazo (1977) used conditional averaging for modelling turbulent flows and Lappen and Randall (2001) used the technique to model cumulus convection, using an updraft fluid and an environment fluid. However, the environmental fluid in that study was assumed to subside in the same column as the updraft, meaning the scheme does not incorporate net vertical mass transport by convection. The multi-fluid approach has also been used in engineering fields such as Guelfi et al. (2007) who model a veriety of flows for nuclear thermal hydraulics, Méchitoua et al. (2003) who use the technique to simulate vapour-and-water flows in hot reactor pipes and Baer and Nunziato (1986) who use a multi-phase model to simulate explosions. Although numerical schemes are given in some of the above examples, there is little discussion of the behaviour of their numerical implementation including their stability, boundedness and conservation properties.

More recently, Thuburn et al. (2018) described how to conditionally filter the fully compressible Euler equations with the aim of representing sub-grid-scale convection (and conservation properties were derived in Thuburn and Vallis, 2018). However, no transfer terms between fluids were included and no numerical method was given. Tan et al. (2018) present similar equations in their "Extended EDMF" with transfer terms and closures for resolved and sub-grid scale quantities. However, they make various assumptions such as neglecting horizontal variations in density and assuming no turbulent fluctuations in the updraft or downdraft fluids. Tan et al. (2018) also do not include net mass transport by convection in their numerical model, as they solve their equations in a single column.

Following Thuburn et al. (2018), a fluid (i) is labelled at a point in space using I_i which is equal to 1 when fluid i is present and 0 when it is not. In this thesis, we will model dry convection with two fluids, where one fluid is descending or stationary (fluid 0), and the other fluid is rising (fluid 1). The fluid labels are therefore defined as

$$I_0 = \begin{cases} 1 \text{ for } w \leq 0 \\ 0 \text{ for } w > 0 \end{cases} \tag{1.41}$$

$$I_1 = 1 - I_0, \tag{1.42}$$

where w is the vertical velocity. A filter could also be chosen based on buoyancy, for example. In the case of moist convection, the filter could also be based on moisture in order to capture convective plumes, as in Couvreux et al. (2010) and Efstathiou et al. (2019).

The variables/fields (ϕ) are averaged such that

$$\widetilde{\phi}(\boldsymbol{x}) = \int_V G(\boldsymbol{x} - \boldsymbol{x}')\, \phi(\boldsymbol{x}')\, d\boldsymbol{x}', \tag{1.43}$$

where $\boldsymbol{x}$ is the spacial vector, V is the volume to be integrated, G is the filter ($G = 1/V$ within the volume V for volume averages) and the $\widetilde{\text{tilde}}$ denotes that the filter has been applied. If ϕ is proportional to the fluid label I_i (for example, $\phi = \kappa I_i$ where κ is an arbitrary variable), then $\widetilde{\phi}$ will be the conditionally averaged version of ϕ because it has only been averaged over regions where fluid i exists. As an example, the volume fraction of a fluid is given by $\sigma_i = \widetilde{I_i}$ and the fluid density by $\rho_i = \widetilde{I_i \rho}/\sigma_i$.

The conditional filter can also be applied to the governing equations themselves to obtain prognostic equations for each of the fluids. The full derivation of the multi-fluid compressible Euler equations is given in Thuburn et al. (2018). Using notation from Weller and McIntyre (2019), we define our prognostic variables as the fluid mass per

unit volume ($\sigma_i \rho_i$), the fluid potential temperature (θ_i) and the fluid velocity ($\boldsymbol{u}_i$). For convenience, we also define $\eta_i \equiv \sigma_i \rho_i$ so that we have a single variable to represent the fluid i mass. Using this notation, the multi-fluid compressible Euler equations in flux form are given by the continuity equation,

$$\frac{\partial \eta_i}{\partial t} + \boldsymbol{\nabla}.(\eta_i \boldsymbol{u}_i) = \underbrace{\sum_{j \neq i} (\eta_j S_{ji} - \eta_i S_{ij})}_{\text{Mass transfers}}, \tag{1.44}$$

the potential temperature equation,

$$\frac{\partial (\eta_i \theta_i)}{\partial t} + \boldsymbol{\nabla}.(\eta_i \theta_i \boldsymbol{u}_i) = \underbrace{\sum_{j \neq i} (\eta_j \theta_j S_{ji} - \eta_i \theta_i S_{ij})}_{\text{Transfer mean temp.}} - \underbrace{\eta_i \sum_{j \neq i} H_{ij}}_{\text{Heat transfer}}, \tag{1.45}$$

and momentum equation for each fluid,

$$\frac{\partial (\eta_i \boldsymbol{u}_i)}{\partial t} + \boldsymbol{\nabla}.(\eta_i \boldsymbol{u}_i \boldsymbol{u}_i) = \eta_i \boldsymbol{g} - \underbrace{2\eta_i \boldsymbol{\Omega} \times \boldsymbol{u}_i}_{\text{Coriolis}} - \underbrace{c_p \eta_i \theta_i \boldsymbol{\nabla} \pi}_{\text{Pressure}} + \underbrace{\sum_{j \neq i} (\eta_j \boldsymbol{u}_j S_{ji} - \eta_i \boldsymbol{u}_i S_{ij})}_{\text{Transfer mean velocity.}} - \underbrace{\eta_i \sum_{j \neq i} \boldsymbol{D}_{ij}}_{\text{Drag}}, \tag{1.46}$$

where S_{ij} is the unidirectional mass transfer rate from fluid i to fluid j ($S_{ij} \geq 0$) and the mean temperatures and velocities are assumed to be transferred between fluids. c_p is the heat capacity of dry air at constant pressure, $\boldsymbol{\Omega}$ is the rotation rate of the domain and $\boldsymbol{g}$ is the gravitational acceleration. $\pi \equiv p^\kappa / p_0^\kappa$ is the Exner pressure where p is the pressure, p_0 is the reference pressure at the surface, $\kappa = R/c_p$ and R is the gas constant of dry air. H_{ij} is the heat transfer between fluids i and j (which does not exchange mass between fluids) and $\boldsymbol{D}_{ij}$ is the drag between fluids i and j. Additionally, the equation of state for dry air is used to relate the pressure and fluid temperatures:

$$p_0 \pi^{\frac{1-\kappa}{\kappa}} = R \sum_i \eta_i \theta_i. \tag{1.47}$$

Note that the pressure in each fluid is the same but Thuburn et al. (2018) suggested that the drag term could be used to parameterise pressure differences in the fluids.

A parameterisation of convection using the multi-fluid equations relies entirely on formulating transfer terms that exchange mass and other properties between fluids. The form of these transfer terms depend on the fluid definitions and the properties at the cloud/fluid interfaces (De Rooy et al., 2013). As we have chosen to define our fluids by the sign of the vertical velocity (equations 1.41 and 1.42), the transfer terms must specifically represent the regions of air which have had a change in sign of vertical

velocity. The form of the transfer terms would ideally be derived by conditionally filtering the governing equations but this will not be done in this study as the resulting terms include delta functions which cannot trivially be filtered (Weller et al., 2020).

The transfer terms are equivalent to entrainment, detrainment and the triggering of convection (cloud-base mass flux) which may be adapted from existing schemes (such as Gregory and Rowntree, 1990; Neggers et al., 2002; Siebesma et al., 2007; Pergaud et al., 2009; Stirling and Stratton, 2012) if the fluid definitions are similar to the plume definitions in the existing schemes. Sketches of the turbulent and dynamical mixing processes are labelled as S_{ij} in figure 1.3.

Regardless of how physical processes are modelled, solving the multi-fluid equations also requires a new numerical scheme which is stable with respect to gravity and acoustic waves in all fluids and for strong updrafts. We must also address how the multi-fluid method can combat the issues identified in section 1.3.9.

1.4.1 Net mass transport by convection

Many convection parameterisations are single-column models designed for horizontal resolutions far larger than the horizontal length scales of convective plumes (for example Arakawa and Schubert, 1974; Gregory and Rowntree, 1990; Kain and Fritsch, 1990). As such, it is often assumed that the circulations induced by convective clouds are contained within a single column. However, modern resolutions are much closer to the convective scales meaning convection may be the dominating driver of the vertical motion. In these cases, it is unreasonable to assume that the compensating subsidence only occurs in the same column as the updraft. This is an issue because it is important to accurately model the vertical transport of mass (and its properties) by convection for accurate models of the atmosphere (Arakawa, 2004; Grell et al., 2014).

There have been some attempts to incorporate the effects of mass transport by convection, including: Grell et al. (2014), who demonstrated a parameterisation which spreads subsidence over neighboring columns, Malardel and Bechtold (2019), who implemented an adjustment to the updraft/downdraft properties for the integrated forecasting system (IFS) at ECMWF, and Kuell and Bott (2008), who implemented net mass transport by convection to the COSMO model (Consortium for Small Scale Modelling).

The multi-fluid approach does not restrict the updraft/downdraft of a single

convective plume to a single column, unlike traditional bulk, adjustment and stochastic schemes. Instead, the fluid properties (including the convective fluid) are grid-scale variables which are computed directly by the dynamical core (instead of being diagnosed each timestep by a modular parameterisation). A convective fluid in one cell can therefore interact with neighbouring cells horizontally and vertically (as indicated in figure 1.3). This means that pressure anomalies (such as those produced by the vertical convergence of mass in a convective plumes) can push or pull mass to neighbouring columns - hence, net mass transport by convection is a property of the multi-fluid method.

1.4.2 Convective memory

Holloway et al. (2014) state that convective memory is important for accurate modern-day parameterisations. However, many parameterisations initiate convection when a specific condition is fulfilled (which is usually related to the level of CAPE or instability present in a parcel). An unintended consequence of such closures is that intermittent behaviour of the convection scheme can occur when close to the initiation condition - a scheme which is convecting at some timestep may no longer fulfil the same discrete condition at the next timestep. This becomes an issue when the timescales of convection are comparable (or larger than) the timestep of the model where there should be some correlation between convective activity at one timestep and the next. An example of this issue is given by Willett and Whitall (2017), who note that the UK Met Office's GA7 scheme produces intermittent entrainment rates (as well as intermittent precipitation).

A scheme has convective memory when the properties of a convective plume (such as updraft temperature and vertical velocity) evolve from the values at the previous timestep. This allows for smooth transitions of convective activity and thus removes any intermittency. The multi-fluid method computes the convection in the dynamical core meaning the convective fluid properties are stored as prognostic variables. As such, a multi-fluid convection scheme has convective memory by default.

1.4.3 Scale-awareness and the triggering of convection

A convection scheme should ideally work at any resolution (Holloway et al., 2014), but many parameterisations are tuned to perform well for a specific grid spacing and a specific model. This is often an issue for convection schemes which are single-column models, or have discrete triggering functions which don't automatically adapt for grey zone resolutions. Lancz et al. (2018) note that the forcing from a convection parameter-

isation must be regulated in the grey zone, but the threshold resolution for turning off a parameterisation is still not well established (Yano et al., 2018). At high resolutions, the model should also converge to the observed solution but convergence has long been an issue for convection parameterisations (Arakawa, 2004). Several attempts to make scale-aware schemes have been made, such as Arakawa et al. (2011) and Kwon and Hong (2017) who attempt to transition between the parameterised sub-grid activity and the resolved flow, depending on the resolution.

The multi-fluid scheme has the potential to be scale aware as the equations of motion for the resolved flow are the same for the convective updrafts (making the scheme consistent) - increasing column width will decrease the updraft volume fraction but the same rising motion should take place. Moreover, when convection is fully resolved, the multi-fluid equations essentially converge to the single-fluid compressible Euler equations as the fluid volume fractions will approach 0 or 1 in every cell.

1.4.4 Computation time

For an N-fluid system, the computational cost will be less than N-times greater the cost of a single-fluid dynamical core without a convection scheme (if there is only one pressure equation). However, a multi-fluid scheme may have more restrictive timestep contraints relative to a single-fluid dynamical core due to the fast updraft velocities within convective plumes. Implicit advection schemes or sub-stepping (multiple smaller timesteps for each model timestep) could be used to address this issue, but both of these options are computationally expensive.

If the multi-fluid method is significantly more expensive than other parameterisations, then conventional convection schemes may be able to run at higher horizontal resolutions for the same computational cost. However, as most parameterisations fail to accurately model convection in the grey zone, a small increase in resolution may be insignificant relative to the potential benefits of a multi-fluid model.

1.5 Summary, motivation and thesis outline

A common issue with convection parameterisations is their inability to accurately represent shallow and deep convection in the grey zone, as they assume a horizontal grid spacing far larger than the horizontal length scales of convection. A common assumption involves ignoring the net mass transfer by convection which causes issues

when convection is the dominant driver of the vertical motion. Most convection schemes are also not scale aware and do not incorporate convective memory. As such, these convection schemes lack consistency and do not converge at higher resolutions. Some promising new techniques are being developed such as super parameterisation, stochastic schemes and machine-learning which can help reduce the errors in convection parameterisations, but incorporating net mass transport by convection into these schemes is not trvial.

The multi-fluid equations have been proposed for modelling convection accurately and consistently across all resolutions because:

- **A multi-fluid scheme is not a single-column model**, meaning that convective circulations can span multiple columns. This is important at grey zone resolutions where convective elements have similar horizontal scales relative to the grid scale. At coarse resolutions (where the scheme converges to a single-column model), a multi-fluid scheme can prevent grid-scale instabilities (such as grid-point storms) by allowing fluids to move in opposite directions at scales smaller than the grid scale.
- **A multi-fluid scheme treats the updraft area fraction, updraft velocity and other updraft properties as prognostic variables** (meaning the scheme has convective memory), instead of being diagnosed at each timestep like in most traditional parameterisations (using equilibrium assumptions). This is important when the turnover time for convective circulations is comparable-to or larger than the timestep of the model.
- **A multi-fluid scheme uses the dynamical core to simulate convection at any resolution.** This means that the convection scheme should converge at high resolution.

The multi-fluid equations are a challenging departure from existing parameterisations because:

- A new, multi-fluid dynamical core and numerical scheme is required. This means that the convection scheme is not modular, and can not be easily replaced with other convection schemes.
- The interaction of the fluids must be understood. This includes the differences in fluid properties as well as entrainment/detrainment terms which depends on the definition of the fluids.
- The scheme must perform better than existing parameterisations in the grey zone.

In this thesis, we aim to further the general understanding of the multi-fluid equations and demonstrate what is needed to produce a scale-aware multi-fluid dry convec-

tion scheme. By predominantly focussing on a two-fluid system (defined by the sign of vertical velocity), we will attempt to address the following issues:

1. Multi-fluid systems are known to be ill-posed when the fluids share the same pressure (Stewart and Wendroff, 1984; Thuburn et al., 2019), but it is not known how a two-fluid system for convection should be stabilised. Terms which stabilise the equation set should be analysed and tested.

2. Accurate and stable numerical methods must be developed for the multi-fluid equations, including for the fluid transfer terms which represent entrainment and detrainment between the convective plumes and the surrounding environment.

3. The functional form of the entrainment and detrainment must be diagnosed so that the fluid transfer terms are representative of the physical processes in the atmosphere. In order to be consistent with the fluid definitions, the transfer terms in our two-fluid model should model when the sign of the vertical velocity changes.

In chapter 2, the stability of a two-fluid system with different pressures and transfer terms between fluids is analysed, in an attempt to find terms which stabilise the system (issue 1). Numerical analysis of the transfer terms (which exchange mass between the fluids) is conducted in chapter 3 (issue 2). Finally, in chapter 4 we use a resolved dry convection test case to diagnose fluid transfer and pressure terms (issue 3), and conduct coarse 2-fluid simulations at various resolutions, including the grey zone.

Chapter 2

Stability analysis of an incompressible two-fluid system

Multi-fluid and multi-phase models have been used for many decades to simulate a variety of systems including nuclear thermal hydraulics (e.g. Méchitoua et al., 2003; Guelfi et al., 2007), combustion and explosion models (e.g. Baer and Nunziato, 1986; Embid et al., 1992), compressible flows (e.g. Saurel and Abgrall, 1999), and more recently, convective systems (e.g. Thuburn et al., 2018; Tan et al., 2018; Weller and McIntyre, 2019). In chapter 1, the multi-fluid compressible Euler equations were presented, which use a shared pressure gradient term (which is also assumed in Thuburn et al., 2018; Tan et al., 2018; Weller and McIntyre, 2019).

Stewart and Wendroff (1984) showed that multi-fluid equations with a shared pressure are ill-posed in the sense that positive imaginary components of the phase velocity exist which facilitate the exponential growth of certain modes. This behaviour occurs when sub-filter-scale terms in the multi-fluid equations are neglected, or if poor assumptions are made to represent them. Ideally, a multi-fluid convection scheme should model all sub-filter scale variability mass exchanges to a high degree of accuracy but further research is necessary to derive and test these terms.

Thuburn et al. (2019) analysed an incompressible, one-dimensional, two-fluid system (with a shared pressure) for convection. They verified that an instability exists in the form of a Kelvin-Helmholtz instability, which describes the growth of perturbations in a system with shear - such an instability is expected in a convective system because updrafts and downdrafts travel in opposite directions, and velocity components perpendicular to the fluid interface will necessarily cause changes to the updraft volume fraction (which may be classified as entrainment or detrainment). Thuburn et al. (2019) showed that the smallest-scale modes (largest wavenumbers) grew the fastest, but they did not derive any terms that could stabilise the system. Although the Kelvin-Helmholtz instability is representative of real instabilities in the atmosphere, the lack of a complete and accurate model for the sub-filter-scale physics (which would prevent the instabilities from growing indefinitely) means that the unstable two-fluid

model is not useful for modelling convection. It is therefore necessary to find terms which stabilise the two-fluid system and provide smooth solutions for any initial conditions. The suppression of the instability would then allow the model to represent an average of the true solution, and would allow for a baseline two-fluid scheme where additional complexity (such as more sub-filter-scale processes) can be added in future studies.

In this chapter, we extend the analysis of the two-fluid incompressible equations from Thuburn et al. (2019) to include differences in pressure and mass exchanges between fluids. From this analysis, we will be able to decipher whether adding these additional coupling terms can stabilise a two-fluid system.

2.1 The 2-fluid system analysis of Thuburn et al. (2019)

Thuburn et al. (2019) analysed the stability of a one-dimensional, two-fluid, incompressible system with a shared pressure gradient:

$$\sigma_0 + \sigma_1 = 1 \tag{2.1}$$

$$\frac{\partial \sigma_0}{\partial t} + \frac{\partial (\sigma_0 w_0)}{\partial z} = 0 \tag{2.2}$$

$$\frac{\partial \sigma_1}{\partial t} + \frac{\partial (\sigma_1 w_1)}{\partial z} = 0 \tag{2.3}$$

$$\frac{\partial w_0}{\partial t} + w_0 \frac{\partial w_0}{\partial z} + \frac{\partial p}{\partial z} = 0 \tag{2.4}$$

$$\frac{\partial w_1}{\partial t} + w_1 \frac{\partial w_1}{\partial z} + \frac{\partial p}{\partial z} = 0, \tag{2.5}$$

where σ_i and w_i are the volume fraction and vertical velocity of fluid i respectively ($i \in \{0, 1\}$), and p is the pressure. By linearising the governing equations and assuming wave-like solutions proportional to $e^{i(mz - \Omega t)}$ (where m is the wavenumber and Ω is the angular frequency), Thuburn et al. (2019) derived the following relation for the frequency:

$$\Omega = (\overline{\sigma}_0 \overline{w}_1 + \overline{\sigma}_1 \overline{w}_0) m \pm im \sqrt{\overline{\sigma}_0 \overline{\sigma}_1} (\overline{w}_0 - \overline{w}_1), \tag{2.6}$$

where the overbars denote the mean variable states which don't change in time or space. Ω has an imaginary component, meaning that the solution takes the form $e^{Rt} e^{im(z - w_A t)}$, where $w_A \equiv \overline{\sigma}_0 \overline{w}_1 + \overline{\sigma}_1 \overline{w}_0$ and R is the growth rate which is equal to $\pm m \sqrt{\overline{\sigma}_0 \overline{\sigma}_1} (\overline{w}_0 - \overline{w}_1)$. A positive value of R (which occurs for $\mathrm{Im}(\Omega) > 0$) ensures that the amplitude of the wavemodes will increase exponentially with time. The growth rate is also proportional to the wavenumber in this case meaning the smallest scale modes

grow the fastest. Thuburn et al. (2019) noted that the growth takes the same form as a Kelvin-Helmholtz instability, similar to equation 1.31 from chapter 1 when $g = 0$ m s^{-2}. The instability disappears only when there is no shear (when $\overline{w}_0 = \overline{w}_1$) or when either volume fraction is zero. Similar instabilities in multi-fluid systems with a shared pressure have been previously noted (e.g. Stewart and Wendroff, 1984). Mass exchanges and different pressures for each fluid should therefore be considered in order to stabilise this 2-fluid system.

2.2 Extending the Thuburn et al. (2019) analysis

By adding mass transfer terms to equations 2.2-2.5 as well as a pressure anomaly (p_i) to each fluid, the prognostic equations become:

$$\sigma_0 + \sigma_1 = 1 \tag{2.7}$$

$$\frac{\partial \sigma_0}{\partial t} + \frac{\partial (\sigma_0 w_0)}{\partial z} = \sigma_1 S_{10} - \sigma_0 S_{01} \tag{2.8}$$

$$\frac{\partial \sigma_1}{\partial t} + \frac{\partial (\sigma_1 w_1)}{\partial z} = \sigma_0 S_{01} - \sigma_1 S_{10} \tag{2.9}$$

$$\frac{\partial w_0}{\partial t} + w_0 \frac{\partial w_0}{\partial z} + \frac{\partial p}{\partial z} + \frac{\partial p_0}{\partial z} = \frac{\sigma_1}{\sigma_0} S_{10}(w_{10}^T - w_0) - S_{01}(w_{01}^T - w_0) \tag{2.10}$$

$$\frac{\partial w_1}{\partial t} + w_1 \frac{\partial w_1}{\partial z} + \frac{\partial p}{\partial z} + \frac{\partial p_1}{\partial z} = \frac{\sigma_0}{\sigma_1} S_{01}(w_{01}^T - w_1) - S_{10}(w_{10}^T - w_1), \tag{2.11}$$

where S_{ij} is the transfer rate from fluid i to fluid j and w_{ij}^T is the vertical velocity of the fluid transferred from i to j. The total pressure of a fluid is given by $p + p_i$.

The linearised equation sets will be analysed with the following assumptions:

1. The pressure anomaly for each fluid is chosen to be

$$p_i = -\gamma \frac{\partial w_i}{\partial z}, \tag{2.12}$$

   which describes the increase of pressure in a fluid when it converges. The chosen pressure term is similar to the pressure anomaly used by Weller et al. (2020), and acts as a diffusion of vertical velocity in one dimension similar to Thuburn et al. (2019). In both studies, stable simulations were conducted using these terms. As noted be Weller et al. (2020), this pressure term does not conserve energy, but any energy sinks can be used as a turbulent kinetic energy source in future multi-fluid models.

2. Each variable is equal to the sum of a mean state (uniform in space and time, de-

noted by an overbar) and a perturbation (denoted by a dash). Our variables therefore become:

$$\sigma_0 = \overline{\sigma}_0 + \sigma_0' \tag{2.13}$$
$$\sigma_1 = \overline{\sigma}_1 + \sigma_1' \tag{2.14}$$
$$w_0 = \overline{w}_0 + w_0' \tag{2.15}$$
$$w_1 = \overline{w}_1 + w_1' \tag{2.16}$$
$$p = \overline{p} + p'. \tag{2.17}$$

3. Second-order perturbation terms are assumed to be small and are neglected.

4. The perturbation terms are wave-like and are therefore proportional to $e^{i(mz-\Omega t)}$, where $i = \sqrt{-1}$, m is the wavenumber and Ω is the angular frequency.

5. The transfer rates are proportional to vertical velocity divergence:

$$S_{01} = \alpha \frac{\partial w_0}{\partial z} \tag{2.18}$$
$$S_{10} = \alpha \frac{\partial w_1}{\partial z}, \tag{2.19}$$

   where α is a constant. This transfer describes mixing which occurs when a fluid parcel accelerates or decelerates, and is similar to the dynamical entrainment described in Houghton and Cramer (1951) and De Rooy et al. (2013). A similar transfer term was also used in Weller et al. (2020), and was shown to produce accurate volume fractions in 2-fluid simulations.

6. The interface vertical velocity is assumed to be zero, meaning $w_{01}^T = w_{10}^T = 0$. This assumption is also made by Weller et al. (2020), as one fluid is defined as rising air and the other as descending air. The velocity at the fluid interface is therefore $w = 0\ \mathrm{ms}^{-1}$.

7. The following definitions will be used for convenience:

$$\overline{w} = \overline{\sigma}_0\overline{w}_0 + \overline{\sigma}_1\overline{w}_1 \tag{2.20}$$
$$w_A = \overline{\sigma}_1\overline{w}_0 + \overline{\sigma}_0\overline{w}_1 \tag{2.21}$$
$$w_B^2 = \overline{\sigma}_1\overline{w}_0^2 + \overline{\sigma}_0\overline{w}_1^2 \tag{2.22}$$
$$w_\Delta = \overline{w}_1 - \overline{w}_0 \tag{2.23}$$
$$w_\sigma = (\overline{\sigma}_1 - \overline{\sigma}_0)(\overline{w}_1 - \overline{w}_0). \tag{2.24}$$

Substituting terms from assumptions 1, 2, 5 and 6 into the prognostic equations (2.7-

2.11) and eliminating second-order perturbation terms gives the linearised equations:

$$\overline{\sigma}_0 + \overline{\sigma}_1 = 1 \tag{2.25}$$

$$\sigma_0' + \sigma_1' = 0 \tag{2.26}$$

$$\frac{\partial \sigma_0'}{\partial t} + \overline{\sigma}_0 \frac{\partial w_0'}{\partial z} + \overline{w}_0 \frac{\partial \sigma_0'}{\partial z} = \alpha \overline{\sigma}_1 \frac{\partial w_1'}{\partial z} - \alpha \overline{\sigma}_0 \frac{\partial w_0'}{\partial z} \tag{2.27}$$

$$\frac{\partial \sigma_1'}{\partial t} + \overline{\sigma}_0 \frac{\partial w_1'}{\partial z} + \overline{w}_1 \frac{\partial \sigma_1'}{\partial z} = \alpha \overline{\sigma}_0 \frac{\partial w_0'}{\partial z} - \alpha \overline{\sigma}_1 \frac{\partial w_1'}{\partial z} \tag{2.28}$$

$$\frac{\partial w_0'}{\partial t} + \overline{w}_0 \frac{\partial w_0'}{\partial z} + \frac{\partial p'}{\partial z} - \gamma \frac{\partial^2 w_0'}{\partial z^2} = -\alpha \frac{\overline{\sigma}_1}{\overline{\sigma}_0} \overline{w}_0 \frac{\partial w_1'}{\partial z} + \alpha \overline{w}_0 \frac{\partial w_0'}{\partial z} \tag{2.29}$$

$$\frac{\partial w_1'}{\partial t} + \overline{w}_1 \frac{\partial w_1'}{\partial z} + \frac{\partial p'}{\partial z} - \gamma \frac{\partial^2 w_1'}{\partial z^2} = -\alpha \frac{\overline{\sigma}_0}{\overline{\sigma}_1} \overline{w}_1 \frac{\partial w_0'}{\partial z} + \alpha \overline{w}_1 \frac{\partial w_1'}{\partial z}. \tag{2.30}$$

By further substituting the wave-like solutions proportional to $e^{i(mz-\Omega t)}$, equations 2.27-2.30 become:

$$-w_p \sigma_0' + \overline{w}_0 \sigma_0' + \overline{\sigma}_0 w_0' = \alpha \overline{\sigma}_1 w_1' - \alpha \overline{\sigma}_0 w_0' \tag{2.31}$$

$$-w_p \sigma_1' + \overline{w}_1 \sigma_1' + \overline{\sigma}_1 w_1' = \alpha \overline{\sigma}_0 w_0' - \alpha \overline{\sigma}_1 w_1' \tag{2.32}$$

$$-w_p w_0' + \overline{w}_0 w_0' + p' - im\gamma w_0' = -\alpha \frac{\overline{\sigma}_1}{\overline{\sigma}_0} \overline{w}_0 w_1' + \alpha \overline{w}_0 w_0' \tag{2.33}$$

$$-w_p w_1' + \overline{w}_1 w_1' + p' - im\gamma w_1' = -\alpha \frac{\overline{\sigma}_0}{\overline{\sigma}_1} \overline{w}_1 w_0' + \alpha \overline{w}_1 w_1', \tag{2.34}$$

where $w_p = \Omega/m$ is the phase velocity. Equations 2.31 and 2.32 can be rearranged such that

$$\sigma_0' = \frac{(1+\alpha)\overline{\sigma}_0 w_0' - \alpha \overline{\sigma}_1 w_1'}{w_p - \overline{w}_0} \tag{2.35}$$

$$\sigma_1' = \frac{(1+\alpha)\overline{\sigma}_1 w_1' - \alpha \overline{\sigma}_0 w_0'}{w_p - \overline{w}_1}, \tag{2.36}$$

and using $\sigma_0' = -\sigma_1'$, the volume fraction perturbation terms can be removed:

$$\frac{(1+\alpha)\overline{\sigma}_0 w_0' - \alpha \overline{\sigma}_1 w_1'}{w_p - \overline{w}_0} = -\frac{(1+\alpha)\overline{\sigma}_1 w_1' - \alpha \overline{\sigma}_0 w_0'}{w_p - \overline{w}_1} \tag{2.37}$$

$$\left[(1+\alpha)\overline{\sigma}_0 (w_p - \overline{w}_1) - \alpha \overline{\sigma}_0 (w_p - \overline{w}_0)\right] w_0' = -\left[(1+\alpha)\overline{\sigma}_1 (w_p - \overline{w}_0) - \alpha \overline{\sigma}_1 (w_p - \overline{w}_1)\right] w_1' \tag{2.38}$$

$$\implies w_0' = -\frac{(1+\alpha)\overline{\sigma}_1 (w_p - \overline{w}_0) - \alpha \overline{\sigma}_1 (w_p - \overline{w}_1)}{(1+\alpha)\overline{\sigma}_0 (w_p - \overline{w}_1) - \alpha \overline{\sigma}_0 (w_p - \overline{w}_0)} w_1' \tag{2.39}$$

$$= -\frac{\overline{\sigma}_1 (w_p - \overline{w}_0) + \alpha \overline{\sigma}_1 w_\Delta}{\overline{\sigma}_0 (w_p - \overline{w}_1) - \alpha \overline{\sigma}_0 w_\Delta} w_1', \tag{2.40}$$

where $w_\Delta = \overline{w}_1 - \overline{w}_0$.

Equations 2.33 and 2.34 can be combined to remove p',

$$(w_p - \overline{w}_0 + im\gamma)w_0' - \alpha\frac{\overline{\sigma}_1}{\overline{\sigma}_0}\overline{w}_0 w_1' + \alpha\overline{w}_0 w_0' = (w_p - \overline{w}_1 + im\gamma)w_1' - \alpha\frac{\overline{\sigma}_0}{\overline{\sigma}_1}\overline{w}_1 w_0' + \alpha\overline{w}_1 w_1', \tag{2.41}$$

and by defining $w_A = \overline{\sigma}_1\overline{w}_0 + \overline{\sigma}_0\overline{w}_1$ for convenience, the terms can be re-arranged for w_0

$$\left[(w_p - \overline{w}_0) + \frac{\alpha}{\overline{\sigma}_1}w_A + im\gamma\right] w_0' = \left[(w_p - \overline{w}_1) + \frac{\alpha}{\overline{\sigma}_0}w_A + im\gamma\right] w_1' \tag{2.42}$$

$$\implies w_0' = \frac{(w_p - \overline{w}_1) + \frac{\alpha}{\overline{\sigma}_0}w_A + im\gamma}{(w_p - \overline{w}_0) + \frac{\alpha}{\overline{\sigma}_1}w_A + im\gamma}w_1'. \tag{2.43}$$

Equating 2.40 and 2.43 removes w_0' and w_1':

$$\frac{(w_p - \overline{w}_1) + \frac{\alpha}{\overline{\sigma}_0}w_A + im\gamma}{(w_p - \overline{w}_0) + \frac{\alpha}{\overline{\sigma}_1}w_A + im\gamma} = -\frac{\overline{\sigma}_1(w_p - \overline{w}_0) + \alpha\overline{\sigma}_1 w_\Delta}{\overline{\sigma}_0(w_p - \overline{w}_1) - \alpha\overline{\sigma}_0 w_\Delta} \tag{2.44}$$

$$\implies w_p^2 - 2\left[w_A - \alpha\left(w_A + \frac{1}{2}w_\sigma\right) - \frac{1}{2}im\gamma\right] w_p \tag{2.45}$$

$$+ \left[w_B^2 - \alpha(\overline{w}_0 + \overline{w}_1)w_A + \alpha(\overline{\sigma}_0\overline{w}_1 - \overline{\sigma}_1\overline{w}_0)w_\Delta + im\gamma(\alpha w_\sigma - w_A)\right] = 0 \tag{2.46}$$

$$\implies w_p^2 - 2\left[w_A - \frac{\alpha}{2}(\overline{w}_0 + \overline{w}_1) - \frac{1}{2}im\gamma\right] w_p \tag{2.47}$$

$$+ \left[w_B^2 - 2\alpha\overline{w}_0\overline{w}_1 + im\gamma(\alpha w_\sigma - w_A)\right] = 0, \tag{2.48}$$

where $w_A = \overline{\sigma}_0\overline{w}_1 + \overline{\sigma}_1\overline{w}_0$, $w_B^2 = \overline{\sigma}_0\overline{w}_1^2 + \overline{\sigma}_1\overline{w}_0^2$ and $w_\sigma = (\overline{\sigma}_1 - \overline{\sigma}_0)(\overline{w}_1 - \overline{w}_0)$.

With the help of equation 2.25, the solution for the quadratic equation for w_p is:

$$w_p = w_A - \frac{\alpha}{2}(\overline{w}_0 + \overline{w}_1) - \frac{1}{2}im\gamma \pm \sqrt{\left[w_A - \frac{\alpha}{2}(\overline{w}_0 + \overline{w}_1) - \frac{1}{2}im\gamma\right]^2 - w_B^2 + 2\alpha\overline{w}_0\overline{w}_1 - im\gamma(\alpha w_\sigma - w_A)} \tag{2.49}$$

Using

$$\begin{aligned} w_A^2 - w_B^2 &= (\overline{\sigma}_0\overline{w}_1 + \overline{\sigma}_1\overline{w}_0)^2 - (\overline{\sigma}_0\overline{w}_1^2 + \overline{\sigma}_1\overline{w}_0^2) \\ &= (\overline{\sigma}_0^2\overline{w}_1^2 + 2\overline{\sigma}_0\overline{\sigma}_1\overline{w}_0\overline{w}_1 + \overline{\sigma}_1^2\overline{w}_1^2) - (\overline{\sigma}_0 + \overline{\sigma}_1)(\overline{\sigma}_0\overline{w}_1^2 + \overline{\sigma}_1\overline{w}_0^2) \\ &= -\overline{\sigma}_0\overline{\sigma}_1(\overline{w}_1 - \overline{w}_0)^2, \end{aligned} \tag{2.50}$$

the phase velocity reduces to:

$$w_p = (\overline{\sigma}_0\overline{w}_1 + \overline{\sigma}_1\overline{w}_0) - \frac{\alpha}{2}(\overline{w}_0 + \overline{w}_1) - \frac{1}{2}im\gamma$$
$$\pm \left\{ -\overline{\sigma}_0\overline{\sigma}_1(\overline{w}_1 - \overline{w}_0)^2 + \frac{1}{4}\alpha^2(\overline{w}_0 + \overline{w}_1)^2 - \frac{1}{4}m^2\gamma^2 \right.$$
$$\left. -\alpha(\overline{w}_1 - \overline{w}_0)(\overline{\sigma}_0\overline{w}_1 - \overline{\sigma}_1\overline{w}_0) + im\alpha\gamma\left[\left(\frac{1}{2} + \overline{\sigma}_1 - \overline{\sigma}_0\right)\overline{w}_0 + \left(\frac{1}{2} + \overline{\sigma}_0 - \overline{\sigma}_1\right)\overline{w}_1\right]\right\}^{\frac{1}{2}}. \tag{2.51}$$

2.2.1 Sanity checks

- In the single-fluid case (where $\overline{\sigma}_0 = 1$ or $\overline{\sigma}_1 = 1$ or $\overline{w}_0 = \overline{w}_1$) and in the absence of pressure differences, the phase velocity reduces to $w_p = \overline{w}$.
- In the single-fluid case with pressure differences, the phase velocity reduces to $w_p = \overline{w} - im\gamma$ which is the solution for an advection-diffusion equation. The wavemodes are proportional to $e^{-m^2\gamma t}e^{im(z-\overline{w}t)}$ and therefore decay at a rate $m^2\gamma$ where the small-scale modes (large m) are damped the most.
- In the 2-fluid case with no pressure differences or transfer terms, the phase velocity reduces to that in Thuburn et al. 2019: $w_p = (\overline{\sigma}_0\overline{w}_1 + \overline{\sigma}_1\overline{w}_0) \pm i\sqrt{\overline{\sigma}_0\overline{\sigma}_1}(\overline{w}_0 - \overline{w}_1)$. This phase velocity has a positive imaginary component which facilitates exponential growth, meaning the system is unstable (a Kelvin-Helmholtz instability in this case). w_p (and therefore Ω) is only real if one of the volume fractions is zero (1-fluid system) or if the mean fluid velocities are equal (same fluid properties $\rightarrow$ 1-fluid system). The instabilities grow fastest with the smallest scale modes (large wavenumbers, m).

2.2.2 Using pressure perturbations without mass transfers

In the case where pressure differences between fluids exist ($\gamma > 0$) but no mass exchanges between fluids take place ($\alpha = 0$, $S_{01} = S_{10} = 0$), the frequency, $\Omega = mw_p$ is given by

$$\Omega = (\overline{\sigma}_0\overline{w}_1 + \overline{\sigma}_1\overline{w}_0)m - im\left[\frac{1}{2}m\gamma \pm \sqrt{\overline{\sigma}_0\overline{\sigma}_1(\overline{w}_0 - \overline{w}_1)^2 + \frac{1}{4}m^2\gamma^2}\right]. \tag{2.52}$$

In order to ensure modes are decaying only, we require that $\mathrm{Im}(\Omega) \leq 0$, meaning

$$-\frac{1}{2}m\gamma + \sqrt{\overline{\sigma}_0\overline{\sigma}_1(\overline{w}_0 - \overline{w}_1)^2 + \frac{1}{4}m^2\gamma^2} \leq 0 \tag{2.53}$$

$$\sqrt{\overline{\sigma}_0\overline{\sigma}_1(\overline{w}_0 - \overline{w}_1)^2 + \frac{1}{4}m^2\gamma^2} \leq \frac{1}{2}m\gamma \tag{2.54}$$

$$\overline{\sigma}_0\overline{\sigma}_1(\overline{w}_0 - \overline{w}_1)^2 \leq 0, \tag{2.55}$$

which is not true unless the system is single-fluid. This result implies that using pressure differences proportional to convergence (or vertical velocity diffusion in the case of Thuburn et al., 2019) cannot completely stabilise the 2-fluid equations on its own, no matter the value of the coefficient (γ). However, it should be noted that using the pressure perturbation term significantly reduces the growth rate of the instability due to the negative imaginary component outside of the square-root in equation 2.52. This reduction of the growth rate is shown in figure 2.1 for a large range mean velocities and volume fractions.

2.2.3 Using mass transfers without pressure perturbations

When there are no pressure differences between the fluids but transfers between the fluids exist, the phase velocity reduces to:

$$\begin{aligned} w_p = {} & (\overline{\sigma}_0\overline{w}_1 + \overline{\sigma}_1\overline{w}_0) - \frac{\alpha}{2}(\overline{w}_0 + \overline{w}_1) \\ & \pm \sqrt{-\overline{\sigma}_0\overline{\sigma}_1(\overline{w}_1 - \overline{w}_0)^2 + \frac{1}{4}\alpha^2(\overline{w}_0 + \overline{w}_1)^2 - \alpha(\overline{w}_1 - \overline{w}_0)(\overline{\sigma}_0\overline{w}_1 - \overline{\sigma}_1\overline{w}_0)}. \end{aligned} \tag{2.56}$$

In order for there to be no imaginary component, the sum of the terms inside the square root must be positive:

$$-\overline{\sigma}_0\overline{\sigma}_1(\overline{w}_1 - \overline{w}_0)^2 + \frac{1}{4}\alpha^2(\overline{w}_0 + \overline{w}_1)^2 - \alpha(\overline{w}_1 - \overline{w}_0)(\overline{\sigma}_0\overline{w}_1 - \overline{\sigma}_1\overline{w}_0) \geq 0. \tag{2.57}$$

The $\frac{1}{4}\alpha^2(\overline{w}_0 + \overline{w}_1)^2$ term is positive and helps stabilise the system. Assuming the worst case scenario where this term is zero ($\overline{w}_1 = -\overline{w}_0$) and using $\max(\overline{\sigma}_0\overline{\sigma}_1) = \frac{1}{4}$, the condi-

tion becomes:

$$-4\overline{\sigma}_0\overline{\sigma}_1\overline{w}_1^2 - 2\alpha\overline{w}_1\left(\overline{\sigma}_0 + \overline{\sigma}_1\right) \geq 0 \tag{2.58}$$

$$\alpha \leq -2\overline{\sigma}_0\overline{\sigma}_1 \tag{2.59}$$

$$\alpha \leq -\frac{1}{2}. \tag{2.60}$$

The two-fluid system is therefore unconditionally stable if α has a large-enough negative value (i.e. if the mass transfers are large enough).

2.2.3.1 Comparing the transfer terms with Weller et al. (2020)

The mass transfer rate between fluids is given by

$$\begin{aligned}\left.\frac{\partial\sigma_0}{\partial t}\right|_{\text{transfers}} &= \sigma_1 S_{10} - \sigma_0 S_{01} \\ &= \alpha\sigma_1\frac{\partial w_1}{\partial z} - \alpha\sigma_0\frac{\partial w_0}{\partial z}.\end{aligned} \tag{2.61}$$

We know that $\boldsymbol{\nabla}.\boldsymbol{u} = 0$ because we have assumed an incompressible system. By also assuming uniform volume fractions with height, we get

$$\begin{aligned}\frac{\partial}{\partial z}\left(\sigma_0 w_0 + \sigma_1 w_1\right) &= 0 \\ \sigma_0\frac{\partial w_0}{\partial z} &= -\sigma_1\frac{\partial w_1}{\partial z},\end{aligned} \tag{2.62}$$

which means that

$$\left.\frac{\partial\sigma_0}{\partial t}\right|_{\text{transfers}} = 2\alpha\sigma_1\frac{\partial w_1}{\partial z} = -2\alpha\sigma_0\frac{\partial w_0}{\partial z} \tag{2.63}$$

$$\left.\frac{\partial\sigma_1}{\partial t}\right|_{\text{transfers}} = 2\alpha\sigma_0\frac{\partial w_0}{\partial z} = -2\alpha\sigma_1\frac{\partial w_1}{\partial z}. \tag{2.64}$$

If the transfer rates (S_{ij}) are strictly defined to be positive (as in Weller et al., 2020), then the transfer rates can be re-written as:

$$S_{01} = \max\left(0, 2\alpha\frac{\partial w_0}{\partial z}\right), \tag{2.65}$$

$$S_{10} = \max\left(0, 2\alpha\frac{\partial w_1}{\partial z}\right). \tag{2.66}$$

For stability $\left(\alpha = -\frac{1}{2}\right)$, the transfer terms must therefore be

$$S_{01} = \max\left(0, -\frac{\partial w_0}{\partial z}\right) \tag{2.67}$$

$$S_{10} = \max\left(0, -\frac{\partial w_1}{\partial z}\right), \tag{2.68}$$

which is the same form of the transfer terms used by Weller et al. (2020):

$$S_{01} = \max\left(0, -\boldsymbol{\nabla}.\boldsymbol{u}_0\right) \tag{2.69}$$

$$S_{10} = \max\left(0, -\boldsymbol{\nabla}.\boldsymbol{u}_1\right). \tag{2.70}$$

Weller et al. (2020) showed that stable (and accurate) 2-fluid convection can be simulated using these transfer terms, which is consistent with the result from equation 2.60.

2.2.4 Using pressure perturbations and mass transfers

In the case where we have pressure differences between fluids ($\gamma \neq 0$) and mass exchanges between fluids ($\alpha \neq 0$), the relation for the phase velocity (equation 2.51) has an imaginary component within the square root. The phase velocity and frequency can be evaluated numerically in order to find any positive imaginary components which make the modes unstable. Figure 2.1.d shows the imaginary components of equation 2.51 using $\gamma = 10^4$ m^2 s^{-1} and $\alpha = -\frac{1}{2}$, for a range of values for the volume fractions, wavemodes and velocities. All computed modes have zero or negative imaginary components to within machine precision, meaning they are stable. This is, perhaps, to be expected given that the transfer terms (without pressure differences) make the equations unconditionally stable, and using the pressure differences (without transfer terms) reduces the growth rate of the unstable modes.

2.3 Summary and conclusions

We have shown that the Kelvin-Helmholtz-like instability which exists in the incompressible 2-fluids equations with equal pressures (Stewart and Wendroff, 1984; Thuburn et al., 2019) can be suppressed by adding a suitable pressure perturbation term in each fluid which is proportional to the convergence of velocity. The term is similar to a viscosity in one dimension which damps the smallest scale modes the most. Similar terms were used by Thuburn et al. (2019) and Weller et al. (2020) to help stabilise their 2-fluid models.

Using mass transfer terms between fluids proportional to convergence makes the 2-fluid system from Thuburn et al. (2019) stable when the transfer coefficient fulfils $\alpha \leq -\frac{1}{2}$. This transfer term is similar to the dynamical entrainment used by Houghton and Cramer (1951) and De Rooy et al. (2013), and helps represent the averaged tendency of the fluids. The transfers also create smooth volume fraction fields by transferring regions where fluid is "bunching up". The system is also stable when these transfer terms are used in conjunction with the pressure perturbation terms. These results are consistent with Weller et al. (2020), who's 2-fluid Boussinesq model is stable and accurate when using the convergence-based mass exchanges.

It should be noted that these results do not guarantee stability in a compressible 2-fluid system with buoyancy, but similar pressure and transfer terms should be trialled for their effectiveness and accuracy (see chapter 4). Moreover, the 2-fluid system defined in this study represents the average tendencies of the fluids (as the fluids are defined by averaging over pre-defined volumes). Future studies should therefore focus on building upon the stable two-fluid scheme by accurately representing the sub-filter-scale physics in each fluid.

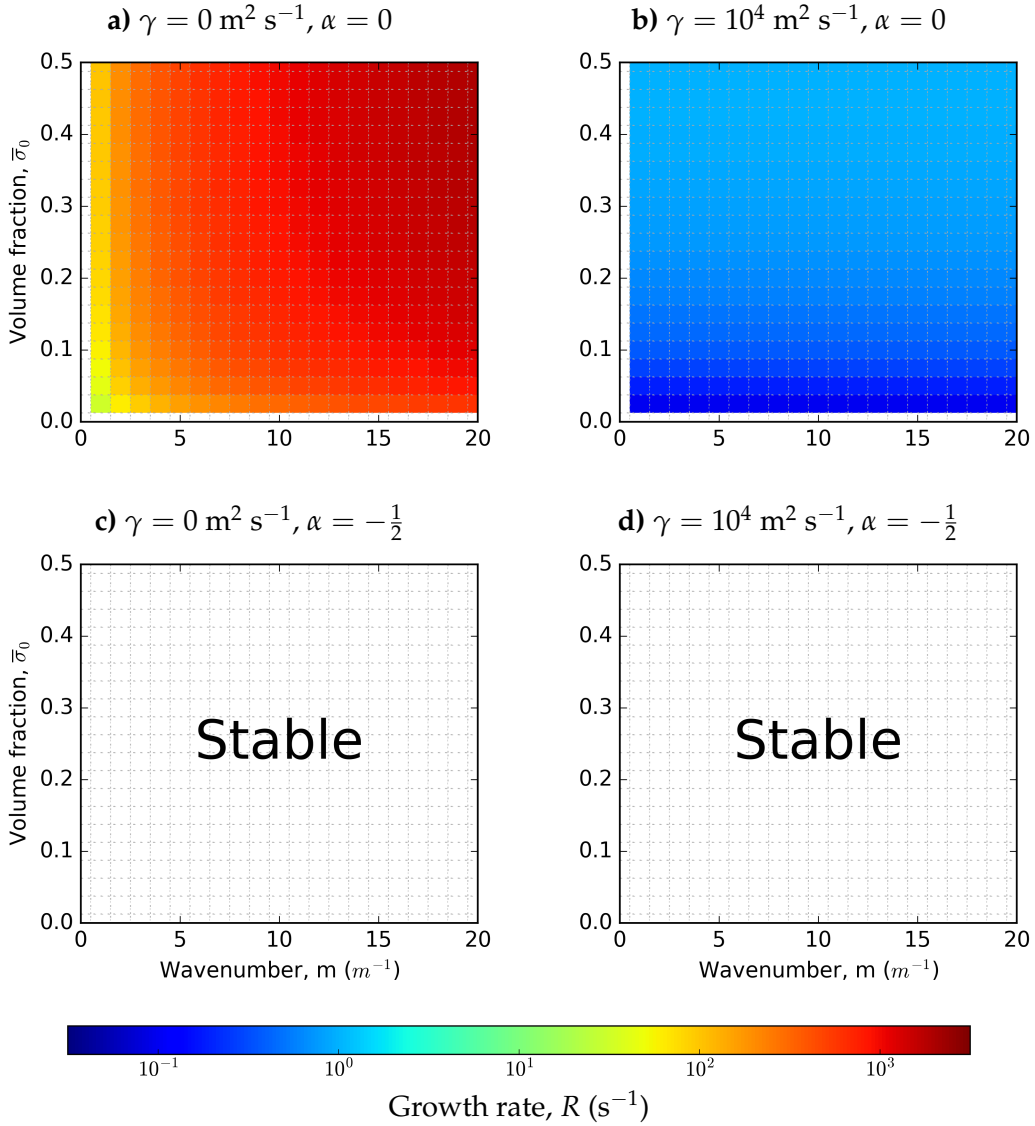

Figure 2.1: The maximum growth rate (equal to the imaginary component of the frequency Ω) for a range of values of the mean volume fraction and wavenumbers. Each data point is sampled over $\overline{w}_0$, $\overline{w}_1 \in [-100, 100]$ m s^{-1}, each incremented by 10 m s^{-1}. Results which are stable ($R \leq 0$) to within machine precision are shown in white. Panel a shows the unstable system analysed in Thuburn et al. (2019). Panel b shows how the pressure perturbation term significantly damps the unstable modes, by up to four orders of magnitude in the given parameter space. Panels c and d show the cases where mass transfers proportional to velocity convergence are used, which are both stable to within machine precision.

Chapter 3

Numerical methods for entrainment and detrainment in multi-fluid convection

The results from this chapter have been published in the Quarterly Journal of the Royal Meteorological Society (McIntyre et al., 2020).

Entrainment and detrainment are key in the interaction of convective clouds and their environment (De Rooy et al., 2013). Transfer terms that exchange mass and other properties between fluids are also crucial for formulating a parameterisation of convection in a multi-fluid model. These transfer terms are equivalent to entrainment (including cloud base entrainment) and detrainment which may be adapted from existing frameworks such as Arakawa and Schubert (1974), Betts and Miller (1993), Neggers et al. (2002) and Siebesma et al. (2007). Weller and McIntyre (2019) proposed a numerical scheme for transfers in a multi-fluid model, but only one transfer scheme was considered in which the numerical treatment of the mass transfer is explicit which may not be suitable for fast transfers. The numerical transfer scheme in Weller and McIntyre (2019) also used an unintuitive combination of explicit and implicit terms in the transfer scheme (as using only explicit or implicit terms produced a non-conservative scheme). This motivates us to present a range of possible mass transfer schemes and analyse their numerical properties to obtain the most desirable numerical solutions. For use in a multi-fluid convection model, the numerical solutions for the transfer schemes must:

- Maintain positivity of mass (noted as a numerical stability condition in Weller and McIntyre, 2019).
- Keep velocities and temperatures bounded to prevent new extrema.
- Conserve momentum.
- Conserve energy where possible.
- Never cause increases in total energy to prevent numerical instabilities.
- Be as accurate as possible.

In this chapter, we analyse the numerical properties of the transfer terms between fluids for the multi-fluid compressible Euler equations (defined in section 3.1). We formulate 20 possible numerical schemes and analyse their properties in section 3.2. We then apply the transfer terms to well-resolved two-fluid dry convection test cases in section 3.3.

3.1 Governing equations

The multi-fluid compressible Euler equations were derived in Thuburn et al. (2018) and were presented in flux form in chapter 1. Using the notation convection from Weller and McIntyre (2019), we will use three prognostic equations for each fluid including the continuity equation,

$$\frac{\partial \eta_i}{\partial t} + \boldsymbol{\nabla}.(\eta_i \boldsymbol{u}_i) = \underbrace{\sum_{j \neq i} (\eta_j S_{ji} - \eta_i S_{ij})}_{\text{Mass transfers}}, \tag{3.1}$$

the potential temperature equation in advective form,

$$\frac{\partial \theta_i}{\partial t} + \boldsymbol{u}_i.\boldsymbol{\nabla}\theta_i = \underbrace{\sum_{j \neq i} \left(\frac{\eta_j}{\eta_i} S_{ji} (\theta_j - \theta_i) \right)}_{\text{Transfer mean temp.}} - \underbrace{\sum_{j \neq i} H_{ij}}_{\text{Heat transfer}}, \tag{3.2}$$

and the momentum equation in advective form,

$$\frac{\partial \boldsymbol{u}_i}{\partial t} + \boldsymbol{u}_i.\boldsymbol{\nabla}\boldsymbol{u}_i = \boldsymbol{g} - \underbrace{c_p \theta_i \boldsymbol{\nabla}\pi}_{\text{Pressure gradient}} + \underbrace{\sum_{j \neq i} \left(\frac{\eta_j}{\eta_i} S_{ji} (\boldsymbol{u}_j - \boldsymbol{u}_i) \right)}_{\text{Transfer mean velocity.}} - \underbrace{\sum_{j \neq i} \boldsymbol{D}_{ij}}_{\text{Drag}}, \tag{3.3}$$

where i is the label for fluid i. Our prognostic variables are the fluid mass per unit volume (η_i), the fluid potential temperature (θ_i) and the fluid velocity ($\boldsymbol{u}_i$). We have defined $\eta_i \equiv \sigma_i \rho_i$, where σ_i is the fluid volume fraction and ρ_i is the density of fluid i. S_{ij} is the unidirectional mass transfer rate from fluid i to fluid j ($S_{ij} \geq 0$). c_p is the heat capacity of dry air at constant pressure and $\boldsymbol{g}$ is the gravitational acceleration. $\pi \equiv p^\kappa / p_0^\kappa$ is the Exner pressure where p is the pressure, p_0 is a reference pressure, $\kappa = R/c_p$ and R is the gas constant of dry air. H_{ij} is the heat transfer between fluids i and j (which does not exchange mass between fluids) and $\boldsymbol{D}_{ij}$ is the drag between fluids i and j - these exchange terms will not be used in this study. Additionally, the equation of state for dry air is used to relate the pressure and fluid temperatures:

$$p_0 \pi^{\frac{1-\kappa}{\kappa}} = R \sum_i \eta_i \theta_i. \tag{3.4}$$

The total energy of the multi-fluid system is given by

$$E = E_P + E_I + E_K \tag{3.5}$$

where E_P is the potential energy, E_I is the internal energy and E_K is the kinetic energy, defined respectively as:

$$E_P = \sum_i \eta_i |\boldsymbol{g}| z, \tag{3.6}$$

$$E_I = \sum_i \eta_i \theta_i c_v \pi, \tag{3.7}$$

$$E_K = \sum_i \frac{1}{2} \eta_i \boldsymbol{u}_i . \boldsymbol{u}_i, \tag{3.8}$$

where z is the height coordinate and $c_v = \frac{c_p}{\gamma}$ is the heat capacity of dry air at constant volume and γ is the heat capacity ratio. These energies will be used to assess the numerical stability of the transfer schemes.

3.2 Fluid transfer schemes

In convection modelling, entrainment and detrainment are both mass exchanges between the updraft and surrounding environment. It is therefore important that the numerical implementation of these transfer terms for a multi-fluid system have accurate conservation properties and that they do not produce new extrema. For accuracy, mass and momentum should be conserved. For stability, the fluid mass (η_i) must remain positive and velocities should be bounded. For accuracy and stability, potential and internal energy should also be conserved. In addition, the kinetic energy should not increase as resolved kinetic energy decreases when two fluids of differing velocity mix. In reality, any sink of grid-scale energy should be a source of turbulent kinetic energy which, in turn, may be a source of internal energy - as we are not modelling sub-filter-scale variability in this study, we will be ignoring these effects. In this section, we demonstrate the conservation and boundedness properties of the mass transfer terms for the multi-fluid equations and present solutions of the multi-fluid Euler equations with these transfers.

3.2.1 Notation and numerics

In our governing equations, we have assumed that mass transferred between fluids will take its associated mean properties from the original fluid. Refinement of the transfer terms to incorporate sub-filter-scale variation will not form part of this study. For a

mean fluid property $\phi_i \in [\theta_i, \boldsymbol{u}_i]$, the governing equations can be generalised as

$$\frac{\partial \phi_i}{\partial t} + \boldsymbol{u}_i.\boldsymbol{\nabla}\phi_i = F_i + \sum_{j \neq i} S_{ji} \frac{\eta_j}{\eta_i} \left[\phi_j - \phi_i\right], \tag{3.9}$$

where F_i contains right-hand-side terms such as the pressure gradient term. Applying this to the temperature and momentum equations we get:

- Momentum equation: $\boldsymbol{\phi}_i = \boldsymbol{u}_i$, $\boldsymbol{F}_{\boldsymbol{u}i} = -c_p\theta_i\boldsymbol{\nabla}\pi + \boldsymbol{g}$.
- Temperature equation: $\phi_i = \theta_i$, $\boldsymbol{F}_{\theta i} = 0$.

We will assume that the transfer terms are operator split such that other processes (advection and F_i) act on the prognostic variables first, followed by the transfers:

$$\phi_i^m = \phi_i^n - (1-\alpha)\Delta t \left[\boldsymbol{u}_i.\boldsymbol{\nabla}\phi_i - F_i\right]^n + \alpha\Delta t \left[\boldsymbol{u}_i.\boldsymbol{\nabla}\phi_i - F_i\right]^m, \tag{3.10}$$

$$\phi_i^{n+1} = \phi_i^m + \Delta t \sum_{j \neq i} S_{ji} \frac{\eta_j}{\eta_i} \left[\phi_j - \phi_i\right], \tag{3.11}$$

where n is the time-level ($t = n\Delta t$), m is the time-level after applying the advection and F_i terms, and α is the Crank-Nicolson off-centering coefficient. The numerical treatment of the transfer terms will be discussed in section 3.2.3. The mass transfers are then based on the most up-to-date states (m) rather than the previous time-level (n). This allows the transfer terms to be independent of the numerical properties of the advection and F_i terms. For each momentum equation, the total momentum should be equal before (m) and after ($n+1$) mass transfer such that: $\sum_i \eta_i^{n+1}\boldsymbol{u}_i^{n+1} = \sum_i \eta_i^m \boldsymbol{u}_i^m$. The internal energy should also be conserved by the temperature equation transfers: $c_v\pi\sum_i \eta_i^{n+1}\theta_i^{n+1} = c_v\pi\sum_i \eta_i^m\theta_i^m$.

As the transfer terms involve a division by η_i, we will replace $1/\eta_i$ with $1/\max(\eta_i, 10^{-16}\text{kg m}^{-3})$ in any numerical method to avoid issues when one fluid vanishes.

3.2.2 Transferring mass

When transferring mass, we must ensure that mass is conserved and all η_i remain positive. The mass in each fluid at the end of the timestep (η_i^{n+1}) is given by the mass after advection (η_i^m) plus the discretised transfer term integrated over time Δt:

$$\begin{aligned}
\eta_0^{n+1} &= \eta_0^m - \Delta t \left[(1-\alpha_C)\,\eta_0^m + \alpha_C\,\eta_0^{n+1}\right] S_{01} + \Delta t \left[(1-\alpha_C)\,\eta_1^m + \alpha_C\,\eta_1^{n+1}\right] S_{10}, \\
\eta_1^{n+1} &= \eta_1^m - \Delta t \left[(1-\alpha_C)\,\eta_1^m + \alpha_C\,\eta_1^{n+1}\right] S_{10} + \Delta t \left[(1-\alpha_C)\,\eta_0^m + \alpha_C\,\eta_0^{n+1}\right] S_{01},
\end{aligned} \tag{3.12}$$

where α_C determines the numerical treatment of transfer terms in the continuity equation: transfers are conducted explicitly if $\alpha_C = 0$ and implicitly if $\alpha_C = 1$. Re-arranging these equations for η_i^{n+1}, we get

$$\begin{aligned} \eta_0^{n+1} &= (1 - \lambda_{C01})\eta_0^m + \lambda_{C10}\,\eta_1^m, \\ \eta_1^{n+1} &= (1 - \lambda_{C10})\eta_1^m + \lambda_{C01}\,\eta_0^m, \end{aligned} \tag{3.13}$$

where

$$\lambda_{Aij} \equiv \frac{\Delta t S_{ij}}{1 + \alpha_A \Delta t (S_{ji} + S_{ij})} \tag{3.14}$$

and A is a label used to identify the coefficients α and λ. We use $A = C$ in the continuity equation (mass transfers) and we will later use $A = M$ and $A = T$ for momentum and temperature transfers respectively. The total mass is clearly conserved as $\sum_i \eta_i^{n+1} = \sum_i \eta_i^n$ and the total potential energy is also conserved. λ_{ij} is between 0 and 1 for all α_A when $\Delta t S_{ij} \leq 1$, meaning η_0 and η_1 remain positive. When $\alpha_A = 1$, any positive $\Delta t S_{ij} > 0$ may be used.

3.2.3 Transferring fluid properties - Method 1

We must also model the transfer of velocity and temperature associated with the relabelling of mass between fluids described in section 3.2.2. The new value of the variable $\phi_i \in [\theta_i, \boldsymbol{u}_i]$ should be bounded by the old values of fluids i and j (at time level m) so that new extrema are not generated. Also, momentum should be conserved and energy should not increase. Assuming operator-split transfers, the new fluid properties for fluids 0 and 1 are written as

$$\begin{aligned} \phi_0^{n+1} &= \phi_0^m - (1 - \alpha_A)\Delta t\, \frac{\eta_1^q}{\eta_0^r} S_{10}(\phi_0^m - \phi_1^m) - \alpha_A\, \Delta t\, \frac{\eta_1^q}{\eta_0^r} S_{10}(\phi_0^{n+1} - \phi_1^{n+1}), \\ \phi_1^{n+1} &= \phi_1^m - (1 - \alpha_A)\Delta t\, \frac{\eta_0^q}{\eta_1^r} S_{01}(\phi_1^m - \phi_0^m) - \alpha_A\, \Delta t\, \frac{\eta_0^q}{\eta_1^r} S_{01}(\phi_1^{n+1} - \phi_0^{n+1}), \end{aligned} \tag{3.15}$$

where ϕ_i^m are the values after advection. If $\alpha_A = 0$, then ϕ_i is treated explicitly and $\alpha_A = 1$ means ϕ_i is treated implicitly. Note that these equations have additional degrees of freedom in the time-level choice for η_i, where q and r are the time level choices for the numerator and denominator respectively. A is the label for each governing equation. For the momentum and temperature equations, we will use $A = M$ and $A = T$ respectively.

Rearranging for ϕ_i^{n+1}, we obtain

$$\begin{aligned}\phi_0^{n+1} &= (1-\nu_{A10}^{q,r})\phi_0^m + \nu_{A10}^{q,r}\phi_1^m,\\ \phi_1^{n+1} &= (1-\nu_{A01}^{q,r})\phi_1^m + \nu_{A01}^{q,r}\phi_0^m,\end{aligned} \tag{3.16}$$

where

$$\nu_{Aij}^{q,r} = \frac{\Delta t S_{ij}\frac{\eta_i^q}{\eta_j^r}}{1+\alpha_A\Delta t\left[S_{ij}\frac{\eta_i^q}{\eta_j^r}+S_{ji}\frac{\eta_j^q}{\eta_i^r}\right]}. \tag{3.17}$$

With two degrees of freedom in each of α_C, α_A, q and r, a total of 16 different transfer schemes exist using this method. In appendix A.1, we derive the momentum/internal energy conservation properties for the following four schemes:

1. $\alpha_C = 0$, $\alpha_M = \alpha_T = 0$ with $q = m$, $r = n+1$.
2. $\alpha_C = 0$, $\alpha_M = \alpha_T = 1$ with $q = m$, $r = m$.
3. $\alpha_C = 1$, $\alpha_M = \alpha_T = 0$ with $q = n+1$, $r = n+1$.
4. $\alpha_C = 1$, $\alpha_M = \alpha_T = 1$ with $q = n+1$, $r = m$.

The other 12 schemes do not conserve momentum/internal energy - we prove this by presenting numerical analysis of the conservation properties. The relative momentum changes ($\Delta F_{\mathrm{REL}} \equiv (F^{n+1}-F^m)/F^0$) due to the transfer schemes are calculated using initial conditions which cover a large parameter range, including conditions observed in convective clouds. The transfer schemes were initiated with $\eta_0^m = 1$ kg m^{-3}, $u_0^m = 1$ ms^{-1}, $\theta_0^m = 300$ K, $\theta_1^m = 301$ K, $S_{01} = 1$ s^{-1}. We also use Δt in the range $[0,5]$ s, η_1^m in the range $[10^{-8},2]$ kg m^{-3}, u_1^m in the range $[-150,150]$ ms^{-1} and S_{10} in the range $[0,1]$ s^{-1} - each uniformly discretised 50 times. For a given timestep, 1.25×10^5 transfers are therefore tested and the range of the relative momentum change for each scheme is plotted. This is shown in figure 3.1. These results confirm the momentum conservation analysis of schemes 1-4 (the relative momentum change for these schemes is always zero). The other 12 schemes do not conserve momentum (or internal energy) and will not be analysed further.

Note that the schemes that treat all prognostic variables explicitly ($\alpha_C = 0$, $\alpha_M = \alpha_T = 0$, $q = m$, $r = m$) or implicitly ($\alpha_C = 1$, $\alpha_M = \alpha_T = 1$, $q = n+1$, $r = n+1$) are not among the conservative schemes. It was because of this that scheme 2 was chosen in Weller and McIntyre (2019).

Boundedness is also an important property for a stable numerical scheme. ϕ will remain bounded if $\nu_{ij}^{q,r} \in [0,1]$ which is guaranteed if $\alpha_A = 1$ (see appendix A.2),

a) $q = m$ and $r = n + 1$, including scheme 1

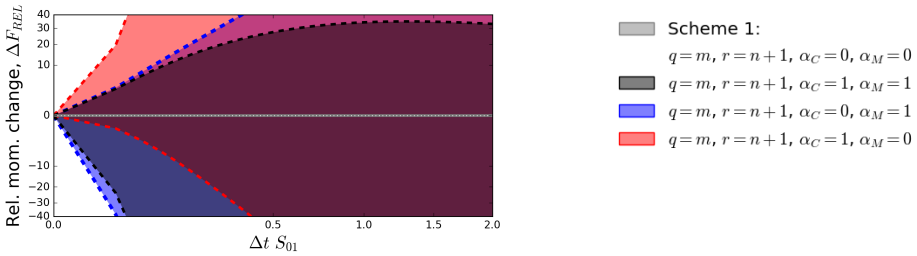

b) $q = m$ and $r = m$, including scheme 2

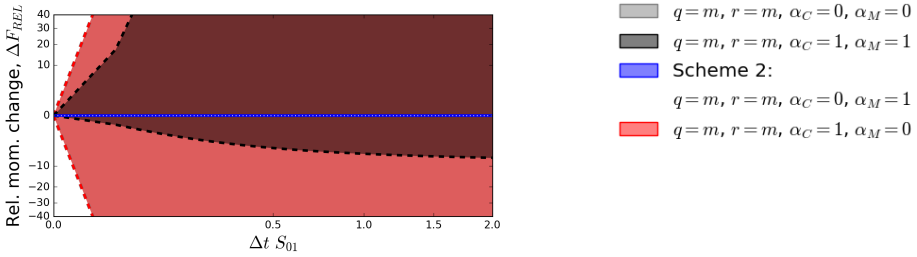

c) $q = n + 1$ and $r = n + 1$, including scheme 3

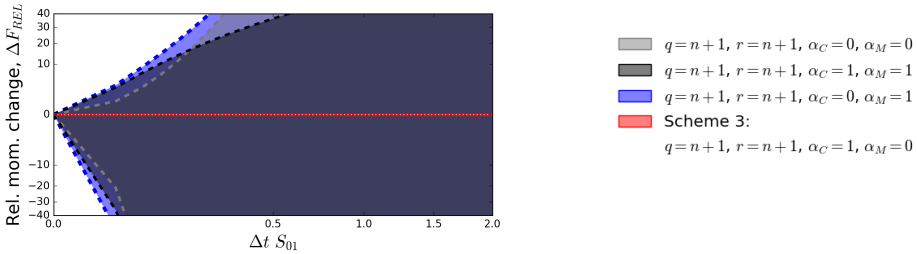

d) $q = n + 1$ and $r = m$, including scheme 4

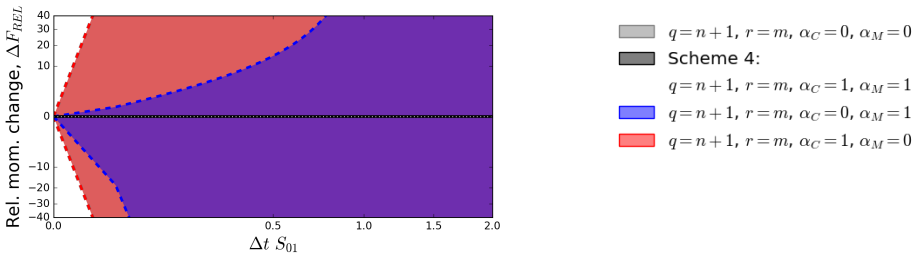

Figure 3.1: The range of momentum changes (relative to initial conditions) of the 16 transfer schemes for method 1. For each scheme, we conduct transfers with initial parameters which include conditions expected in the atmosphere. Schemes are momentum conserving if the relative momentum change due to the transfer is always zero, as indicated by the dotted white line. Schemes which conserve momentum are shown with solid lines whereas dashed lines are used for non-conserving schemes. The conserving schemes are scheme 1 (panel a, grey), scheme 2 (panel b, blue), scheme 3 (panel c, red) and scheme 4 (panel d, black). Square-root scales are used for both axes. They grey and red profiles in panels b and d overlap with the red profile shown on top.

meaning schemes 2 and 4 are bounded. A special case also exists for scheme 1 which ensures values of ϕ remain bounded for $\Delta t S_{ij} \leq 1$. Figure 3.2.a shows the relative energy changes ($\Delta E_{\text{REL}} \equiv (E^{n+1} - E^m)/E^0$) of schemes 1-4 over the same range of

parameter space used in figure 3.1. Schemes 2 (blue) and 4 (black) do not increase the total kinetic energy of the system for any $\Delta t S_{ij} > 0$ and scheme 1 (grey) for $\Delta t S_{ij} \leq 1$. Scheme 3 (red) may produce large energy increases for any $\Delta t S_{ij}$ due to unbounded velocities which cause increases in kinetic energy. The energy analysis comprehensively samples the parameter-space which is useful for convection modelling, but these results do not concretely prove that schemes 2 and 4 are always energy diminishing. We should therefore also consider other transfer methods with known energy properties.

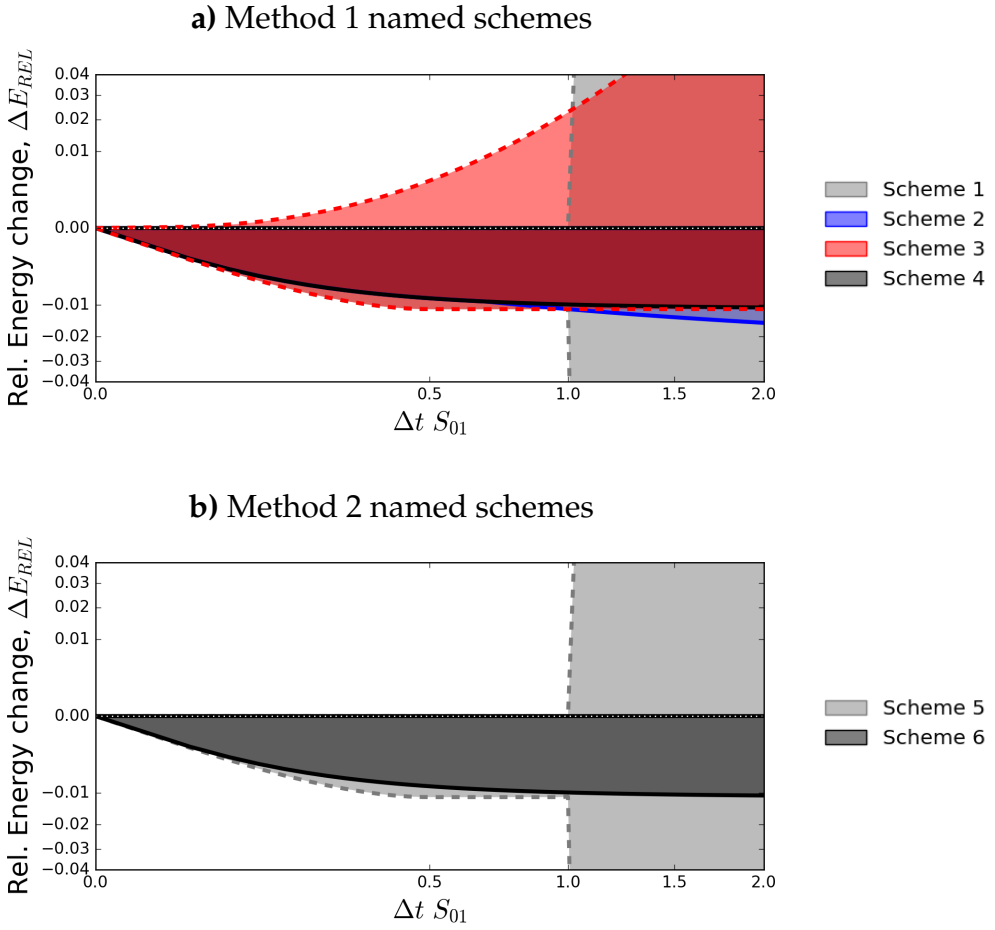

Figure 3.2: The range of relative energy changes of schemes 1-4 (panel a) and schemes 5 & 6 (panel b). The minimum and maximum energy changes are calculated using the same parameter-space range as figure 3.1. Schemes are energy-diminishing if the relative energy change due to the transfer is never above zero, indicated by the dotted white line. Energy diminishing and energy producing schemes are shown with solid and dashed lines respectively. Scheme 2 (panel a, blue), scheme 4 (panel a, black) and scheme 6 (panel b, black) are energy diminishing. Scheme 1 (panel a, grey) and scheme 5 (panel b, grey) also have energy-diminishing properties for $\Delta t S_{ij} \leq 1$. Although schemes 2 and 4 behave similarly for $\Delta t S_{ij} \leq 1$, the profiles are not identical. Square-root scales are used for both axes.

3.2.4 Transferring fluid properties - Method 2 (Mass-weighted transfers)

Transfer terms can also be obtained by considering the flux form equations,

$$\frac{\partial(\eta_i\phi_i)}{\partial t} + \boldsymbol{\nabla}.(\eta_i\phi_i\boldsymbol{u}_i) = \eta_i F_i + \sum_j \left[S_{ji}\eta_j\phi_j - S_{ij}\eta_i\phi_i\right], \tag{3.18}$$

which are obtained by combining the continuity equation 3.1 and equation 3.9 with the chain rule. These transfers unconditionally guarantee the conservation of $\eta_i\phi_i$ (momentum and internal energy) as with the mass transfers seen in section 3.2.2. By defining our mass-weighted quantity as $\Phi_i \equiv \eta_i\phi_i$, we get:

$$\begin{aligned}
\Phi_0^{n+1} &= \Phi_0^m - \Delta t\left[(1-\alpha_A)\,\Phi_0^m + \alpha_A\,\Phi_0^{n+1}\right] S_{01} + \Delta t\left[(1-\alpha_A)\,\Phi_1^m + \alpha_A\,\Phi_1^{n+1}\right] S_{10},\\
\Phi_1^{n+1} &= \Phi_1^m - \Delta t\left[(1-\alpha_A)\,\Phi_1^m + \alpha_A\,\Phi_1^{n+1}\right] S_{10} + \Delta t\left[(1-\alpha_A)\,\Phi_0^m + \alpha_A\,\Phi_0^{n+1}\right] S_{01}.
\end{aligned} \tag{3.19}$$

These transfers take a similar form to (3.12), meaning we get the solution,

$$\begin{aligned}
\Phi_i^m &\equiv \eta_i^m\phi_i^m\\
\Phi_0^{n+1} &= (1-\lambda_{A01})\Phi_0^m + \lambda_{A10}\,\Phi_1^m,\\
\Phi_1^{n+1} &= (1-\lambda_{A10})\Phi_1^m + \lambda_{A01}\,\Phi_0^m,\\
\phi_i^{n+1} &= \frac{\Phi_i^{n+1}}{\eta_i^{n+1}}.
\end{aligned} \tag{3.20}$$

We have proposed this alternative method as we can demonstrate that the total kinetic energy of the system never increases when $\alpha_C = \alpha_A$ (see appendix A.3). In appendix A.2, we also show that ϕ_i is bounded when mass and momentum transfers are treated consistently ($\alpha_C = \alpha_A$) - we will therefore not consider schemes where $\alpha_C \neq \alpha_A$. Using purely explicit or purely implicit treatments, we therefore have 2 more viable transfer schemes for the multi-fluid equations:

5. $\alpha_C = 0, \alpha_A = \alpha_M = \alpha_T = 0.$

6. $\alpha_C = 1, \alpha_A = \alpha_M = \alpha_T = 1.$

Note that schemes such as $[\alpha_C = 0.5,\ \alpha_A = 0.5]$ can also be used but there is no increase in order of accuracy as the scheme is operator-split and thus the time level m is not that of the previous timestep. Using time level n instead of m introduces instabilities into the numerical method as updates from the prognostic equations such as advection will be ignored in the transfer scheme. Figure 3.2.b shows the relative energy changes of schemes 5 and 6 over the same parameter space range used for method 1 schemes. The energy changes are consistent with the analysis in appendix A.3, whereby scheme 5

never increases in energy for $\Delta t S_{ij} \leq 1$ and scheme 6 for $\Delta t S_{ij} > 0$.

3.2.5 Transfers on a staggered grid

So far, we have assumed that our mass transfers are conducted in the same location, i.e. on a co-located grid (A-grid). But how do the numerical methods change when using staggered grid? Following the 2D C-grid setup used in Weller and McIntyre (2019), we keep our prognostic mass and temperature defined at cell centres and define our velocities on cell faces. Henceforth, a cell-centred variable (μ) which is linearly-interpolated onto cell faces will be denoted by $[\mu]_f$ and a variable defined on cell faces will be denoted by $[\mu]_c$ when it is interpolated onto the cell-centres.

The numerical transfer schemes for the mass and potential temperature remain the same, but some adjustments must be made for the velocity transfers (method 1):

$$\begin{aligned} \boldsymbol{u}_0^{n+1} &= \left(1 - [\nu_{M10}^{q,r}]_f\right)\ \boldsymbol{u}_0^m + [\nu_{M10}^{q,r}]_f\ \boldsymbol{u}_1^m, \\ \boldsymbol{u}_1^{n+1} &= \left(1 - [\nu_{M01}^{q,r}]_f\right)\ \boldsymbol{u}_1^m + [\nu_{M01}^{q,r}]_f\ \boldsymbol{u}_0^m. \end{aligned} \tag{3.21}$$

$[\nu_{M10}^{q,r}]_f$ has various degrees of freedom in the choice of interpolations, such as $[S_{ij}]_f \frac{[\eta_i^q]_f}{[\eta_j^r]_f}$ or $\left[S_{ij}\frac{\eta_i^q}{\eta_j^r}\right]_f$, for example. We will use $\frac{[S_{ij}\ \eta_i^q]_f}{[\eta_j^r]_f}$, once again following Weller and McIntyre (2019). The momentum transfers for method 2 become

$$\begin{aligned} N_0^{n+1} &\equiv \left(1 - [\lambda_{C01}]_f\right)\ [\eta_0^m]_f + [\lambda_{C10}]_f\ [\eta_1^m]_f, \\ N_1^{n+1} &\equiv \left(1 - [\lambda_{C10}]_f\right)\ [\eta_1^m]_f + [\lambda_{C01}]_f\ [\eta_0^m]_f, \\ \boldsymbol{F}_i^m &\equiv [\eta_i^m]_f \boldsymbol{u}_i^m \\ \boldsymbol{F}_0^{n+1} &= \left(1 - [\lambda_{M01}]_f\right)\ \boldsymbol{F}_0^m + [\lambda_{M10}]_f\ \boldsymbol{F}_1^m, \\ \boldsymbol{F}_1^{n+1} &= \left(1 - [\lambda_{M10}]_f\right)\ \boldsymbol{F}_1^m + [\lambda_{M01}]_f\ \boldsymbol{F}_0^m. \\ \boldsymbol{u}_i^{n+1} &= \frac{\boldsymbol{F}_i^{n+1}}{N_i^{n+1}}, \end{aligned} \tag{3.22}$$

where $[\lambda_{Aij}]_f = \frac{\Delta t [S_{ij}]_f}{1+\alpha_M \Delta t([S_{ji}]_f + [S_{ij}]_f)}$. N_i is the fluid mass calculated by conducting the mass transfers on the cell faces - this aids in a consistent and accurate conversion of the mass flux to the fluid velocity. With velocities defined on cell faces, the kinetic energy is calculated on the faces and then interpolated back onto the cell centres:

$$E_K^{n+1} = \sum_i \frac{1}{2}\left[N_i^{n+1}(w_i^{n+1})^2\right]_c. \tag{3.23}$$

This interpolation method ensures kinetic energy is conserved when converting to the cell centre values (Ringler et al., 2010).

3.2.6 Summary of proposed transfer terms

We have presented 6 numerical transfer schemes which maintain positivity of mass and conserve mass, momentum, potential energy and internal energy for $\Delta t S_{ij} \leq 1$. These schemes are presented in table 3.1.

	Scheme	Positive η_i?	Bounded θ_i & u_i?	Momentum & IE conserved?	KE decreases?
	Method 1				
1	$\alpha_C = 0, \alpha_A = 0, q = m, r = n+1$	✓	✗	✓✓	(✓)
2	$\alpha_C = 0, \alpha_A = 1, q = m, r = m$	✓	✓✓	✓✓	(✓✓)
3	$\alpha_C = 1, \alpha_A = 0, q = n+1, r = n+1$	✓✓	✗	✓✓	✗
4	$\alpha_C = 1, \alpha_A = 1, q = n+1, r = m$	✓✓	✓✓	✓✓	(✓✓)
	Other schemes	✓	✓ for $\alpha_A = 1$	✗	✗
	Method 2 (Mass-weighted transfers)				
5	$\alpha_C = 0, \alpha_A = 0$	✓	✓	✓✓	✓
6	$\alpha_C = 1, \alpha_A = 1$	✓✓	✓✓	✓✓	✓✓
	Other schemes	✓	✓ for $\alpha_C = \alpha_A$	✓✓	✓ for $\alpha_C = \alpha_A$

Table 3.1:: The transfer properties of the transfer schemes from methods 1 and 2. Schemes 4 and 6 have all of the ideal transfer properties. In this study, we have not shown that schemes 1 or 4 always decrease energy but we have observed no energy increases in idealised test cases. Ticks indicate that the scheme fulfils the given property for $\Delta t S_{ij} \leq 1$, double ticks show that the property also occurs for all $\Delta t S_{ij} > 0$ and crosses mean the property is not fulfilled. Properties which have not been proven but have been numerically verified (in figure 3.2) are shown in brackets.

Schemes 2, 4, 5 and 6 keep the fluid temperatures and velocities bounded, although schemes 2 and 5 only do this for $\Delta t S_{ij} \leq 1$. Only schemes 2, 4 and 6 are kinetic-energy-diminishing for all timesteps meaning schemes 1, 3 and 5 can cause numerical instabilities if $\Delta t S_{ij}$ is large. From our analysis, we recommend scheme 4,

$$\begin{aligned}
\eta_i^{n+1} &= \left(1 - \frac{\Delta t S_{ij}}{1 + \Delta t S_{ji} + \Delta t S_{ij}}\right) \eta_i^m + \frac{\Delta t S_{ji}}{1 + \Delta t S_{ji} + \Delta t S_{ij}} \eta_j^m \\
\phi_i^{n+1} &= \left(1 - \frac{\Delta t S_{ji} \frac{\eta_j^{n+1}}{\eta_i^m}}{1 + \Delta t S_{ij} \frac{\eta_i^{n+1}}{\eta_j^m} + \Delta t S_{ji} \frac{\eta_j^{n+1}}{\eta_i^m}}\right) \phi_i^m + \frac{\Delta t S_{ji} \frac{\eta_j^{n+1}}{\eta_i^m}}{1 + \Delta t S_{ij} \frac{\eta_i^{n+1}}{\eta_j^m} + \Delta t S_{ji} \frac{\eta_j^{n+1}}{\eta_i^m}} \phi_j^m,
\end{aligned} \tag{3.24}$$

and scheme 6,

$$\begin{aligned}
\eta_i^{n+1} &= \left(1 - \frac{\Delta t S_{ij}}{1 + \Delta t S_{ji} + \Delta t S_{ij}}\right) \eta_i^m + \frac{\Delta t S_{ji}}{1 + \Delta t S_{ji} + \Delta t S_{ij}} \eta_j^m \\
\phi_i^{n+1} &= \frac{\left(1 - \frac{\Delta t S_{ij}}{1 + \Delta t S_{ji} + \Delta t S_{ij}}\right) \eta_i^m \phi_i^m + \frac{\Delta t S_{ji}}{1 + \Delta t S_{ji} + \Delta t S_{ij}} \eta_j^m \phi_j^m}{\eta_i^{n+1}},
\end{aligned} \tag{3.25}$$

as they are fully implicit and fulfil all the numerical criteria we have set. Scheme 2 is also a viable scheme if the transfer rate is limited to $\Delta t S_{ij} \leq 1$ to maintain positive mass. Section 3.3 will test these schemes on 2D staggered grids.

3.3 Rising bubble test cases

In order to test the properties of the various transfer schemes on a staggered grid, we have implemented them into the multi-fluid fully compressible Euler equation solver from Weller and McIntyre (2019) using operator splitting. We will run test cases adapted from the single-fluid rising bubble test case (defined in Bryan and Fritsch, 2002) where an initially stationary temperature anomaly rises and generates resolved circulations (see figure 3.3). The domain extends to $x \in [-10, 10]$ km and $z \in [0, 10]$ km with uniform grid spacings $\Delta x = \Delta z = 100$ m and wall boundaries on all sides (where zero-gradient fields are imposed and no fluxes perpendicular to the boundaries). A uniform potential temperature field of $\theta = 300$ K is initially chosen with the system in hydrostatic balance and zero velocity. A warm temperature perturbation is then applied at $t = 0$ s:

$$\theta' = 2 \cos^2 \left(\frac{\pi}{2} L\right). \tag{3.26}$$

The perturbation is only applied for $L \leq 1$ where $L \equiv \sqrt{\frac{x - x_c}{x_r} + \frac{z - z_c}{z_r}}$, $x_c = 10$ km, $z_c = 2$ km and $x_r = z_r = 2$ km. For the 2-fluid experiments the warm anomaly will be

applied to θ_1 only, whereas fluid 0 will remain initialised as $\theta_0 = 300$ K.

We use a 2D C-grid with η_i and θ_i defined at cell centres and the normal component of $\boldsymbol{u}_i$ defined at cell faces. The time-stepping is centred Crank-Nicolson with a timestep of $\Delta t = 2$ s. A van-Leer advection scheme is chosen to maintain positivity of the mass of each fluid. All details of the numerical setup and the numerical solvers used are described in Weller and McIntyre (2019), with the exception of a numerical adjustment which must be made for an operator-split Crank-Nicolson multi-fluid scheme (described in appendix B).

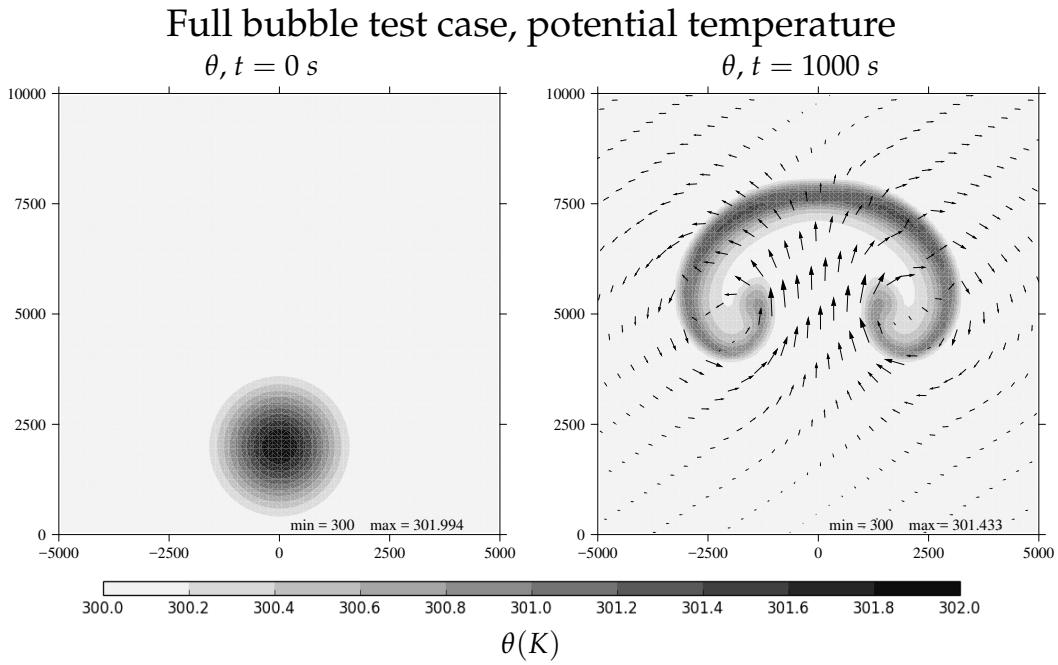

Figure 3.3: The temperature profile evolution of the full bubble test case, which has the same analytical solution as the single-fluid test case from Bryan and Fritsch (2002). The warm anomaly rises and induces large-scale resolved circulations. The black arrows give the relative magnitudes and directions of the velocity vectors.

3.3.1 Full bubble test case

The first test case is initialised with all mass in fluid 1: $\sigma_0 = 0$, $\sigma_1 = 1$. The transfer rate is chosen to transfer a large quantity of fluid 1 to fluid 0:

$$S_{01} = 0, \tag{3.27}$$

$$S_{10} = \frac{1}{\Delta t\, \eta_1^m} \max\left(0,\, \sigma_{\min} \rho_0^m - \eta_0^m\right), \tag{3.28}$$

where $\sigma_{\min} = 0.1$. This means that the explicit schemes will transfer 10% of the mass in the first timestep (and none thereafter). As fluid 0 initially has no mass, it should inherit the properties of fluid 1 when mass is transferred. We therefore expect the solution to be the same as the single-fluid test case shown in figure 3.3.

The test case is run for all 20 transfer schemes, including the non-conservative schemes. For each scheme we calculate the relative energy change from the single fluid test case:

$$\Delta E^n_{RSF} = \frac{E^n_{MF} - E^n_{SF}}{E^0_{SF}}, \tag{3.29}$$

where E^n_{SF} and E^n_{MF} are the total energies at timestep n for the single-fluid and multi-fluid simulations respectively. With a float precision up to 16 decimal places, we expect fluid 0 to inherit the density, velocity and temperature of fluid 1 to machine precision. A relative energy change of $\Delta E^n_{RSF} \sim 10^{-15}$ is therefore reasonable for an energy conserving scheme.

Name	**Method**	α_C	α_A	q	r	ΔE^1_{RSF}	ΔE^{500}_{RSF}	$\Delta \theta^{500}_{RMS}$	Δw^{500}_{RMS}
Scheme 1	1	0	0	m	$n+1$	$\mathbf{-1.18 \times 10^{-14}}$	$\mathbf{-4.71 \times 10^{-15}}$	1.24×10^{-13}	1.08×10^{-12}
–	1	0	1	m	$n+1$	$+6.77 \times 10^{-7}$	-1.34×10^{-6}	4.98×10^{-1}	6.84×10^{-2}
–	1	1	0	m	$n+1$	-1.23×10^{-7}	-1.97×10^{-6}	8.48×10^{-1}	3.48×10^{-3}
–	1	1	1	m	$n+1$	$+5.85 \times 10^{-7}$	-2.35×10^{-6}	4.79×10^{-1}	6.38×10^{-2}
–	1	0	0	m	m	$+1.05 \times 10^{11}$	–	–	–
Scheme 2	1	0	1	m	m	$\mathbf{-1.18 \times 10^{-14}}$	$\mathbf{-7.07 \times 10^{-15}}$	3.14×10^{-13}	8.81×10^{-13}
–	1	1	0	m	m	$+9.51 \times 10^{10}$	–	–	–
–	1	1	1	m	m	$\mathbf{-1.18 \times 10^{-15}}$	$\mathbf{-6.73 \times 10^{-15}}$	5.78×10^{-14}	2.63×10^{-12}
–	1	0	0	$n+1$	$n+1$	$+1.35 \times 10^{-7}$	-6.53×10^{-6}	3.93×10^{-1}	2.57×10^{-2}
–	1	0	1	$n+1$	$n+1$	$+7.12 \times 10^{-7}$	-1.07×10^{-6}	5.18×10^{-1}	6.41×10^{-2}
Scheme 3	1	1	0	$n+1$	$n+1$	$\mathbf{-1.18 \times 10^{-15}}$	$\mathbf{-6.56 \times 10^{-15}}$	1.75×10^{-13}	2.04×10^{-12}
–	1	1	1	$n+1$	$n+1$	$+6.15 \times 10^{-7}$	-2.00×10^{-6}	4.86×10^{-1}	6.87×10^{-2}
–	1	0	0	$n+1$	m	$+8.47 \times 10^{10}$	–	–	–
–	1	0	1	$n+1$	m	$\mathbf{-1.18 \times 10^{-14}}$	$\mathbf{-4.71 \times 10^{-15}}$	3.51×10^{-13}	1.95×10^{-12}
–	1	1	0	$n+1$	m	$+7.86 \times 10^{10}$	–	–	–
Scheme 4	1	1	1	$n+1$	m	$\mathbf{-1.18 \times 10^{-15}}$	$\mathbf{-8.75 \times 10^{-15}}$	1.05×10^{-13}	1.64×10^{-12}
Scheme 5	2	0	0	–	–	$\mathbf{-1.18 \times 10^{-14}}$	$\mathbf{-3.87 \times 10^{-15}}$	6.92×10^{-12}	4.00×10^{-13}
–	2	0	1	–	–	$+5.13 \times 10^{-14}$	–	–	–
–	2	1	0	–	–	$+4.58 \times 10^{-14}$	–	–	–
Scheme 6	2	1	1	–	–	$\mathbf{-1.18 \times 10^{-15}}$	$\mathbf{-3.19 \times 10^{-15}}$	4.82×10^{-11}	6.25×10^{-13}

Table 3.2:: The relative energy changes and the RMS errors of potential temperature and vertical velocity, for the 2-fluid rising bubble test case relative to the single-fluid test case. Energy changes are shown for the first timestep ($n = 1$) where the transfers are largest and after 1000 s ($n = 500$). Given the machine precision, a relative energy change of the order 10^{-15} is expected for energy conservation - results around this range are indicated in bold.

The energy changes for all schemes are shown in table 3.2 as well as the root-mean-squared (RMS) errors for the potential temperature and vertical velocity fields. All six conservative schemes produce small energy decreases after one timestep with the implicit mass schemes (3, 4 and 6) producing the smallest energy changes with $\Delta E^1_{RSF} = -1.18 \times 10^{-15}$ as they have not transferred the full 10% of the mass in the first timestep (unlike schemes 1, 2 and 5). The relative energy changes of schemes 1-6 remain of the order 10^{-15} by $t = 1000$ s with schemes 5 and 6 having the smallest errors. Many of the non-conservative schemes produce large energy increases due to lack of internal energy conservation and unbounded velocities. Some of these schemes become unstable before the end of the test case at $t = 1000$ s. Note that two of the non-conservative schemes behave similarly to Schemes 1-6, but internal energy and momentum are not conserved exactly.

The smallest RMS error in potential temperature (at $t = 1000$ s) is obtained by scheme 4, followed by schemes 1 and 3. The RMS error of the fully-implicit scheme 6 is more than two orders of magnitude larger than that of scheme 4. However, the method 2 schemes (5 and 6) produce the smallest RMS error in vertical velocity, although the error from all method 1 schemes is within an order of magnitude. Averaging over both temperature and velocity field errors, scheme 2 is the most accurate.

3.3.2 Half-bubble test case

We have already shown solutions for transfers to an empty fluid. But how do the schemes behave when transferring between fluids with comparable mass and different properties? For this we use a 2-fluid test case from Weller and McIntyre (2019), where half the mass is initialised with the warm anomaly (fluid 1) and the other half without (fluid 0):

$$\sigma_1 = \begin{cases} 0.5 & \text{for } L < 1, \\ 0 & \text{otherwise,} \end{cases} \qquad \sigma_0 = 1 - \sigma_1. \tag{3.30}$$

The 2-fluid equations with different fluid properties require some form of stabilization (Weller and McIntyre, 2019; Thuburn et al., 2019). We will use a diffusive mass transfer to couple the fluids:

$$S_{ij} = \frac{1}{2}\frac{K_\sigma}{\eta_i}\max\left(0,\ \nabla^2(\eta_j - \eta_i)\right), \tag{3.31}$$

where $K_\sigma = 200$ m^2 s^{-1} is a large-enough diffusion coefficient to maintain numerical

stability for this test case (as shown in Weller and McIntyre, 2019).

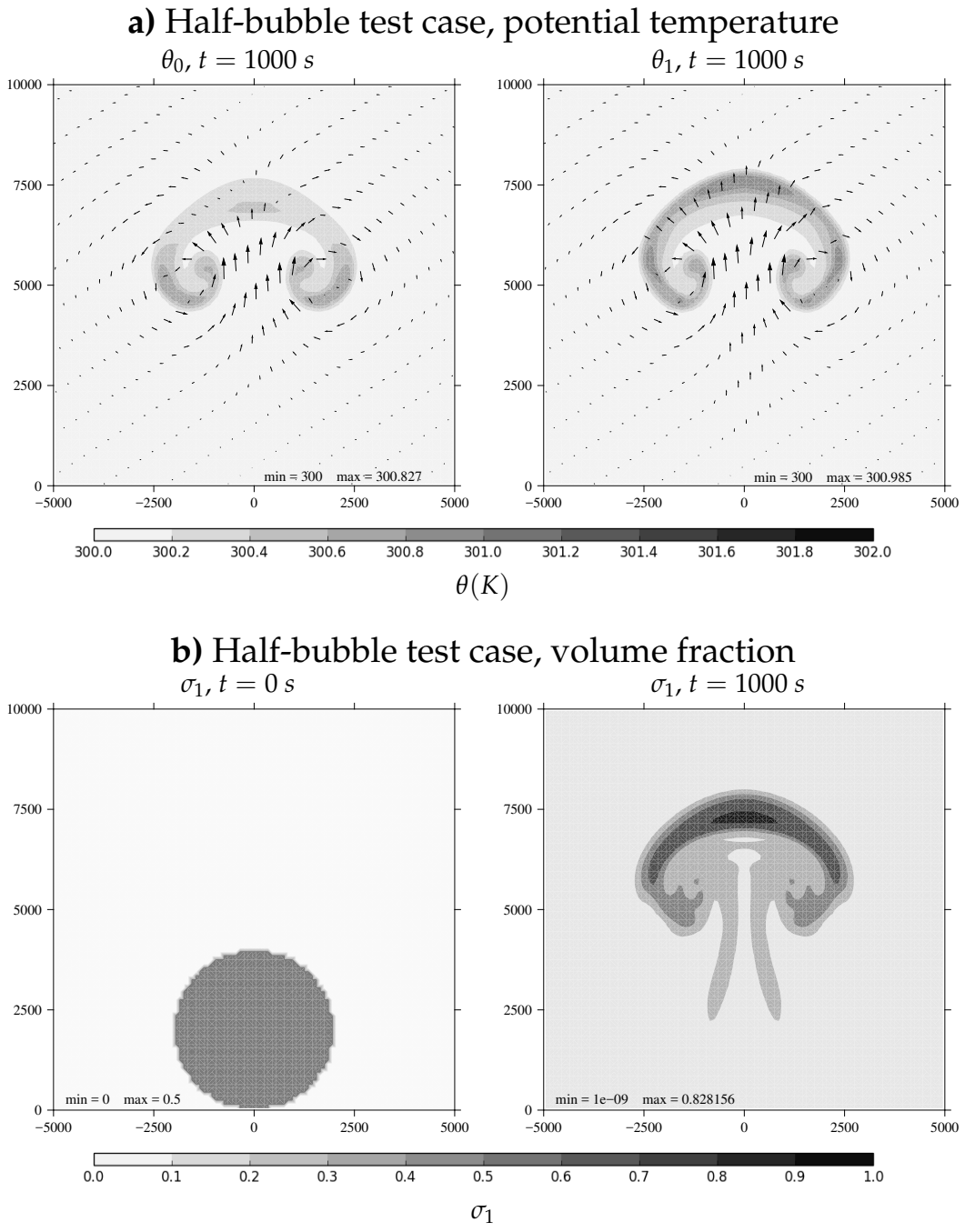

Figure 3.4: The temperature (a) and volume fraction (b) profiles of the half-bubble test case using scheme 2. The black arrows give the relative magnitudes and directions of the velocity vectors. As the warm anomaly is initially only in half the fluid, the distributions differ from the single-fluid case in figure 3.3, including a slower circulation over the domain.

The temperature and volume fraction distributions for this test case are shown in figure 3.4 - slower circulations form compared with the full bubble test case due to the lower mean temperature anomaly. The energy changes of all schemes relative

to the initial conditions are shown in figure 3.5. Dashed lines represent negative energy changes and solid lines show positive energy changes. Schemes 1-6 follow similar energy evolutions, where energy decreases relative to the initial conditions. The non-conservative schemes (light grey) exhibit various behaviours; many blow up within the first timesteps and produce large energy increases whereas some schemes (which use implicit transfers) follow similar energy evolutions to the conservative schemes. Note that energy changes due to other aspects of the numerical scheme (eg the non-energy-conserving van-Leer advection scheme) are far larger than changes due to the transfer schemes - hence all conservative schemes appear to behave similarly.

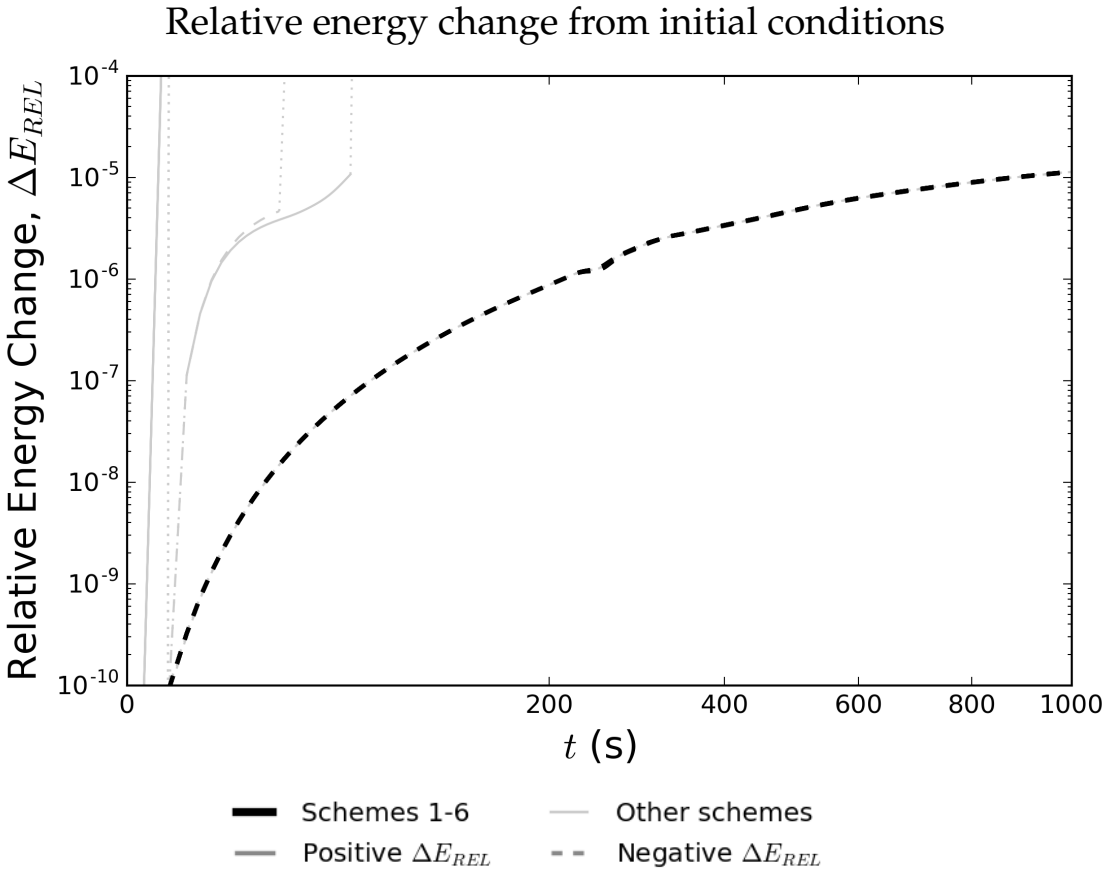

Figure 3.5: The relative energy change from the initial energy for all of the transfer schemes for the 2-fluid rising bubble test case. The solid and dashed lines represent positive and negative energy differences respectively. Dotted lines represent the transition between positive and negative energy changes. Schemes 1-6 are given by the black lines, while the remaining non-conservative schemes are given by the light grey lines.

These simulations on a staggered grid are consistent with the analysis of the transfer schemes in section 3.2 as schemes 1-6 conserve mass, momentum, internal energy and potential energy and are stable for the given test cases with no positive increases in total energy.

3.4 Conclusions

Transfer terms between the fluid components in the multi-fluid equations can be used to couple the fluids, represent physical exchanges and stabilise the equations, but the numerical treatment of the transfer terms must be stable. We have presented various numerical methods for treating the transfer terms between the fluids. These schemes are applicable to any multi-fluid equation set where the mean properties of a fluid are transferred with its mass. We have shown that some of the transfer schemes maintain positive mass, keep prognostic variables bounded, conserve momentum, potential & internal energy and are kinetic energy diminishing. These properties help to keep the overall numerical scheme accurate and stable on co-located and staggered grids.

Of the six conservative schemes, we have shown that scheme 3 can produce energy increases (figure 3.2). We have also shown that schemes 5 and 6 do not increase energy for $\Delta t S_{ij} \leq 1$ and $\Delta t S_{ij} > 0$ respectively. We have not proved this for schemes 1, 2 and 4 but have thoroughly explored the relevant parameter space for convection and have not found any instances of kinetic energy increases (other than scheme 1 for $\Delta t S_{ij} > 1$). The fully implicit schemes (schemes 4 and 6) automatically handle large mass transfers and scheme 6 also produces the smallest energy changes in the full bubble test case. The fully-implicit scheme 6 fulfils all of the aforementioned conservation requirements but produces the largest temperature inaccuracies in the full bubble test case. Our numerical analysis suggests that scheme 4 is an ideal transfer scheme and that scheme 2 is useful if the transfer is limited so that mass positivity is maintained. Both schemes also produced accurate temperature and velocity fields, meaning that they are the most suitable for representing entrainment and detrainment in the multi-fluid equations can be conducted in a numerically stable manner. The physical form of the entrainment and detrainment transfer terms for dry convection will be investigated in chapter 4.

Chapter 4

Building a two-fluid dry convection scheme for the grey zone

The results from sections 4.1 and 4.2 were used to inform the closures for the 2-fluid Boussinesq scheme in Weller et al. (2020). The rising bubble test case results from section 4.3 (compressible 2-fluid equations) were replicated for the incompressible two-fluid model in Weller et al. (2020).

The multi-fluid equations have been proposed for the modelling of grey zone convection due to their potential for representation of net mass transport by convection and non-equilibrium dynamics (Thuburn et al., 2018; Weller and McIntyre, 2019). Thuburn and Vallis (2018) derived conservation properties of the multi-fluid equations and found their normal modes. Thuburn et al. (2019) analysed their stability and presented a numerical method of a stabilised version of the equations for a single-column model. Weller and McIntyre (2019) presented a numerical method of the fully compressible multi-fluid Euler equations. In chapter 3, we presented stable and conservative numerical schemes for exchanges between the fluids (see also McIntyre et al., 2020). However, little has been done to represent grey zone convection with the multi-fluid equations. Moreover, we have a limited understanding of how entrainment and detrainment should be parameterised in the multi-fluid framework.

In this chapter we use the single fluid rising bubble test case from Bryan and Fritsch (2002) and attempt to reproduce it using a coarse 2-fluid scheme. In section 4.1, we use a fluid filter based on the vertical velocity to diagnose the expected properties of each fluid from the resolved single fluid test case, as well as the form of the entrainment and detrainment terms. In section 4.2, we present and analyse different methods for transferring the fluid temperatures which assume sub-filter-scale variability - unlike the schemes from chapter 3 which always transfer the mean potential temperature. We will also investigate which schemes most accurately reproduce the expected temperature fields in entraining and detraining regions. Finally, we will use our analyses from sections 4.1 and 4.2 to set up and test a two fluid scheme over a large range of resolutions (including the grey zone) in section 4.3.

4.1 Single-fluid rising bubble test case analysis

4.1.1 Test case and performance with resolution

We will use the same (full) single-fluid rising bubble test case for our "truth" solution as defined in chapter 3.3 (as well as Bryan and Fritsch, 2002), including the same numerical scheme. The solution for the potential temperature is shown in figure 3.3, with a horizontal resolution of 100 m (200 columns). However, horizontal resolutions in global models are typically far coarser at scales $\Delta x \sim 10$ km. But what happens to the rising bubble if the test case is run at these coarser resolutions? The horizontally averaged temperature profile of the single-fluid rising bubble test case is shown in figure 4.1 (200 columns), as well as the solutions using different horizontal resolutions. Figure 4.1 emphasises the issues with modelling coarse dry convection using a single-fluid dynamical core. The results show the inhibited ability of the warm perturbation to rise at lower resolutions, to the extent that there is no movement from the initial conditions in the single column case - this is because there are no neighbouring columns for horizontal convergence/divergence and only one vertical velocity vector per grid box, meaning the fluid cannot rise as any movement would create a vacuum-like effect where empty space cannot be filled due to continuity. Convection parameterisations are needed to transport heat vertically in this case. Using the two-fluid approach, movement will be allowed in the single-column case due to the presence of a second velocity field. This would allow for one fluid to rise as the other descends. As such, it is not fair to make comparisons with the single-column, single-fluid scheme without a convection parameterisation.

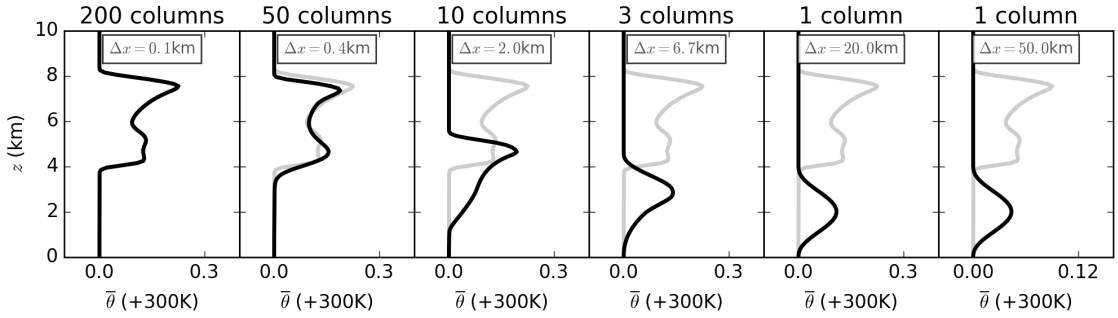

Figure 4.1: Horizontally-averaged temperature distributions for the single-fluid rising bubble test case at various resolutions (black). The grey lines show the horizontally averaged profile for the 200 column test case.

4.1.2 Diagnosing updraft and downdraft fluids

By horizontally averaging the well-resolved single-fluid rising bubble test case, we know what the mean temperatures/velocities should be after $t = 1000\ s$. But to help analyse a 2-fluid scheme, we must first define our fluid filter and then apply it to our single-fluid solution. We choose to label a grid cell according to its vertical velocity such that the fluid label is

$$I_1 = \begin{cases} 1 & \text{for } w > 0, \\ 0 & \text{for } w \leq 0, \end{cases} \tag{4.1}$$

and $I_0 = 1 - I_1$, where fluid 0 is defined as the downdraft fluid and fluid 1 as the updraft fluid. Alternative fluid filters also exist including Couvreux et al. (2010) and Efstathiou et al. (2019) who also use other variables in their filter such as liquid water content, height relative to cloud base and tracer concentrations. Changes in sign of vertical velocity will need to be modelled by the mass transfer terms, which will be investigated in section 4.1.4.

Figure 4.2 shows the vertical velocity field of the well-resolved single-fluid case at $t = 1000$ s which will be used to filter the field into two fluids. The dotted contour shows the boundary where the vertical velocity is zero which is the interface between the two fluids. From this we can see that the volume fraction for the updraft will be $\sigma_1 \sim 0.25$ when averaging over a 20 km wide column. This is somewhat consistent with studies which assume a uniform volume fraction for all heights (such as Siebesma et al., 2007).

We use the velocity filter to extract the horizontally-averaged (HA) volume fraction and mass quantities via conditional averaging:

$$\sigma_{\mathrm{HA},i} \equiv \frac{1}{x_2 - x_1} \int_{x_1}^{x_2} I_i dx, \tag{4.2}$$

$$\eta_{\mathrm{HA},i} \equiv \frac{1}{x_2 - x_1} \int_{x_1}^{x_2} I_i \rho \, dx, \tag{4.3}$$

where $x_1 = -10$ km and $x_2 = 10$ km. Other conditionally averaged mean variables are obtained via

$$\overline{\phi}_{\mathrm{HA},i} = \frac{1}{\eta_{\mathrm{HA},i}} \frac{1}{x_2 - x_1} \int_{-10km}^{10km} I_i \rho \phi_i \, dx, \tag{4.4}$$

and variances via

$$\phi'^{2}_{\mathrm{HA},i} = \frac{1}{\eta_{\mathrm{HA},i}} \frac{1}{x_2 - x_1} \int_{-10km}^{10km} I_i \rho (\phi_i - \overline{\phi}_{i,\mathrm{HA}})^2 \, dx. \tag{4.5}$$

Vertical profiles of these averages are presented in figure 4.3. When conducting coarse

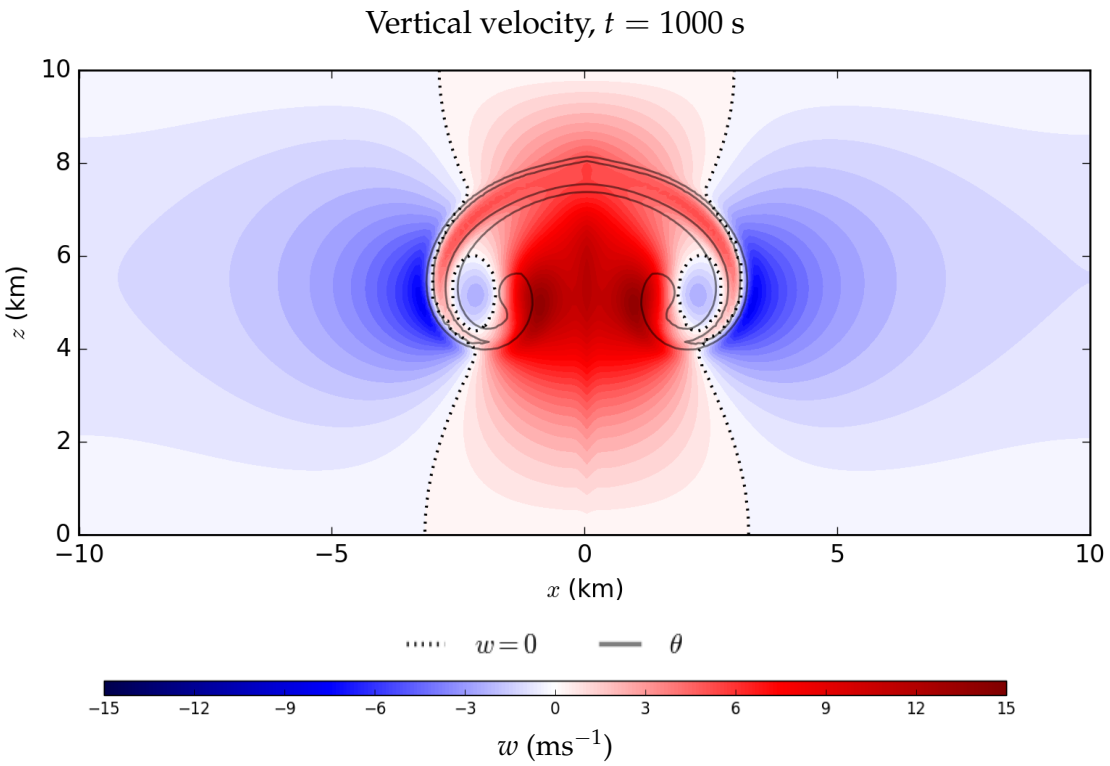

Figure 4.2: The well resolved vertical velocity field of the single-fluid rising bubble test case at $t = 1000$ s. Positive and negative vertical velocities are shown by red and blue regions respectively, where the dotted line shows the $w = 0$ m s^{-1} contour. The grey contour lines show the potential temperature field, contoured at 300.5 K and 301 K.

2-fluid simulations, it is these profiles which we aim to reproduce.

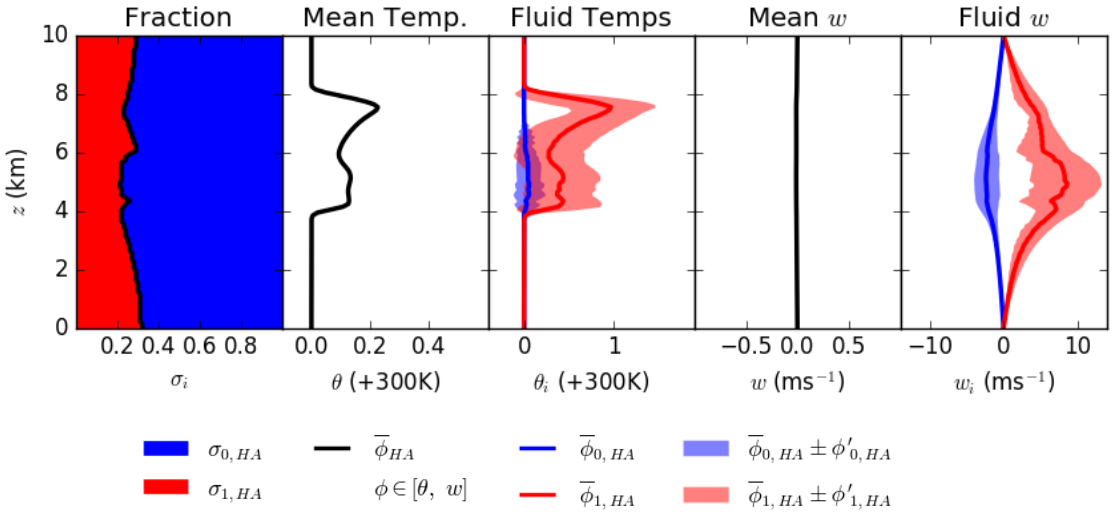

Figure 4.3: The horizontally averaged variables from the well-resolved, single-fluid rising bubble test case after 1000 s. Fluid 0 features are represented in blue and fluid 1 features in red. Solid lines show the mean quantities and the transparent shaded zones show the one-standard-deviation regions.

The horizontally averaged potential temperature profile has 2 sets of local maxima: one at $z \approx 7.5$ km where the hottest anomalies have been concentrated and another at $z \approx 5$ *km* where the large-scale circulations have caused *entrainment* of warm regions which were previously *detrained* (according to our fluid definitions). The latter set of peaks may be difficult to reproduce in single-column simulations as they require modelling of sub-grid-scale processes. Also shown are the horizontally averaged profiles of our filtered fluids: updrafts (red) and downdrafts (blue), with shaded regions representing the standard deviation range. The mean updraft fluid temperature is hotter than that of the downdraft fluid but there are various instances below $z = 7$ km where the sub-filter temperatures overlap, as indicated by the shaded regions. This is due to the large-scale circulations which bring hot air into the downdraft fluid and vica versa. The mean vertical velocity is zero and the individual fluid velocities have opposite signs due to our filter condition. Unlike the temperature distributions, the shaded regions for the velocity profiles do not overlap which is a consequence of our choice of fluid filter where $w = 0$ m s^{-1} is the fluid interface.

4.1.3 Analysis of the pressure field

Thuburn et al. (2019) demonstrated that the 2-fluid incompressible equations with a shared pressure gradient generate a Kelvin-Helmholtz-like instability. This is consistent with Weller and McIntyre (2019), who needed drag or mixing between fluids for stable simulations - but the fluids became too strongly coupled as a result. In chapter 2, we showed that a pressure perturbation term for each fluid (proportional to velocity convergence) significantly damped the unstable modes. In this section we compare this pressure perturbation term with high resolution data.

We can use the well-resolved single-fluid test case, in-combination with our choice of filter, to examine the pressure differences that exist. Figure 4.4 shows the pressure anomalies with respect to the horizontal mean ($\pi - \pi_{\mathrm{HA}}$) at $t = 500$ s. Differences in pressure between fluids clearly exist, most notably at $z \approx 3$ km and $z \approx 5$ *km*. These pressure anomalies are responsible for the horizontal divergence above the bubble and horizontal convergence below the bubble. It may therefore be reasonable to assume that there exists a pressure anomaly (π_i') such that $\pi_i' \propto \boldsymbol{\nabla}.\boldsymbol{u}_i$. By adding this term to the momentum equation, we get

$$\frac{\partial \boldsymbol{u}_i}{\partial t} + \boldsymbol{u}_i.\boldsymbol{\nabla}\boldsymbol{u}_i = -c_p\theta_i\boldsymbol{\nabla}(\pi + \pi_i') - 2\boldsymbol{\Omega} \times \boldsymbol{u}_i + \boldsymbol{g} + \sum_{j \neq i}\left[\frac{\eta_j}{\eta_i}S_{ji}(\boldsymbol{u}_j - \boldsymbol{u}_i) - \boldsymbol{D}_{ij}\right], \qquad (4.6)$$

where $\pi_i' = -\gamma\boldsymbol{\nabla}.\boldsymbol{u}_i$ and γ is a positive constant. This choice of stabilization is consistent

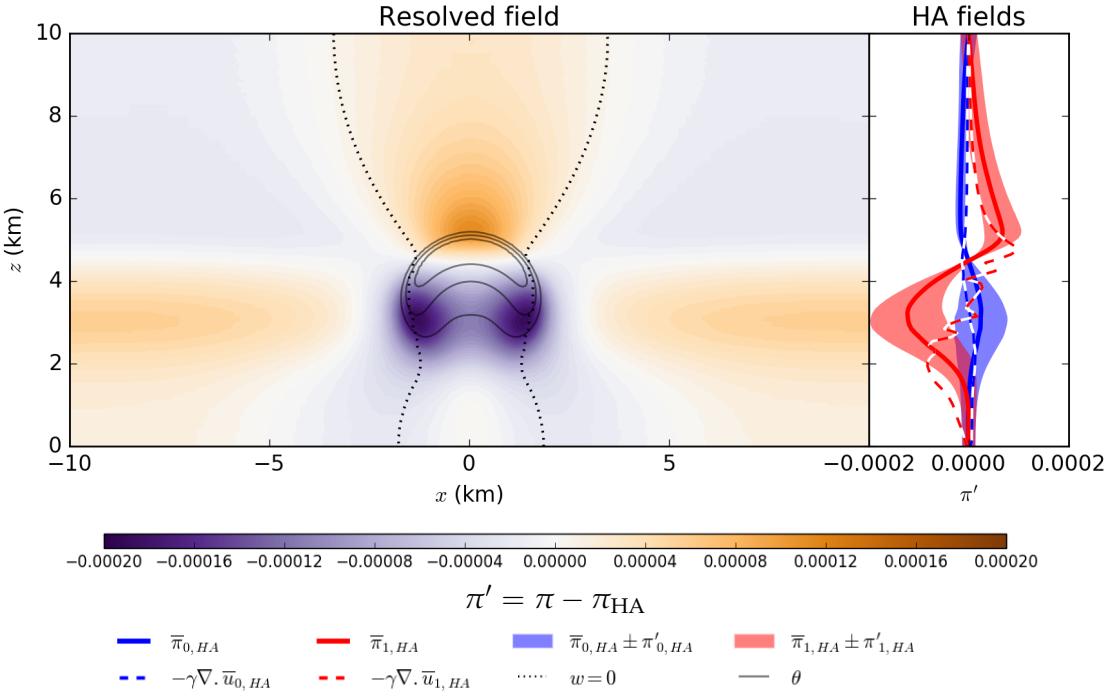

Figure 4.4: The anomalies of the Exner pressure relative the the horizontally averaged profile at $t = 500$ s. In the resolved profile (left), brown and purple regions indicate positive and negative pressure anomalies respectively. The grey contours show the potential temperature field, contoured at 300.5 K, 301 K and 301.5 K. The dotted line shows the $w = 0$ m s^{-1} interface. The horizontally-averaged fluid 0 pressure anomaly is given in blue, and fluid 1 in red (right). The dashed lines show the convergence of the horizontally averaged velocity field multiplied by $-\gamma$ where $\gamma = 0.02$ s.

with Thuburn et al. (2019), who demonstrate that a vertical velocity diffusion term is sufficient to suppress the Kelvin-Helmholtz-like instability present in the multi-fluid equations in a one column model. In a single column, both $\nabla^2 \boldsymbol{u}_i$ and $\boldsymbol{\nabla}(\boldsymbol{\nabla}.\boldsymbol{u}_i)$ reduce to $\frac{\partial^2 w_i}{\partial z^2}$. Note that, in well resolved systems $\boldsymbol{\nabla}(\boldsymbol{\nabla}.\boldsymbol{u}_i)$ becomes negligible whereas velocity diffusion does not. In order to use $\pi_i' = -\gamma \boldsymbol{\nabla}.\boldsymbol{u}_i$, we must use a sensible value for γ. Weller et al. (2020) conducted a scale analysis of the multi-fluid equations to diagnose γ. By assuming the circulation is driven by buoyancy, they found the relationship $\gamma c_p \theta_i \sim \sqrt{B} L^{\frac{3}{2}}$, where B is the magnitude of the buoyancy anomaly and L is the length scale of the anomaly. Using $B = g\frac{2\text{K}}{300\text{K}}$ m s^{-2} and the bubble radius $L = 2 \times 10^3$ m, we get $\gamma \sim 0.2$ s. Figure 4.4 shows the π_i' with $\gamma = 0.02$ s (dashed lines). The term shows good concordance with the filtered single-fluid pressure anomalies for $z > 5$ km and the correct sign below $z = 3$ km. It should be noted that the additional π_i' term breaks energy conservation when summed over all fluids, although the energy loss is not significant in short simulations like the rising bubble test case. Deriving a conservative pressure perturbation term will be a topic of future research. For the remainder of this chapter, we will use the $\pi_i' = -\gamma \boldsymbol{\nabla}.\boldsymbol{u}_i$ pressure perturbation term to stabilise the multi-fluid equations.

4.1.4 Diagnosing entrainment and detrainment

The horizontal differences in pressure between the fluids suggest that fluxes over the fluid boundaries exist; entrainment and detrainment in the form of mass transfers between fluids. Many different numerical transfer schemes for the multi-fluid equations have already been proposed in chapter 3. But we must also diagnose the expected transfer distribution for the rising bubble test case in order to accurately model convection in a coarse 2-fluid model.

For the resolved single fluid test case, the change in the mass field (per unit volume) over one timestep is given by

$$\frac{\eta^{n+1} - \eta^n}{\Delta t} + \left[\boldsymbol{\nabla}.(\eta \boldsymbol{u})\right]^n = 0, \tag{4.7}$$

meaning the new filtered horizontally averaged profile is

$$\begin{aligned} \eta^{n+1}_{HA,i} &= \left\{\eta^n - \Delta t \left[\boldsymbol{\nabla}.(\eta \boldsymbol{u})\right]^n\right\}_{HA,i} \\ &= \eta^n_{HA,i} - \Delta t \left[\boldsymbol{\nabla}.(\eta \boldsymbol{u})\right]^n_{HA,i}. \end{aligned} \tag{4.8}$$

The change in the fluid i mass for the single-column 2-fluid case is given by

$$\frac{\eta_i^{n+1} - \eta_i^n}{\Delta t} + \left[\boldsymbol{\nabla}.(\eta_i \boldsymbol{u}_i)\right]^n = \sum_{j \neq i} \left(S_{ji}\eta_j - S_{ij}\eta_i\right). \tag{4.9}$$

We want the single-column 2-fluid simulation to accurately represent the resolved single fluid test case. By equating η_i^{n+1} and $\eta^{n+1}_{HA,i}$, we can re-arrange to get an expression to diagnose what the mass transfer terms should be for consistency with the resolved simulation:

$$\Delta t \sum_{j \neq i} \left(S_{ji}\eta_j - S_{ij}\eta_i\right) = \eta^n_{HA,i} - \eta^n_i + \Delta t \left[\boldsymbol{\nabla}.(\eta_i \boldsymbol{u}_i)\right]^n - \Delta t \left[\boldsymbol{\nabla}.(\eta \boldsymbol{u})\right]^n_{HA,i}. \tag{4.10}$$

If we also initialise the 2-fluid simulation such that $\eta^n_i = \eta^n_{HA,i}$ then the transfer terms can be diagnosed through the difference in advection terms of the single-column 2-fluid and resolved single fluid simulations:

$$S_{01}\eta_0 - S_{10}\eta_1 = \left[\boldsymbol{\nabla}.(\eta_1 \boldsymbol{u}_1)\right]^n - \left[\boldsymbol{\nabla}.(\eta \boldsymbol{u})\right]^n_{HA,1}. \tag{4.11}$$

This will be used to diagnose the entrainment and detrainment terms. We will also

compare the diagnosed transfer to four possible models for mass transfer (MT):

- **MT1: Diffusion of σ_i**
  $\eta_i^m S_{ij} = \frac{1}{2} K_\sigma \max\left[0, \nabla^2(\eta_j^m - \eta_i^m)\right]$
  This mass transfer term was proposed in Weller and McIntyre (2019) for the multi-fluid equations. The transfer acts to smoothen and diffuse the volume fraction field. We will use $K_\sigma = 2 \times 10^3$ m^{2}s^{-1}.

- **MT2: Laplacian of θ_i**
  $\eta_0^m S_{01} = \frac{1}{2} \frac{K_\theta}{\theta_0} \max\left[0, -\nabla^2 \theta_0\right]$
  $\eta_1^m S_{10} = \frac{1}{2} \frac{K_\theta}{\theta_1} \max\left[0, \nabla^2 \theta_1\right]$
  This mass transfer term was also proposed in Weller and McIntyre (2019) for the multi-fluid equations. This term transfers regions of fluid 0 with positive temperature anomalies to fluid 1 and regions of negative temperature anomalies in fluid 1 to fluid 0. We will use $K_\theta = 5 \times 10^5$ m^{2}s^{-1}.

- **MT3: Velocity convergence**
  $\eta_i^m S_{ij} = \eta_i^m \max\left[0, -\boldsymbol{\nabla}.\boldsymbol{u}_i\right]$
  We noted in section 4.1.3 that pressure differences between the fluids exist. These pressure anomalies will cause horizontal convergence/divergence and therefore mass fluxes between the fluids. We therefore propose this transfer term which is proportional to the velocity convergence (ie. when a fluid "*bunches up*", the fluid is "*pushed*" into the neighbouring fluid). This is similar to the dynamical entrainment described in Houghton and Cramer (1951), and is equivalent to the transfer term used in chapter 2 and Weller et al. (2020).

- **MT4: Entrainment based on w_1 / R**
  $\eta_i^m S_{ij} = \eta_i^m \max\left[0, \frac{0.2 w_j}{R}\right]$
  This transfer is based on a commonly used term to model entrainment in mass flux schemes (De Rooy et al., 2013): entrainment, $\epsilon = \frac{0.2}{R}$. The transfer of fluid 0 to fluid 1 is proportional to the (positive) vertical velocity of fluid 1. We will use $R = 2$ km, the initial radius of of the bubble.

We will compare these mass transfers at various time steps using the same multi-fluid scheme described in chapter 3 and Weller and McIntyre (2019). For the 2-fluid test case we will use a single column which is 20 km wide, instead of the 200-column set-up used in the resolved single-fluid test case in figure 4.2. We initialise the 2-fluid 1-column scheme at a given time level n with the filtered, horizontally averaged profiles from the single-fluid resolved simulation. For example, if we initialised at $t = 1000$ s, the fields for each fluid would look like those in figure 4.3. We run the model for one timestep only ($\Delta t = 1$ s); we conduct the advection (to get us to time level m) and subsequently perform the mass transfers.

In appendix D, we note that using the fluid filter from equation 4.1 produces excessive noise in our mass transfer analysis due to the discrete switching of the vertical velocity sign between timesteps. We derive an approximation for the volume fraction when the $w = 0$ m s^{-1} fluid interface intersects a cell. This smoother filter will be used for analysis of the transfer terms in the remainder of section 4.1.4 as well as section 4.2.5.

Figure 4.5 shows the diagnosed mass transfer (left) and the behaviour of the four mass transfer types at $t = 100$ s (a), $t = 500$ s (b) and averaged over all timesteps (c). In figure 4.5.a, we diagnose that entrainment should occur for $z < 2$ km and detrainment for 2 km$< z < 4$ km - this is due to the upwards advection of fluid 1 in the two fluid scheme, which corresponds to $[\boldsymbol{\nabla}.(\eta_1 \boldsymbol{u}_1)]^n$ in equation 4.11. This mass transfer is well represented by the convergence-based mass transfer scheme (MT3). The diagnosed entrainment and detrainment above $z = 5$ km is due to the movement of the fluid interface in the resolved single fluid simulation ($\Delta t\,[\boldsymbol{\nabla}.(\eta \boldsymbol{u})]^n_{HA,i}$ in equation 4.11) - this is not well represented by any of the parameterisations.

At $t = 500$ s (figure 4.5.b), we diagnose entrainment to fluid 1 below the center of the warm anomaly ($z \approx 4$ km) and detrainment to fluid 0 above the warm anomaly - this is analogous to the horizontal convergence/divergence associated with the largest circulation seen in the resolved single-fluid test case. The velocity convergence transfer (MT3) is the only transfer term which captures this behaviour. This concordance is also present in the mass transfer profiles averaged over all timesteps (0 s$\leq t \leq$ 1000 s) in figure 4.5.c. The entrainment-based MT4 gives some resemblance below $z = 4$ km but continues to entrain air above this height. Both Laplacian-based transfers (MT1 and MT2) do not present any correlation with the diagnosed mass transfer.

It should be noted that the mass transfer types may perform better or worse for different test cases. Moreover, a different choice of fluid filter will significantly alter the form of the diagnosed mass transfer terms. As we have chosen to filter our fluid based on the vertical velocity, it makes sense to use a velocity-dependent mass transfer term. If we instead use a buoyancy-based filter, perhaps MT2 would prove more useful in transferring buoyant or negatively-buoyant regions between fluids.

Our results suggest that the divergence transfer term is realistic for a coarse two-fluid scheme when using a fluid filter based on vertical velocity. The transfer term successfully emulates the horizontal convergence/divergence which occurs in the resolved test case. Additional transfer terms may be needed to represent cloud base mass flux (where warm anomalies are moved into fluid 1). We will also need to analyse how the temperature and velocity fields evolve in a coarse 2-fluid simulation relative to the resolved case. If we can implement realistic transfer terms for the fluid

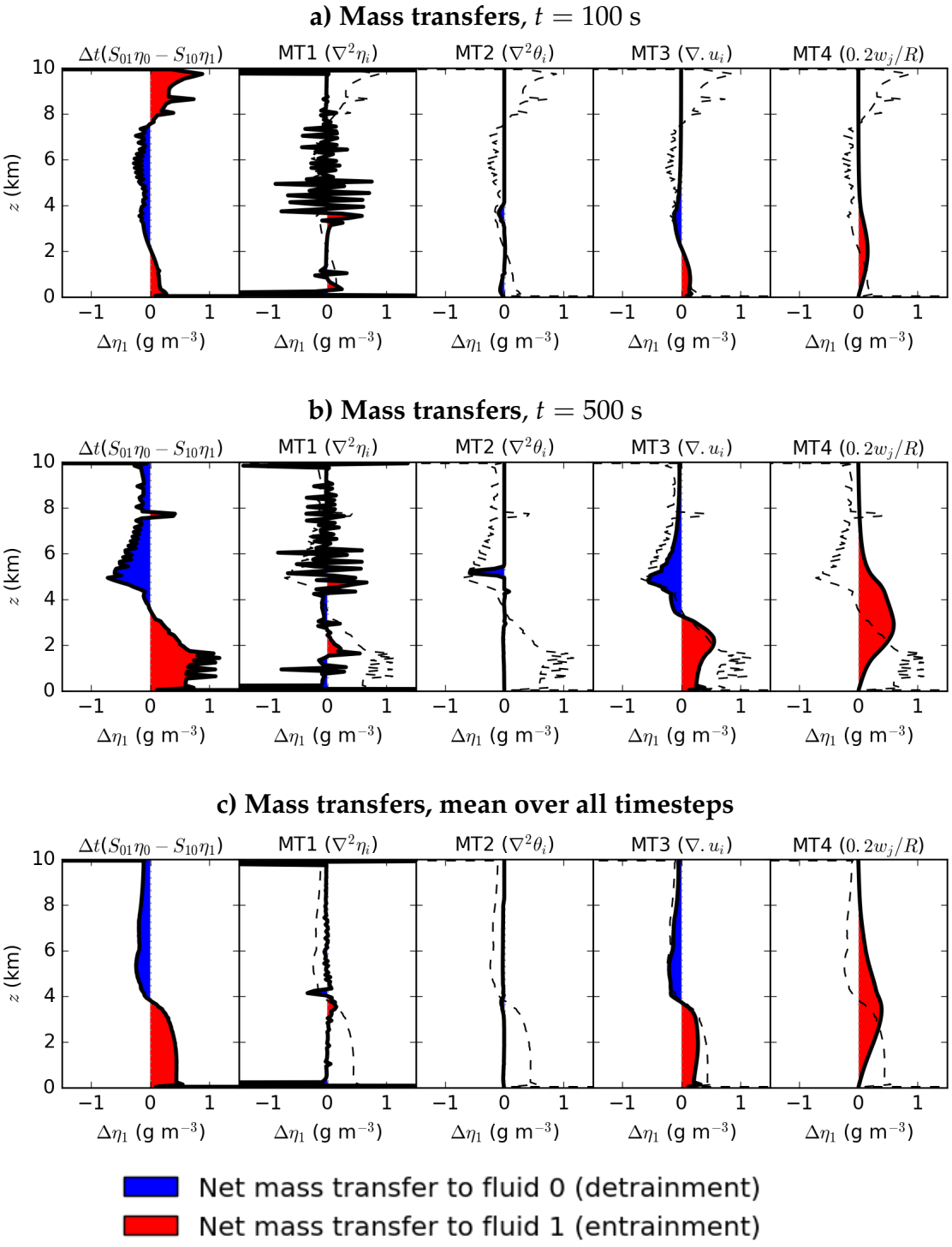

Figure 4.5: The mass transfers for fluid 1 produced by MT1-MT4 over one timestep ($\Delta t = 1$ s) at various times (right four columns). Also shown are the transfers needed to obtain the masses from the resolved filtered single-fluid test case (left). Gains in mass for fluids 0 and 1 are given by the blue and red regions respectively. Panel a shows the mass transfers at $t = 100$ s, panel b at 500 s and panel c shown the transfers averaged over 1000 timesteps.

properties (as well as the fluid mass), then an accurate 2-fluid scheme could be produced.

4.2 Derivation and analysis of transfer terms for the fluid properties

In chapter 3, we derived a set of numerical schemes which transfer the mean fluid properties when fluids are mixed. This assumes that the temperature or velocity distributions of the fluid transferred are delta functions, centred at the mean. But we have shown in figure 4.3 that various temperatures and velocities exist in a conditionally averaged fluid. This calls into question whether using mean transfers is a valid assumption. Fitch (2019) argues that using delta functions to represent the updraft and downdraft velocity probability density functions (PDFs) is not sufficient for an accurate convection scheme. This is because turbulent vertical velocity fluctuations are a significant process within clouds and the boundary layer as they are one of the main mechanisms for the vertical transport of heat, moisture and momentum in the atmosphere (Fitch, 2019). Knowledge of the temperature and velocity variance can also inform us of the intensity of the turbulence present within a cell as well as which regions of a PDF should be entrained or detrained. Various studies have demonstrated that information of subgrid-scale velocities is necessary for better cloud modelling (Lohmann et al., 1999; Donner et al., 2016; Fitch, 2019). Other studies have also used potential temperature PDFs (Mellor, 1977; Sommeria and Deardorff, 1977; Guo et al., 2015). However, it should be noted that any improvement in accuracy due to the representation of sub-grid (or sub-filter) variability should be judged relative to the increase in computational cost (Yano et al., 2018).

The combined grid-box velocity profile can be approximated via first-to-fourth order moments (mean, variance, skewness and kurtosis respectively) - although, even higher-order moments are required to exactly define the subgrid behaviour (Shohat and Tamarkin, 1943). An alternative to a fourth-order moment scheme is to assume two Gaussian distributions (one representing the turbulence properties of the updraft and one the properties of the downdraft) which can represent features such as skewness and kurtosis when the two profiles are summed together. This representation is especially applicable to convective clouds who's grid cell PDFs are strongly non-Gaussian, whereas stratocumulus clouds are Gaussian as there are no concentrated updraft regions (Fitch, 2019). We will therefore consider alternative transfer schemes to those in chapter 3 which assume sub-filter scale variability.

For a given fluid property ϕ, the budget equation when transferring non-mean fluid

properties in flux form is given by

$$\frac{\partial(\eta_i\overline{\phi}_i)}{\partial t} + \boldsymbol{\nabla}.\left(\overline{\phi}_i\boldsymbol{u}_i\right) = \eta_i F_i + \sum_{j\neq i}\left[\eta_j S_{ji}\overline{\phi}_{ji}^T - \eta_i S_{ij}\overline{\phi}_{ij}^T\right], \tag{4.12}$$

where F_i contains additional physics terms and $\overline{\phi}_{ij}^T$ is the transferred quantity. In advective form the equation becomes

$$\frac{\partial\overline{\phi}_i}{\partial t} + \boldsymbol{u}_i.\boldsymbol{\nabla}\overline{\phi}_i = F_i + \sum_{j\neq i}\left[S_{ji}\frac{\eta_j}{\eta_i}(\overline{\phi}_{ji}^T - \overline{\phi}_i) - S_{ij}(\overline{\phi}_{ij}^T - \overline{\phi}_i)\right]. \tag{4.13}$$

Note that the mean transfer equation from chapter 3 is recovered by using $\overline{\phi}_{ij}^T = \overline{\phi}_i$.

By using $\overline{\phi}_{ij}^T \neq \overline{\phi}_i$, we assume that there is some sub-filter scale variability in each fluid and that specific regions of the PDF are transferred. In our two fluid scheme, we will assume that the mass entrained or detrained from one fluid to another should carry the properties of the fluid interface. From our definition of 2-fluid scheme in 4.1, we know that the vertical velocity (w) is zero at the interface. By assuming that the horizontal velocities at the interface are equal to the mean fluid velocities, we get

$$\overline{\boldsymbol{u}}_{ij}^T = \begin{bmatrix}\overline{u}_i\\ \overline{v}_i\\ 0\end{bmatrix}, \tag{4.14}$$

where $\overline{u}_i$ and $\overline{v}_i$ are the mean velocities in the x and y directions respectively. We do not know the values of the potential temperature at the fluid interface so we must test and analyse different assumptions for the temperature at the fluid interface.

In this section we present and discuss four transfer methods for the potential temperature, three of which do not transfer the mean fluid properties and therefore assume sub-filter-scale variability within each fluid. Each method will use different transferred temperatures ($\overline{\theta}_{ij}^T$). We analyse which methods best reproduce the diagnosed velocity and temperature fields for the rising bubble test case.

4.2.1 TT1: Transferring the mean temperature of each fluid

Our first transfer type (TT) involves the transfer of the mean potential temperature of each fluid, where $\overline{\theta}_{ij}^T = \overline{\theta}_i$. This is the same transfer method used in chapter 3.

4.2.2 TT2: Transferring the total mean temperature over all fluids

In this transfer scheme we assume that the interface temperature is equal to the mean potential temperature over all fluid components:

$$\begin{aligned}\overline{\theta}_{ij}^{T} &= \overline{\theta}^{m} \\ &= \frac{\sum_i \eta_i^m \overline{\theta}_i^m}{\sum_i \eta_i^m}.\end{aligned} \tag{4.15}$$

The transferred temperature differs from Thuburn et al. (2019), who instead use a linear combination of fluid temperatures without mass weighting: $\overline{\theta}_{ij}^{T} = a\overline{\theta}_i + (1-a)\overline{\theta}_j$, where a is a constant. Without mass weighting, the temperature transferred will depend on the temperature of a fluid which may not always exist.

We will use a conservative numerical implementation of this scheme for TT1 and TT2 which follows Weller et al. (2020):

$$\begin{aligned}\begin{bmatrix}\overline{\theta}_0 \\ \overline{\theta}_1\end{bmatrix}^{n+1} &= \frac{1}{1+\Delta t S_{01}\frac{\eta_0^m}{\eta_1^m}+\Delta t S_{10}\frac{\eta_1^m}{\eta_0^m}} \\ &\times \begin{bmatrix}1+\Delta t S_{01}\frac{\eta_0^m}{\eta_1^m} & \Delta t S_{10}\frac{\eta_1^m}{\eta_0^m} \\ \Delta t S_{01}\frac{\eta_0^m}{\eta_1^m} & 1+\Delta t S_{10}\frac{\eta_1^m}{\eta_0^m}\end{bmatrix} \begin{bmatrix}(1+\Delta t S_{01})\overline{\theta}_0^m - \Delta t S_{01}\overline{\theta}_{01}^{T} + \Delta t S_{10}\frac{\eta_1^m}{\eta_0^m}(\overline{\theta}_{10}^{T} - \overline{\theta}_1^m) \\ (1+\Delta t S_{10})\overline{\theta}_1^m - \Delta t S_{10}\overline{\theta}_{10}^{T} + \Delta t S_{01}\frac{\eta_0^m}{\eta_1^m}(\overline{\theta}_{01}^{T} - \overline{\theta}_0^m).\end{bmatrix}\end{aligned} \tag{4.16}$$

Note that the numerical scheme reduces to scheme 2 from chapter 3 for the TT1 (mean) transfers.

4.2.3 TT3: Transfers using variance properties and Gaussian profiles

With TT2, we assumed sub-filter variability but did not define the potential temperature PDF. For this transfer scheme, we model the temperatures as Gaussian profiles, motivated by Fitch (2019) who demonstrate that the velocity field distributions for convection can be decomposed into a Gaussian for the updraft and a separate Gaussian for the surrounding environment (including the compensating downdraft). In this section, we derive transfer terms for the potential temperature based on these profiles, where the hottest regions of fluid 0 and coldest regions of fluid 1 are transferred.

Imagine we have a 2-fluid system with masses $\eta_i \equiv \sigma_i \rho_i$, mean temperatures $\overline{\theta}_i$ and temperature variances of $\theta_i'^2$. We assume the fluid temperatures are normally distributed

at some time level n by

$$\Theta_i^n \equiv N\left(\theta, \overline{\theta}_i^n, \theta_i'^n\right) = \frac{1}{\sqrt{2\pi}\theta_i'^n} \exp\left[-\frac{(\theta - \overline{\theta}_i^n)^2}{2(\theta_i'^2)^n}\right]. \tag{4.17}$$

$\eta_i^n \Theta_i^n$ is therefore the mass-weighted distribution which gives the fluid mass when integrated. We will once again perform our transfers from time-level m (after advection and other processes) in order to get to time-level $n+1$, like in chapter 3.

We expect that the updraft fluid should contain the highest temperatures in any given cell. Moreover, we expect some transition between the location of the most buoyant regions (in the updraft fluid) and the most negatively-buoyant regions (in the downdraft fluid). When transferring mass between the fluids, we therefore want the largest temperatures to be transferred out of the downdraft fluid and vice versa for the updraft fluid (see figure 4.6). We will therefore assume that the largest parts of the fluid 0 PDF and the smallest regions of the fluid 1 profile are more likely to be transferred.

The integral of a Gaussian with a mean $\overline{\theta}$ and variance θ'^2 is

$$\int_{-\infty}^{\infty} \frac{1}{\sqrt{2\pi}\theta'} \exp\left[-\frac{(\theta - \overline{\theta})^2}{2\theta'^2}\right] d\theta = \frac{1}{2}\left[1 + \mathrm{erf}\left(\frac{\theta - \overline{\theta}}{\sqrt{2}\theta'}\right)\right], \tag{4.18}$$

where erf is the error function. This function, which is 0 as $\theta \to -\infty$ and 1 as $\theta \to \infty$ (see figure 4.6), can be used to determine which regions of the fluid temperature PDF are transferred. Let us first consider the transfer of fluid 0 to fluid 1. To help diagnose which PDF regions to transfer, we define a reference profile $\Theta_{\mathrm{REF},01}$ where $\Theta_{\mathrm{REF},ij} = N\left(\theta, \overline{\theta}_{ij}^n, \theta_{ij}'^n\right)$ is a Gaussian, $\overline{\theta}_{ij}^n$ is the mean of the reference profile and $\theta_{ij}'^n$ is the standard deviation. By multiplying $\int_{-\infty}^{\infty} \Theta_{\mathrm{REF},01} d\theta$ by the fluid 0 profile, we get a continuous region to transfer from fluid 0 to 1 (shown in red, figure 4.6):

$$\eta_0^m \Theta_{01} = \eta_0^m \frac{1}{2}\left[1 + \mathrm{erf}\left(\frac{\theta - \overline{\theta}_{01}}{\sqrt{2}\theta_{01}'}\right)\right] \frac{1}{\sqrt{2\pi}\theta_0'} \exp\left[-\frac{(\theta - \overline{\theta}_0^m)^2}{2(\theta_0'^2)^m}\right]. \tag{4.19}$$

It follows that the fraction of the mass transferred (which is also equal to $\Delta t S_{ij}$) is given by the integral of Θ_{01}. Using appendix C.1 (where we integrate an error function times a

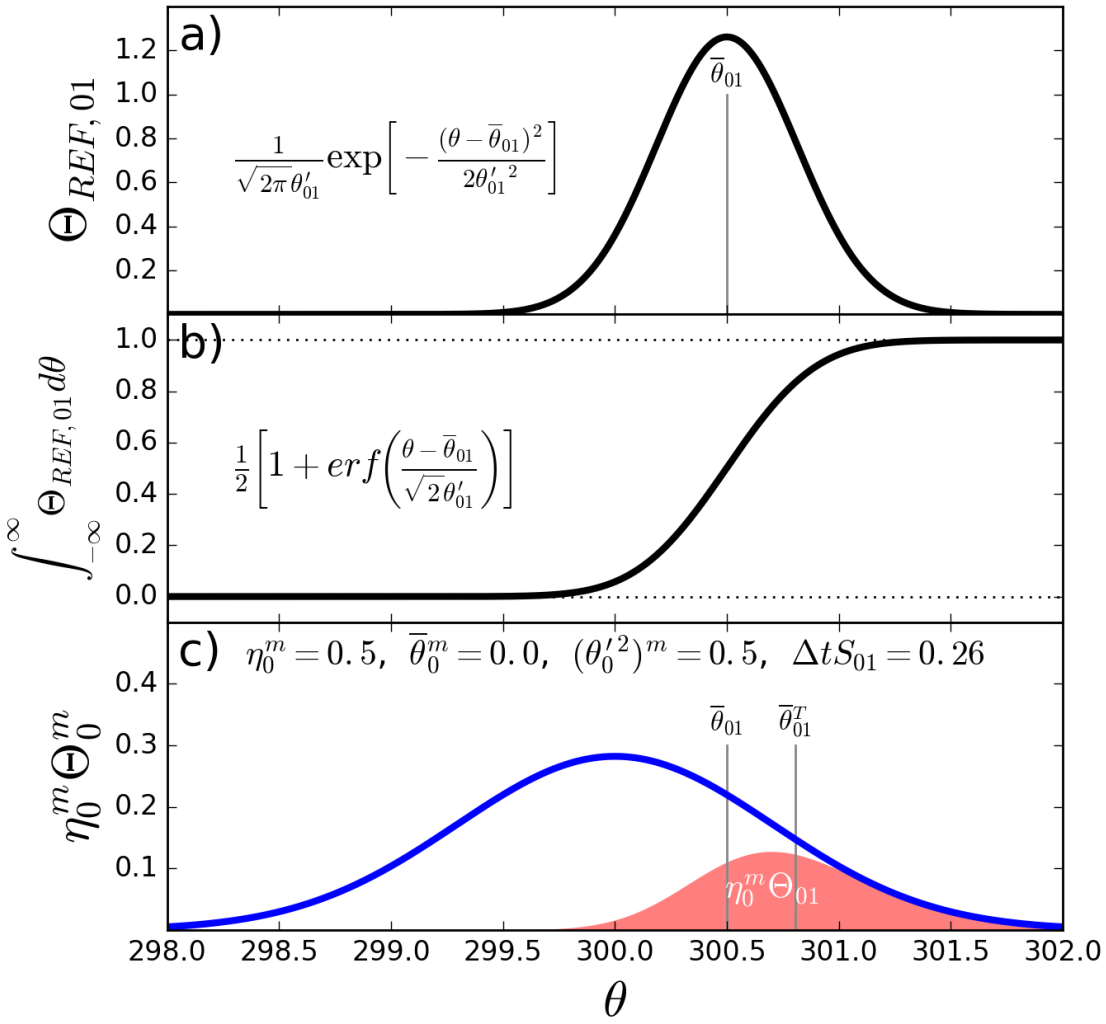

Figure 4.6: An arbitrary example of how the reference profile ($\Theta_{\text{REF},01}$) and transfer rate (S_{01}) are related. The reference profile (a) can be integrated (b) and multiplied by the fluid 0 blue profile Θ_0^m (c) to get the region to transfer to fluid 1 (red). $\overline{\theta}_{01}$ is the mean of the reference profile and $\overline{\theta}^T_{01}$ represents the mean value of the transferred region. Note that $\overline{\theta}^T_{01}$ is slightly to the right of the peak of the transferred region because Θ_{01} is not a Gaussian.

Gaussian), we get

$$\begin{aligned} \Delta t S_{01} &= \int_{-\infty}^{\infty} \Theta_{01}\, d\theta \\ &= \frac{1}{2}\left[1 + \text{erf}\left(\frac{\overline{\theta}_0^m - \overline{\theta}_{01}}{\sqrt{2}\sqrt{(\theta'^2_0)^m + (\theta'^2_{01})}}\right)\right]. \end{aligned} \tag{4.20}$$

The unknown variables are $\overline{\theta}_{01}$ and θ'^2_{01} as we have already defined S_{ij} in section 4.1.4. By assuming the transfer variance (θ'^2_{01}) is some predefined value, equation 4.20 can then

be rearranged to find $\overline{\theta}_{01}$:

$$\overline{\theta}_{01} = \overline{\theta}_0 - \sqrt{2}\sqrt{(\theta_0'^{\,2})^m + (\theta_{01}'^{\,2})}\ \mathrm{erf}^{-1}\left(2\Delta t\ S_{01} - 1\right). \tag{4.21}$$

When transferring from fluid 1 to fluid 0, we want to remove the lowest temperatures so we instead get:

$$\begin{aligned}
\Delta t S_{10} &= \int_{-\infty}^{\infty} \Theta_{10}\, d\theta \\
&= \int_{-\infty}^{\infty} \frac{1}{2}\left[1 - \mathrm{erf}\left(\frac{\theta - \overline{\theta}_{10}}{\sqrt{2}\theta_{10}'}\right)\right] \frac{1}{\sqrt{2\pi}\theta_1'} \exp\left[-\frac{(\theta - \overline{\theta}_1^m)^2}{2(\theta_1'^{\,2})^m}\right] d\theta \\
&= \frac{1}{2}\left[1 - \mathrm{erf}\left(\frac{\overline{\theta}_1^m - \overline{\theta}_{10}}{\sqrt{2}\sqrt{(\theta_1'^{\,2})^m + (\theta_{10}'^{\,2})}}\right)\right], \\
\implies \overline{\theta}_{10} &= \overline{\theta}_1 + \sqrt{2}\sqrt{(\theta_1'^{\,2})^m + (\theta_{10}'^{\,2})}\ \mathrm{erf}^{-1}\left(2\Delta t\ S_{10} - 1\right).
\end{aligned} \tag{4.22}$$

Figure 4.7 shows the transfer region of fluid 1 to fluid 0 (blue-shaded region) for an arbitrarily-chosen transfer rate of $\Delta t S_{10} = 0.2$.

The new mean temperature of fluid 0 is given by the first order moment of the new fluid 0 profile:

$$\begin{aligned}
\eta_0^{n+1}\overline{\theta}_0^{n+1} &= \eta_0^m \underbrace{\int_{-\infty}^{\infty} \theta\Theta_0^m d\theta}_{\text{Original mean}} - \eta_0^m \underbrace{\int_{-\infty}^{\infty} \theta\Theta_{01}^m d\theta}_{\text{Red region mean (fig. 4.7)}} + \eta_1^m \underbrace{\int_{-\infty}^{\infty} \theta\Theta_{10}^m d\theta}_{\text{Blue region mean}} \\
&= \eta_0^m\overline{\theta}_0^m - \Delta t\ S_{01}\ \eta_0^m\overline{\theta}_{01}^T + \Delta t\ S_{10}\ \eta_1^m\overline{\theta}_{10}^T.
\end{aligned} \tag{4.23}$$

For fluid 1, we get:

$$\eta_1^{n+1}\overline{\theta}_1^{n+1} = \eta_1^m\overline{\theta}_1^m + \Delta t\ S_{01}\ \eta_0^m\overline{\theta}_{01}^T - \Delta t\ S_{10}\ \eta_1^m\overline{\theta}_{10}^T. \tag{4.24}$$

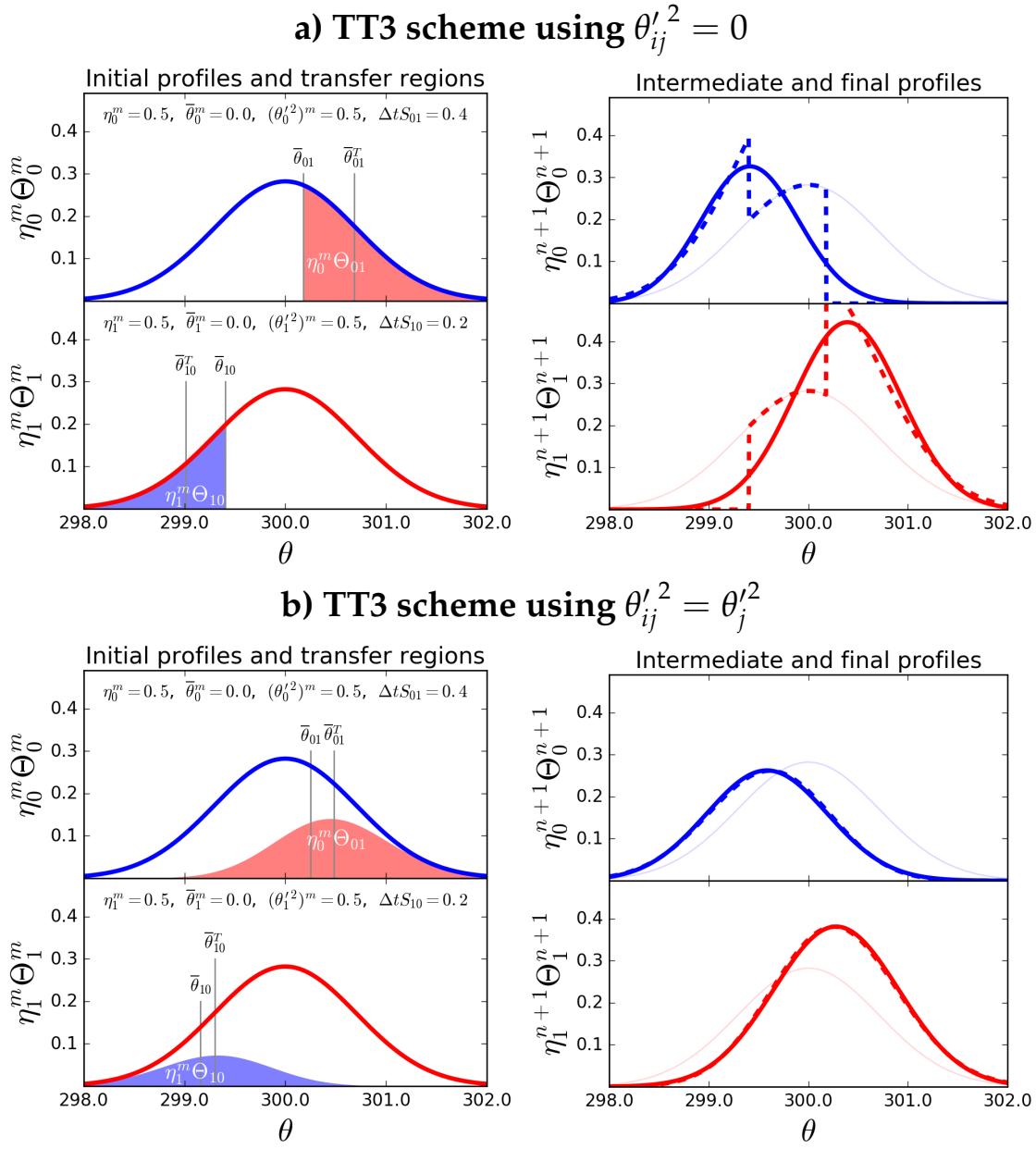

Figure 4.7: The profiles of 2 fluids which initially have identical mean and variance values (left). By arbitrarily prescribing $\Delta tS_{01} = 0.4$ and $\Delta tS_{10} = 0.2$, we get the intermediate profiles (dashed) and the new Gaussian profiles (solid) on the right-hand-side panels. By using $\theta'^2_{ij} = 0$ (a), the largest fluid 0 regions and the smallest fluid 1 regions are transferred. Using $\theta'^2_{ij} = \theta'^2_j$ (b) produces far smoother intermediate profiles and makes the Gaussian assumption for timestep $n+1$ more accurate.

$\bar{\theta}_{01}^T$ and $\bar{\theta}_{10}^T$ are the mean values of the transfer regions such that,

$$\begin{aligned}
\bar{\theta}_{01}^T &= \frac{1}{\Delta tS_{01}} \int_{-\infty}^{\infty} \theta\Theta_{01} d\theta \\
&= \frac{1}{\Delta tS_{01}} \left\{ \frac{1}{2}\bar{\theta}_0^m \left[1 + \operatorname{erf}\left(\frac{\bar{\theta}_0^m - \bar{\theta}_{01}}{\sqrt{2}\sqrt{(\theta_0'^2)^m + (\theta_{01}'^2)^m}} \right) \right] \right. \\
&\quad \left. + \bar{\theta}_0 \frac{1}{\sqrt{2\pi}\sqrt{(\theta_0'^2)^m + (\theta_{01}'^2)^m}} \exp\left[\frac{1}{2} \frac{(\bar{\theta}_0^m - \bar{\theta}_{01})^2}{(\theta_0'^2)^m + (\theta_{01}'^2)^m} \right] \right\}, \\
\implies \bar{\theta}_{01}^T &= \bar{\theta}_0^m + \frac{(\theta_0'^2)^m}{\Delta tS_{01}} N\left(\bar{\theta}_{01}, \bar{\theta}_0, \sqrt{(\theta_0'^2)^m + (\theta_{01}'^2)^m} \right),
\end{aligned} \tag{4.25}$$

and

$$\overline{\theta}_{10}^{T} = \overline{\theta}_{1}^{m} - \frac{(\theta_1'^{2})^m}{\Delta t S_{10}} N\left(\overline{\theta}_{10}, \overline{\theta}_{1}, \sqrt{(\theta_1'^{2})^m + (\theta_{10}'^{2})^m}\right), \tag{4.26}$$

which were derived using appendices C.2 and C.4. Figure 4.6 illustrates the locations of $\overline{\theta}_{ij}^{T}$ for a given example where $\Delta t S_{01} = 0.26$, and figure 4.7 shows $\overline{\theta}_{ij}^{T}$ for different transfer rates. Given that $\theta'^{2} N$ is positive, fluid 0 will transfer a temperature larger than (or equal to) its own mean which will cool fluid 0. The opposite is true for fluid 1. Also note that the total internal energy will clearly be conserved as $\eta_0^{n+1}\overline{\theta}_0^{n+1} + \eta_1^{n+1}\overline{\theta}_1^{n+1} = \eta_0^{m}\overline{\theta}_0^{m} + \eta_1^{m}\overline{\theta}_1^{m}$.

In order to calculate the Gaussian profiles at time level $n+1$, we must also calculate the new values of the fluid variances. For convenience, we define $\zeta_i^m = \left[(\theta_i'^{2})^m + (\overline{\theta}_i^m)^2\right]$. With the help of appendices C.1, C.2, C.3 and C.5, we calculate ζ_i^{n+1} using:

$$\begin{aligned}\eta_0^{n+1}\zeta_0^{n+1} &= \eta_0^m \int_{-\infty}^{\infty} \theta^2 \Theta_0^m d\theta - \eta_0^m \int_{-\infty}^{\infty} \theta^2 \Theta_{01}^m d\theta + \eta_1^m \int_{-\infty}^{\infty} \theta^2 \Theta_{10}^m d\theta \\ &= \eta_0^m \zeta_0^m - \Delta t\ S_{01}\ \eta_0^m \zeta_{01}^T + \Delta t\ S_{10}\ \eta_1^m \zeta_{10}^T,\end{aligned} \tag{4.27}$$

and

$$\eta_1^{n+1}\zeta_1^{n+1} = \eta_1^m \zeta_1^m + \Delta t\ S_{01}\ \eta_0^m \zeta_{01}^T - \Delta t\ S_{10}\ \eta_1^m \zeta_{10}^T, \tag{4.28}$$

where

$$\begin{aligned}\zeta_{01}^T &= \frac{1}{\Delta t S_{01}} \int_{-\infty}^{\infty} \theta^2 \Theta_{01}^m d\theta \\ &= \frac{1}{\Delta t S_{01}} \left\{ \frac{1}{2}\overline{\zeta}_0^m \left[1 + \operatorname{erf}\left(\frac{\overline{\theta}_0^m - \theta_{01}}{\sqrt{2}\sqrt{(\theta_0'^{2})^m + (\theta_{01}'^{2})^m}}\right)\right] \right. \\ &\quad \left. + \theta_0'^{m} \left[2\overline{\theta}_0^m - (\overline{\theta}_0^m - \overline{\theta}_{01}) \frac{(\theta_0'^{2})^m}{(\theta_0'^{2})^m + \theta_{01}'^{2}}\right] \frac{1}{\sqrt{2\pi}} \exp\left[-\frac{1}{2}\frac{(\overline{\theta}_0^m - \overline{\theta}_{01})^2}{(\theta_0'^{2})^m + (\theta_{01}'^{2})^m}\right] \right\} \\ &= \zeta_0^m + \frac{(\theta_0'^{2})^m}{\Delta t S_{01}} \left[2\overline{\theta}_0^m - (\overline{\theta}_0^m - \overline{\theta}_{01}) \frac{(\theta_0'^{2})^m}{(\theta_0'^{2})^m + \theta_{01}'^{2}}\right] N\left(\overline{\theta}_{01}, \overline{\theta}_0, \sqrt{(\theta_0'^{2})^m + (\theta_{01}'^{2})^m}\right),\end{aligned} \tag{4.29}$$

and

$$\begin{aligned}
\zeta_{10}^{T} &= \frac{1}{\Delta t S_{10}} \int_{-\infty}^{\infty} \theta^2 \Theta_{10}^{m} d\theta \\
&= \frac{1}{\Delta t S_{10}} \left\{ \frac{1}{2} \overline{\zeta}_1^{m} \left[1 - \operatorname{erf} \left(\frac{\overline{\theta}_1^{m} - \theta_{10}}{\sqrt{2}\sqrt{(\theta'^{2}_{10})^{m} + (\theta'^{2}_{1})^{m}}} \right) \right] \right. \\
&\left. - \theta'^{m}_{1} \left[2\overline{\theta}_1^{m} - (\overline{\theta}_1^{m} - \overline{\theta}_{10}) \frac{(\theta'^{2}_{1})^{m}}{\theta'^{2}_{10} + (\theta'^{2}_{1})^{m}} \right] \frac{1}{\sqrt{2\pi}} \exp \left[-\frac{1}{2} \frac{(\overline{\theta}_0^{m} - \overline{\theta}_{01})^2}{(\theta'^{2}_{10})^{m} + (\theta'^{2}_{1})^{m}} \right] \right\} \\
&= \zeta_1^{m} - \frac{(\theta'^{2}_{1})^{m}}{\Delta t S_{10}} \left[2\overline{\theta}_1^{m} - (\overline{\theta}_1^{m} - \overline{\theta}_{10}) \frac{(\theta'^{2}_{1})^{m}}{\theta'^{2}_{10} + (\theta'^{2}_{1})^{m}} \right] N \left(\overline{\theta}_{10}, \overline{\theta}_1, \sqrt{(\theta'^{2}_{10})^{m} + (\theta'^{2}_{1})^{m}} \right).
\end{aligned} \tag{4.30}$$

We then calculate the new fluid variance $(\theta_i'^2)^{n+1}$ using $\zeta_i^{n+1} - \left(\overline{\theta}_i^{n+1}\right)^2$. Note that the signs of the variance correction terms appear to suggest that the fluid 1 variance will tend to increase whilst the fluid 0 variance decreases. However, given that $\left(\theta_i'^2\right)^{n+1} = \zeta_i^{n+1} - (\overline{\theta}_i^{n+1})^2$ and that $\overline{\theta}_1^{n+1} - \overline{\theta}_1^{m} \geq \overline{\theta}_0^{n+1} - \overline{\theta}_0^{m}$, this effect is directly cancelled out resulting in equal treatment of the fluid variances - i.e. if the fluid variances are initially equal and if $S_{01} = S_{10}$, then they will be identical after the transfer has taken place.

We are now ready to use the TT3 scheme but we have not yet chosen a value for the reference profile variance, θ'^{2}_{ij}. We propose the following two choices:

- $\theta'^{2}_{ij} = 0$
  With zero variance, the reference profile ($\Theta_{\mathrm{REF},ij}$) becomes a delta function and the integral becomes a step function. This means that *all* of the largest fluid 0 temperatures are transferred for a given S_{ij} and *all* of the smallest fluid 1 temperatures (see figure 4.7.a). But this also means that the intermediate profiles are not continuous meaning the Gaussian assumption for time level $n+1$ is questionable. This gives us:

$$\begin{aligned}
\overline{\theta}_{01}^{T} &= \overline{\theta}_0^{m} + \frac{(\theta'^{2}_{0})^{m}}{\Delta t S_{01}} N \left(\overline{\theta}_{01}, \overline{\theta}_0, \theta'^{m}_{0} \right), \\
\overline{\theta}_{10}^{T} &= \overline{\theta}_1^{m} - \frac{(\theta'^{2}_{1})^{m}}{\Delta t S_{10}} N \left(\overline{\theta}_{10}, \overline{\theta}_1, \theta'^{m}_{1} \right), \\
\zeta_{01}^{T} &= \zeta_0^{m} + \frac{(\theta'^{2}_{0})^{m}}{\Delta t S_{01}} \left(\overline{\theta}_0^{m} + \overline{\theta}_{01} \right) N \left(\overline{\theta}_{01}, \overline{\theta}_0, \theta'^{m}_{0} \right), \\
\zeta_{10}^{T} &= \zeta_1^{m} - \frac{(\theta'^{2}_{1})^{m}}{\Delta t S_{10}} \left(\overline{\theta}_1^{m} + \overline{\theta}_{10} \right) N \left(\overline{\theta}_{10}, \overline{\theta}_1, \theta'^{m}_{1} \right).
\end{aligned} \tag{4.31}$$

- ${\theta'_{ij}}^2 = {\theta'_j}^2$
  With a finite variance, the largest fluid 0 temperatures are *more likely* to be transferred to fluid 1 and vice versa for the transfer from fluid 1 to 0. The resulting intermediate profiles are continuous (see figure 4.7.b). This gives us:

$$
\begin{aligned}
\overline{\theta}_{01}^T &= \overline{\theta}_0^m + \frac{({\theta'_0}^2)^m}{\Delta t S_{01}} N\left(\overline{\theta}_{01}, \overline{\theta}_0, \sqrt{({\theta'_0}^2)^m + ({\theta'_1}^2)^m}\right), \\
\overline{\theta}_{10}^T &= \overline{\theta}_1^m - \frac{({\theta'_1}^2)^m}{\Delta t S_{10}} N\left(\overline{\theta}_{10}, \overline{\theta}_1, \sqrt{({\theta'_0}^2)^m + ({\theta'_1}^2)^m}\right), \\
\zeta_{01}^T &= \zeta_0^m + \frac{({\theta'_0}^2)^m}{\Delta t S_{01}} \left[2\overline{\theta}_0^m - (\overline{\theta}_0^m - \overline{\theta}_{01}) \frac{({\theta'_0}^2)^m}{({\theta'_0}^2)^m + ({\theta'_1}^2)^m}\right] N\left(\overline{\theta}_{01}, \overline{\theta}_0, \sqrt{({\theta'_0}^2)^m + ({\theta'_1}^2)^m}\right), \\
\zeta_{10}^T &= \zeta_1^m - \frac{({\theta'_1}^2)^m}{\Delta t S_{10}} \left[2\overline{\theta}_1^m - (\overline{\theta}_1^m - \overline{\theta}_{10}) \frac{({\theta'_1}^2)^m}{({\theta'_0}^2)^m + ({\theta'_1}^2)^m}\right] N\left(\overline{\theta}_{10}, \overline{\theta}_1, \sqrt{({\theta'_0}^2)^m + ({\theta'_1}^2)^m}\right).
\end{aligned}
\tag{4.32}
$$

We will compare the performance of these methods in sections 4.2.4, 4.2.5 and 4.3.

4.2.4 Summary of potential temperature transfer types

Without advection or other processes, the transfers for the potential temperature in a two fluid system (i and j) are

$$
\frac{\partial \overline{\theta}_i}{\partial t} = S_{ji} \frac{\eta_j}{\eta_i} (\overline{\theta}_{ji}^T - \overline{\theta}_i) - S_{ij} (\overline{\theta}_{ij}^T - \overline{\theta}_i). \tag{4.33}
$$

We have discussed four different forms of the transferred potential temperature $\overline{\theta}_{ij}^T$:

- **Scheme TT1:** Transfer the mean temperature of the fluid:
  $\overline{\theta}_{ij}^T = \overline{\theta}_i$,

- **Scheme TT2:** Transfer the temperature at the fluid interface:
  $\overline{\theta}_{ij}^T = \left(\eta_i^m \theta_i^m + \eta_j^m \theta_j^m\right) / \left(\eta_i^m + \eta_j^m\right)$,

- **Scheme TT3 (with ${\theta'_{ij}}^2 = 0$):** Assume Guassian potential temperature PDFs. Transfer the hottest temperatures from fluid 0 and the coolest temperatures and velocities from fluid 1:
  $\overline{\theta}_{01}^T = \overline{\theta}_0^m + \frac{({\theta'_0}^2)^m}{\Delta t S_{01}} N\left(\overline{\theta}_{01}, \overline{\theta}_0, {\theta'_0}^m\right)$,
  $\overline{\theta}_{10}^T = \overline{\theta}_1^m - \frac{({\theta'_1}^2)^m}{\Delta t S_{10}} N\left(\overline{\theta}_{10}, \overline{\theta}_1, {\theta'_1}^m\right)$.

- **Scheme TT3 (with $\theta_{ij}'^2 = \theta_j'^2$):** Assume Guassian potential temperature PDFs. Transfer the hottest temperatures from fluid 0 with higher probability and vice versa for fluid 1:
$\overline{\theta}_{01}^T = \overline{\theta}_0^m + \frac{(\theta_0'^2)^m}{\Delta t S_{01}} N\left(\overline{\theta}_{01}, \overline{\theta}_0, \sqrt{(\theta_0'^2)^m + (\theta_1'^2)^m}\right)$,
$\overline{\theta}_{10}^T = \overline{\theta}_1^m - \frac{(\theta_1'^2)^m}{\Delta t S_{10}} N\left(\overline{\theta}_{10}, \overline{\theta}_1, \sqrt{(\theta_0'^2)^m + (\theta_1'^2)^m}\right)$.

Figure 4.8 shows how the mean temperatures evolve for the four transfer methods in two test cases where advection and other processes are not present. In figure 4.8.a, fluid 0 is initialised with a larger temperature than fluid 1 (both with close-to-zero variance). The transfer rate in both directions is $S_{ij} = 0.1$ s^{-1} with a timestep of $\Delta t = 1$ s. By transferring the mean fluid temperatures, the TT1 scheme (solid lines) converges to the mean temperature of the system - this is undesirable in a 2-fluid system as the fluid properties should be different. The TT2 scheme (dashed lines) transfers the mean temperature of the system ($\overline{\theta} = 301$ K) which means that the fluids are transferring the same properties to each other. As there is an equal mass exchange between the two fluids, the temperatures remain the same. Only the TT3 schemes (dot-dashed and dotted lines) successfully swap the the fluid properties so that fluid 1 is hotter than fluid 0. The $\theta_{ij}'^2 = 0$ method converges the fastest of the two TT3 schemes.

Figure 4.8.b shows a test case where the temperature of both fluids is initially zero, but the temperature variance is non-zero. The TT1 ($\overline{\theta}_{ij}^T = \overline{\theta}_i$) and TT2 ($\overline{\theta}_{ij}^T = \overline{\theta}$) transfer schemes do not alter the fluid properties. Both TT3 schemes are able to transfer hot temperatures to fluid 1 and cold temperatures to fluid 0.

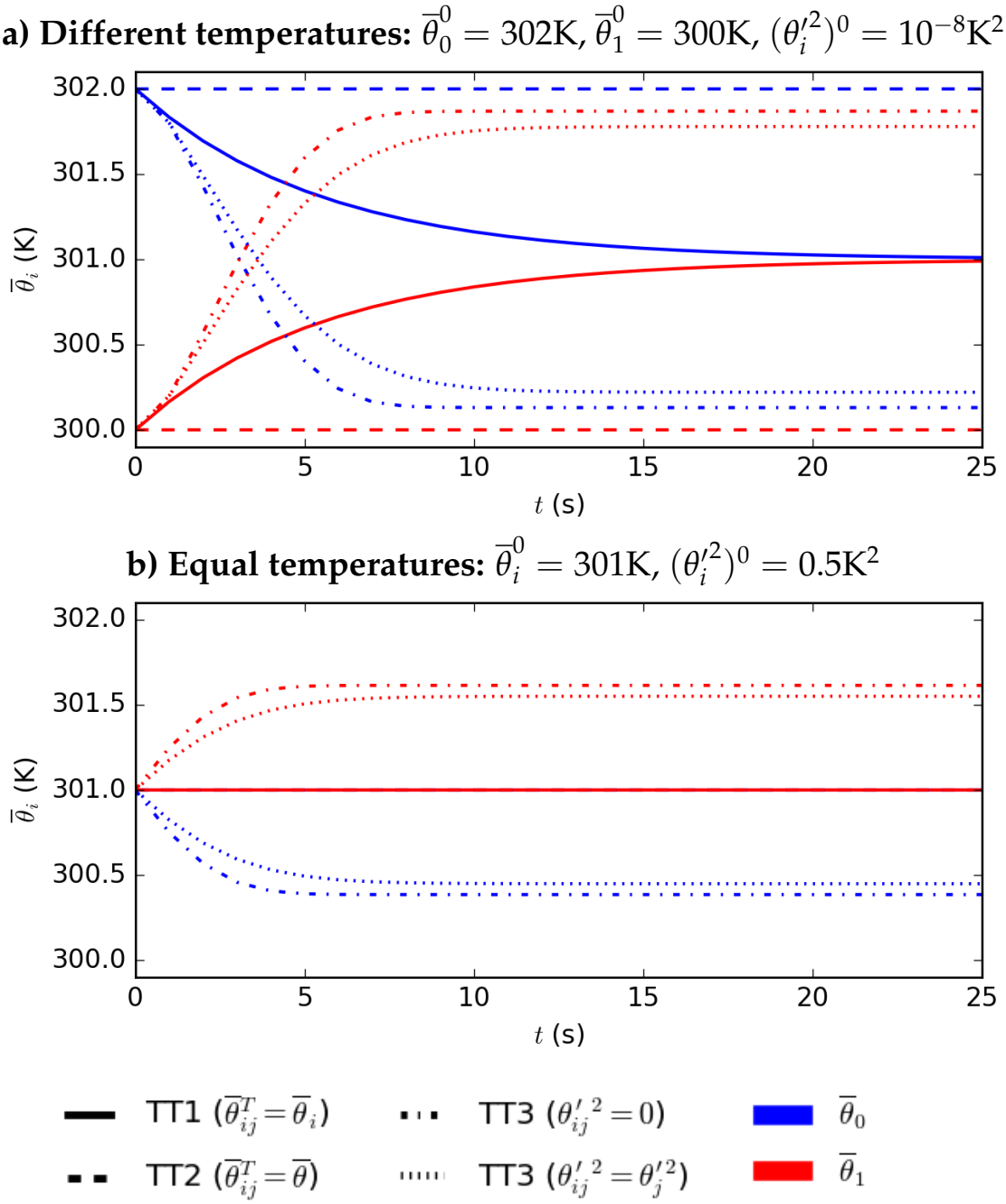

Figure 4.8: The mean potential temperature evolution over 25 timesteps using the four transfer schemes, with initial conditions of $\eta_i^0 = 0.5$ and transfer rates of $\Delta t S_{ij} = 0.1$. The fluids in panel a are initialised with different temperatures and small variances whereas the fluids in panel b start with the same temperature and large variances. Fluid 0 is given by the blue lines and fluid 1 by the red lines. The variance-based schemes allow fluid 1 to be hotter than fluid 0. Note that the blue and red lines for the TT1 and TT2 schemes remain at 301 K throughout the simulation in panel b.

4.2.5 Analysis of the temperature transfer types for dry convection

In section 4.1.4, we diagnosed the mass transfer distributions needed for the 2-fluid 1-column test case by comparing the dynamics to the resolved single-fluid simulation at

a given timestep. By doing this, we were able to identify that the velocity-convergence-based mass transfer term was suitable for representing entrainment and detrainment in our 2-fluid system. Using a similar approach, we will attempt to diagnose the best fluid property transfer methods for the potential temperature.

As the TT3 transfer scheme from section 4.2.3 requires information of the temperature variances, we will include them as prognostic variables in our numerical scheme. We will advect the variance terms according to

$$\frac{\partial \theta_i'^2}{\partial t} + \boldsymbol{u}_i.\boldsymbol{\nabla}\theta_i'^2 = 0, \tag{4.34}$$

from time level n to time level m using the same numerical method used for $\overline{\theta}_i$ from Weller and McIntyre (2019). The variances are initialised by conditionally averaging the resolved fields according to equation 4.5 and the transfers for the variance terms will then be conducted from time level m.

4.2.5.1 Potential temperature transfers

We will analyse the temperature transfers in a similar way to the mass transfers in section 4.1.4. For the resolved single fluid test case, the change in the potential temperature is given by

$$\frac{\theta^{n+1} - \theta^n}{\Delta t} + \left[\boldsymbol{u}.\boldsymbol{\nabla}.\theta\right]^n = 0, \tag{4.35}$$

meaning the new filtered horizontally averaged profile is

$$\begin{aligned} \theta^{n+1}_{HA,i} &= \left\{\theta^n - \Delta t \left[\boldsymbol{u}.\boldsymbol{\nabla}.\theta\right]^n\right\}_{HA,i} \\ &= \theta^n_{HA,i} - \Delta t \left[\boldsymbol{u}.\boldsymbol{\nabla}.\theta\right]^n_{HA,i}. \end{aligned} \tag{4.36}$$

The change in the potential temperature of fluid i for the single-column 2-fluid case is given by

$$\begin{aligned} \frac{\theta_i^{n+1} - \theta_i^n}{\Delta t} + \left[\boldsymbol{u}_i.\boldsymbol{\nabla}\theta_i\right]^n &= \sum_{j\neq i} S_{ji}\frac{\eta_j}{\eta_i}\left(\theta_j - \theta_i\right), \\ \implies \theta_i^{n+1} &= \theta_i^n - \Delta t \left[\boldsymbol{u}_i.\boldsymbol{\nabla}\theta_i\right]^n + \Delta t \sum_{j\neq i} S_{ji}\frac{\eta_j}{\eta_i}\left(\theta_j - \theta_i\right). \end{aligned} \tag{4.37}$$

Like with the mass transfers in section 4.1.4, we want the single-column 2-fluid simulation to accurately represent the resolved single fluid test case. By equating θ_i^{n+1} and

$\theta^{n+1}_{HA,i}$, we can re-arrange to get an expression to diagnose what the temperature transfer terms should be for consistency with the resolved simulation:

$$\Delta t \sum_{j \neq i} S_{ji} \frac{\eta_j}{\eta_i} \left(\theta_j - \theta_i\right) = \theta^n_{HA,i} - \theta^n_i + \Delta t \left[\boldsymbol{u}_i . \boldsymbol{\nabla} \theta_i\right]^n - \Delta t \left[\boldsymbol{u} . \boldsymbol{\nabla} \theta\right]^n_{HA,i} . \tag{4.38}$$

Initialising such that $\theta^n_i = \theta^n_{HA,i}$ for a two fluid system, we get our diagnosed solution for the potential temperature transfers:

$$S_{ji} \frac{\eta_j}{\eta_i} \left(\theta_j - \theta_i\right) = \left[\boldsymbol{u}_i . \boldsymbol{\nabla} \theta_i\right]^n - \left[\boldsymbol{u} . \boldsymbol{\nabla} \theta\right]^n_{HA,i} . \tag{4.39}$$

For transfer schemes TT1, TT2 and TT3, we will use the exact solution for the mass transfer rates from section 4.1.4 to represent entrainment and detrainment (see figure 4.5). Using these transfer rates, we independently apply the transfer schemes to the potential temperature fields at time level m. Figure 4.9 shows the diagnosed temperature transfers needed for consistency with the single-fluid well-resolved test case, as well as the behaviour of four transfer methods.

In the early stages of the test case (figure 4.9.a), the temperature of fluid 1 decreases where entrainment is occurring - this is due to the cooler fluid 0 entering fluid 1. Where there is detrainment, fluid 1 increases in temperature. This is because the coolest parts of fluid 1 are leaving the fluid meaning the mean temperature increases. Entrainment and detrainment occurs above the warm anomaly ($z > 4$ km), but the temperatures do not change as both fluids have $\overline{\theta}_i = 300$ K in this region. All transfer schemes successfully capture the cooling of fluid 1 for $z < 2$ km. Because the TT1 scheme transfers the mean temperature, the properties of the fluid which is losing mass do not change - hence the scheme does not capture the increase in temperature of fluid 1 for 2 km$< z < 4$ km.

At $t = 500$ s (figure 4.9.b), the warm anomaly has risen to $z \approx 5$ km and the hottest regions have become concentrated towards the top of the bubble. This causes the change in shape of the diagnosed temperature transfer from figure 4.9.a. Scheme TT1 once again fails to accurately represent the change in temperature of the fluids. The TT2 ($\overline{\theta}^T_{ij} = \overline{\theta}^m$) and TT3 (Gaussian) schemes predict the temperature change in detraining regions but not the cooling of fluid 1 in the entraining regions. The TT3 scheme which assumes a reference profile variance of $\theta'^2_{ij} = \theta'^2_j$ gives the best agreement with the diagnosed result at this timestep.

The time-averaged transfers (figure 4.9.c) suggest that schemes TT2 and TT3 (with $\theta'^2_{ij} = 0$) best represent the temperature change properties for the rising bubble test case. The alternative TT3 method (with $\theta'^2_{ij} = \theta'^2_j$) also generally produces the correct sign

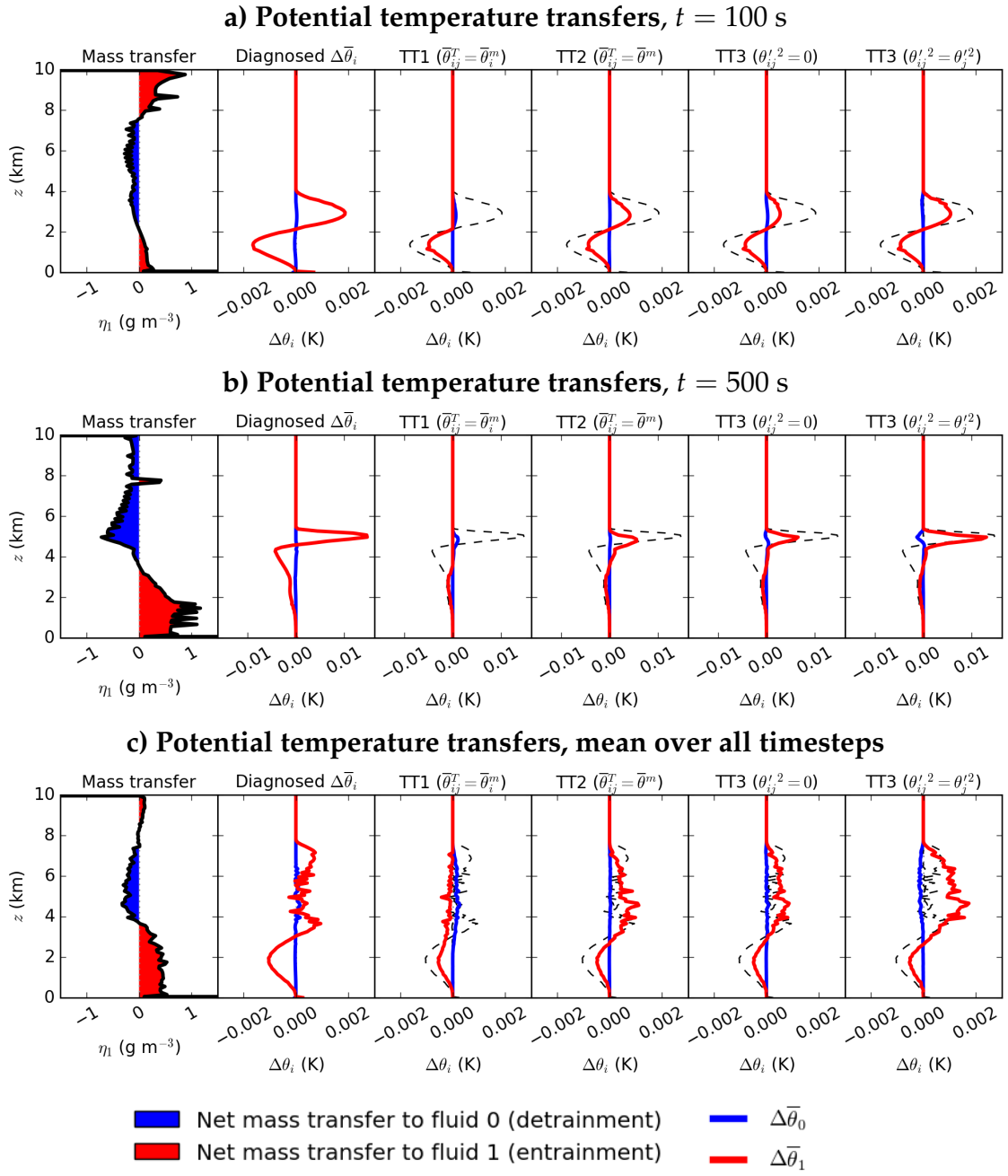

Figure 4.9: The mass transfer at a given timestep (left), the diagnosed temperature transfers needed for consistency with the resolved simulation (second-left), and the temperature changes due to the four transfer methods. Transfers are shown at $t = 100$ s (panel a), $t = 500$ s (panel b) and averaged over one thousand timesteps (panel c). Changes in temperature to the downdraft fluid are given by the blue lines and those for the updraft fluid by the red lines. The dashed lines show the diagnosed potential temperature changes.

of the temperature change but over-estimates it in some scenarios. However, we know from chapter 3 that the TT1 scheme is bounded, whereas schemes TT2 and TT3 are not. This may cause other issues in the two-fluid model which we will discuss in section 4.3.

4.2.5.2 Summary of temperature transfer analysis

We have described and analysed four potential temperature transfer methods. The TT1 scheme transfers the mean temperature and therefore assumes no sub-filter-scale variability. The TT2 scheme assumes that the temperature at the fluid interface is equal to the mean temperature of the fluids. This assumes sub-filter-scale variability but does not specify the exact form of the temperature distribution. The TT3 scheme assumes that the temperature profiles of each fluid are Gaussian, and that hotter regions of fluid 0 are transferred to fluid 1 and cooler regions of fluid 1 are transferred to fluid 0. By assuming $\theta_{ij}'^{2} = 0$, the very hottest and coldest regions of fluids 0 and 1 respectively are transferred. Assuming $\theta_{ij}'^{2} = \theta_{j}'^{2}$, the hottest/coldest regions are more likely to be transferred than other regions of the temperature PDF.

All of the schemes conserve internal energy and momentum but only TT1 can guarantee bounded temperatures (as discussed in chapter 3 and derived in appendix A.2). However, the temperatures converge to the total fluid mean temperature (shown in figure 4.8.a) and the scheme had the worst concordance with the diagnosed temperature changes in section 4.2.5.

The TT2 scheme can prevent the fluid properties from converging (unlike TT1), but the scheme requires correct initialisation of the fluid properties (meaning the hottest regions must be in fluid 1). If this is not done then the fluid 1 temperature will always be equal or less than the fluid 0 temperature, as demonstrated in figure 4.8. Using the correct initial conditions in section 4.2.5, TT2 was able to represent the temperature changes of the rising bubble test case well.

The Gaussian-based TT3 scheme can ensure that fluid 1 is the hotter fluid if enough entrainment and detrainment occurs. Both versions of the scheme ($\theta_{ij}'^{2} = 0$ and $\theta_{ij}'^{2} = \theta_{j}'^{2}$) accurately represented the temperature changes in figure 4.9. The mean temperatures in the TT3 scheme are unbounded when the variances are non-zero but this happens because temperatures hotter and colder than the mean exist in each fluid. This is not an issue as the scheme is merely relabelling these regions and the total temperature variance within a cell is conserved. This is particularly useful for separating the fluids when their mean temperatures are identical (which can not be achieved with schemes TT1 and TT2). However, the TT3 scheme requires an additional budget equation for the variance of each fluid which results in more computational cost.

4.3 Two-fluid dry convection simulations

So far, we have decided how a 2-fluid rising bubble test case should be defined (figure 4.3), identified the need for different pressures in each fluid (section 4.1.3) and analysed how the transfer schemes behave over a single timestep (section 4.2.5). We will now conduct full rising bubble simulations using coarse 2D 2-fluid set-ups.

4.3.1 Initial conditions

The rising bubble test case from Bryan and Fritsch (2002) has a hot anomaly (defined in chapter 3) which is initially at rest. To initialise the two-fluid test case we need to conditionally average the initial fields, but the velocity is zero at $t = 0$ meaning we cannot initialise based on equation 4.1. We instead analyse the velocity field after the first timestep of the resolved single-fluid simulation, shown in figure 4.10. We observe that the $w = 0$ m s^{-1} boundary lies at $x \approx \pm 1.2$ km. We therefore choose to horizontally average the initial resolved field such that

$$I_1 = \begin{cases} 1 & \text{for } |x| \leq 1.2\text{km}, \\ 0 & \text{otherwise}, \end{cases} \tag{4.40}$$

and $I_0 = 1 - I_1$. This is an approximation of the fluid filter described in equation 4.1 and is chosen for simplicity. We note that the $w = 0$ m s^{-1} boundary diverges from $x \approx \pm 1.2$ km above the bubble - but as all fields are horizontally homogeneous above $z = 4$ km it does not matter how these regions are initialised.

By conditionally averaging the resolved fields according to equations 4.2-4.5, we obtain initial conditions for the fluid volume fractions, fluid mean properties and variances which will be the initial conditions for the 2-fluid 1-column scheme. These initial profiles are shown in figure 4.11.

4.3.2 Using the pressure perturbation term

In section 4.1.3, we identified that a pressure perturbation term proportional to the velocity divergence was a realistic stabilsation for the multi-fluid equations. Figure 4.12 shows the final profiles for the two-fluid one-column model ($t = 1000$ s), using the pressure perturbation term with $\gamma = 0.02$ s and no mixing ($S_{ij} = 0$). The scheme clearly exhibits some vertical heat transport (unlike the one-fluid one-column case, figure 4.1), but the temperature anomaly only reaches ~ 7 km rather than the 8 km achieved by the

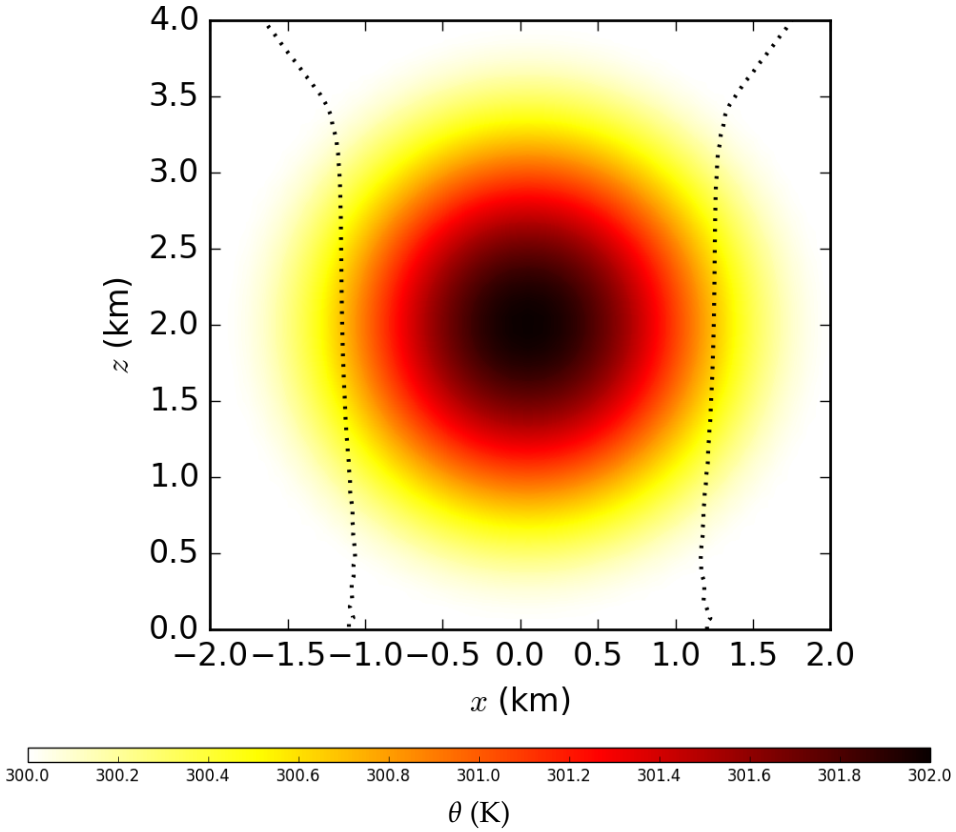

Figure 4.10: The potential temperature field of the single-fluid rising bubble after one timestep ($t = 1$ s). The dotted line shows the $w = 0$ m s^{-1} contour. The region inside $x \approx [-1.2, 1.2]$ km is ascending and the regions outside the dotted lines are descending.

well-resolved single-fluid scheme (see greyed-out profiles). Also note that unphysical spikes exist in the velocity profiles. One reason for this behaviour is the convergence to a one-fluid system at $z \approx 2.5$ km, where $\sigma_1 \to 1$. We have already seen in figure 4.1 that a one-column one-fluid system cannot move due to continuity. The dominance of fluid 1 in this region therefore acts like a barrier, inhibiting the fluids from rising/descending past this region. Such a build up of fluid 1 occurs due to the convergence of the updraft fluid, where buoyant parcels catch up to slightly-less-buoyant parcels. The lack of any transfer terms between the fluids therefore proves critical here, as updraft convergence is often associated with entrainment/detrainment processes.

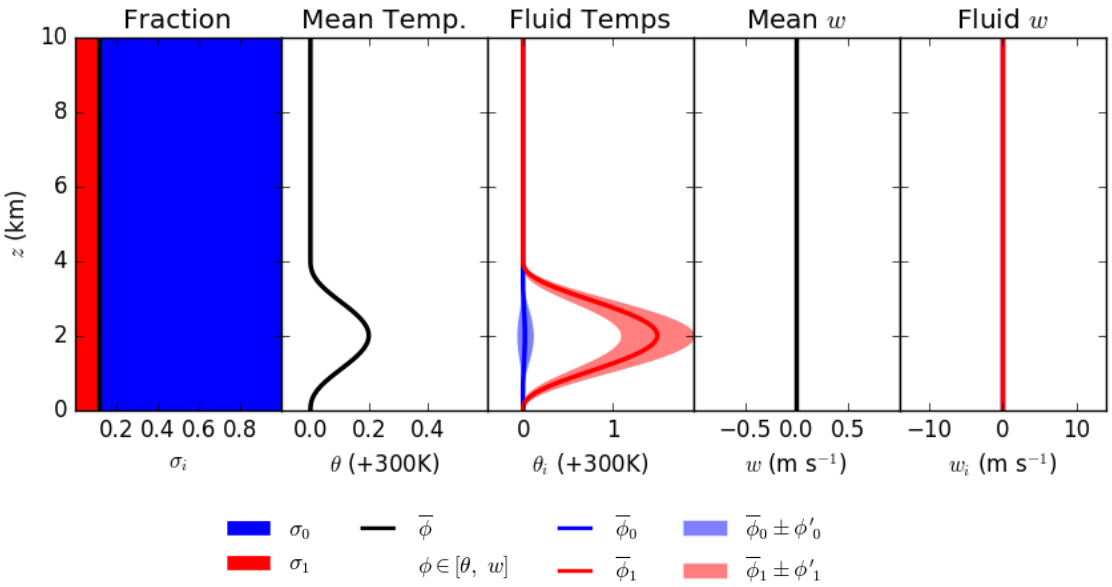

Figure 4.11: The initial conditions of the one-column two-fluid system, diagnosed by filtering the well-resolved bubble according to temperature and subsequently horizontally averaging. Fluid 0 features are represented in blue and fluid 1 features in red. Solid lines show the mean quantities and the transparent shaded zones show the one-standard-deviation regions. Both fluids are initially at rest. Note that that the volume fraction of fluid 1 is given by the black line (left panel) whereas the fraction of each fluid present in a given layer is represented by the opaque blue (fluid 0) and red (fluid 1) regions.

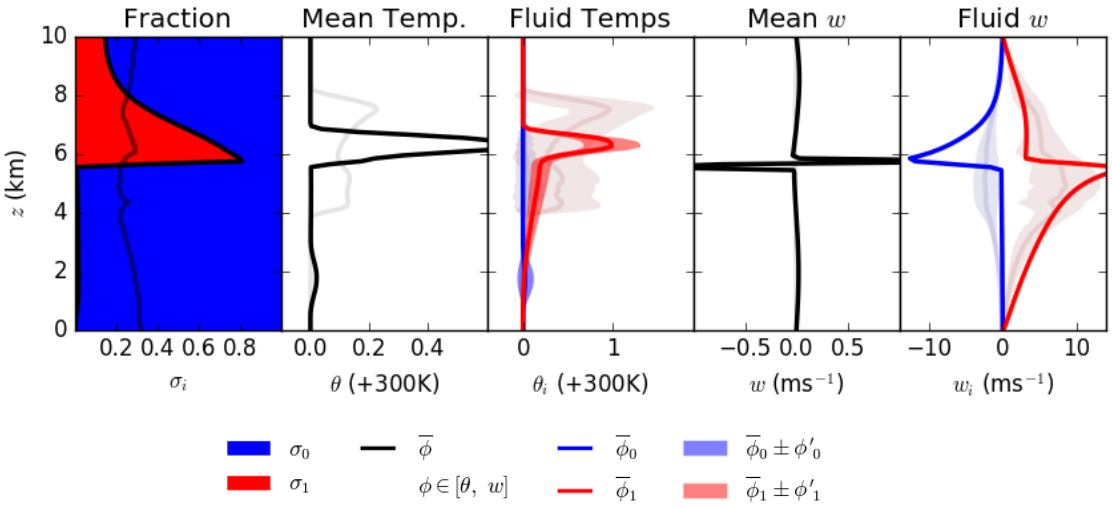

Figure 4.12: The two-fluid system after 1000 s using the pressure perturbation term as stabilization ($\gamma = 0.02$ s). Fluid 0 features are represented in blue and fluid 1 features in red. Solid lines show the mean quantities and the transparent shaded zones show the one-standard-deviation regions. Discontinuities in the velocity profiles appear where the updraft fluid volume fraction approaches 1.

4.3.3 Pressure perturbation term + convergence-based mass transfer

In section 4.1.4, we identified a velocity-convergence-based transfer term (MT3) which accurately represents the entrainment and detrainment processes which exist in the

rising bubble test case. Without entrainment or detrainment, we get a "bunching up" of fluid like in figure 4.12.

We have not yet diagnosed an exact value for γ, the timescale which determines the magnitude of the fluid pressure anomaly term ($\pi_i' = -\gamma \boldsymbol{\nabla}.\boldsymbol{u}_i$). Figure 4.13 shows the root-mean-squared (RMS) error of the temperature distributions (relative to the single-fluid θ) at $t = 1000$ s for a range of values for γ, where the error is given by

$$\varepsilon_{\text{RMS}} = \sqrt{\frac{1}{V_{Tot}} \int_{0\text{km}}^{10\text{km}} \left(\bar{\theta}^{1000} - \bar{\theta}^{1000}_{\text{HA}}\right)^2 A \, dz}, \tag{4.41}$$

A is the cross-sectional area of the column and V_{Tot} is the total volume of the column.

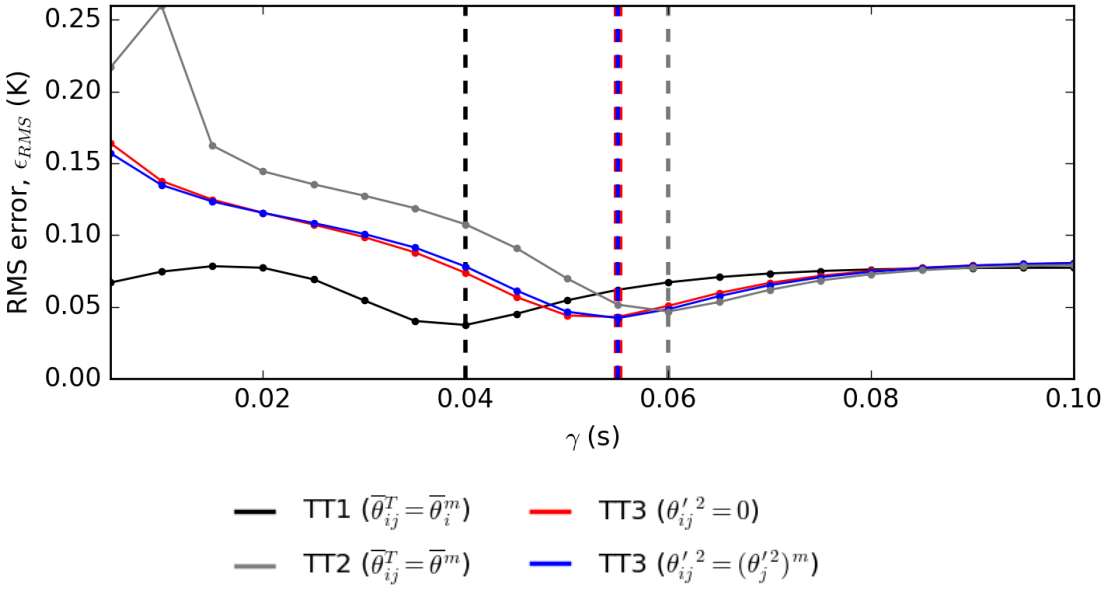

Figure 4.13: The RMS Error of the two-fluid potential temperature distributions after 1000 s for various values of γ. The two-fluid scheme is using the pressure perturbation and the convergence-based mass transfer. The minima of the rms errors for each scheme are indicated by the location of the dashed lines.

The RMS error is minimised when $\gamma = 0.04$ s for TT1, $\gamma = 0.06$ s for TT2 and $\gamma = 0.055$ s for both TT3 schemes. In section 4.1.3, we showed that the derived value of γ based on the scale analysis was 0.2 s - within an order of magnitude but approximately four times greater than the optimum values according to figure 4.13. But the buoyancy anomaly and length scale used in the scale analysis are based on the initial conditions and these values differ later in the test case. We will use the γ values which correspond to the minimum RMS error for our 2-fluid simulations.

Figure 4.14 shows the 2-fluid test case using the pressure perturbation term and the velocity-convergence mass transfer term with the TT1 scheme which transfers the mean fluid temperatures (figure 4.14.a) and the TT2 scheme which transfers the mean potential temperature of the whole cell (figure 4.14.b).

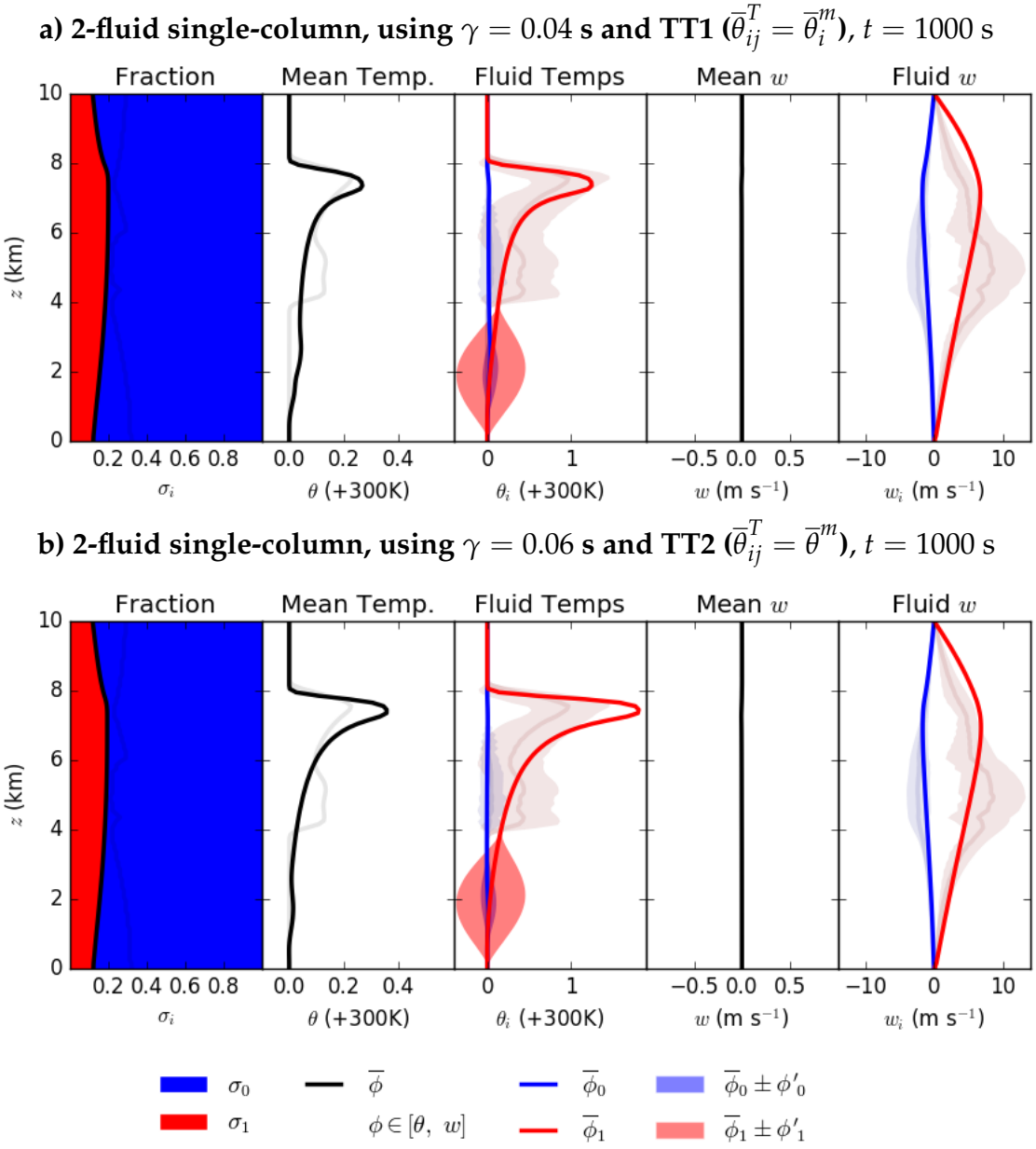

Figure 4.14: The two-fluid system after 1000 s using the pressure perturbation and divergence transfer terms. Fluid 0 features are represented in blue and fluid 1 features in red. Solid lines show the mean quantities and the transparent shaded zones show the one-standard-deviation regions. Panels a and b show the results using temperature transfer schemes TT1 and TT2 respectively.

The 2-fluid scheme performs well with the addition of entrainment and detrainment terms. Using the optimum pressure perturbation magnitudes from figure 4.13, both the

TT1 and TT2 schemes are able to transport the hot anomaly to $z = 8$ km. The mean temperature profiles show similar features to the horizontally averaged single-fluid test case with a maximum at $z \approx 8$ km and a trailing tail. The peak temperature is greater using the TT2 scheme as less of the hot anomaly has been left behind in the 2 km$< z <$ 4 km region. The individual fluid temperatures from the TT1 scheme match closely to the diagnosed solution, whereas the TT2 fluid 1 temperature is 1 K too large. Note that the mean temperature profile for the TT2 scheme is greater than 300 K everywhere despite being an unbounded transfer scheme, but the scheme may not be bounded for other test cases. The fluid 1 vertical velocities deviate from the single-fluid case with lower vertical velocities in the 2 km$< z <$ 6 km region - this is partly the source of the errors in potential temperature in this region. Both TT1 and TT2 schemes keep the initial temperature variance from the initial conditions in the 0 km$< z <$ 4 km region. This is because these schemes do not use a transport equation for the temperature variance.

Figure 4.15 shows the 2-fluid simulation results using the two TT3 temperature schemes, which assumes that the temperature profiles are Gaussian in each fluid. Both methods produce similar temperature profiles at $t = 1000$ s, where the peak temperatures are between those from the TT1 and TT2 schemes from figure 4.14. As well as the variance sources and sinks derived in section 4.2.3, the variance fields are advected according to equation 4.34. Note that both of the TT3 schemes produce temperatures below 300 K at $z \approx 1$ km as the transfers are not bounded. This is a consequence of variance in fluid 0 which implies that the fluid contains temperatures less than 300 K which is not the case in our initialisation. This is undesirable and reduces the accuracy of the scheme, but this does not cause any stability issues in the 2-fluid rising bubble test case. The issue could be addressed by incorporating skewness into the potential temperature profiles but we will not refine the TT3 method in this study.

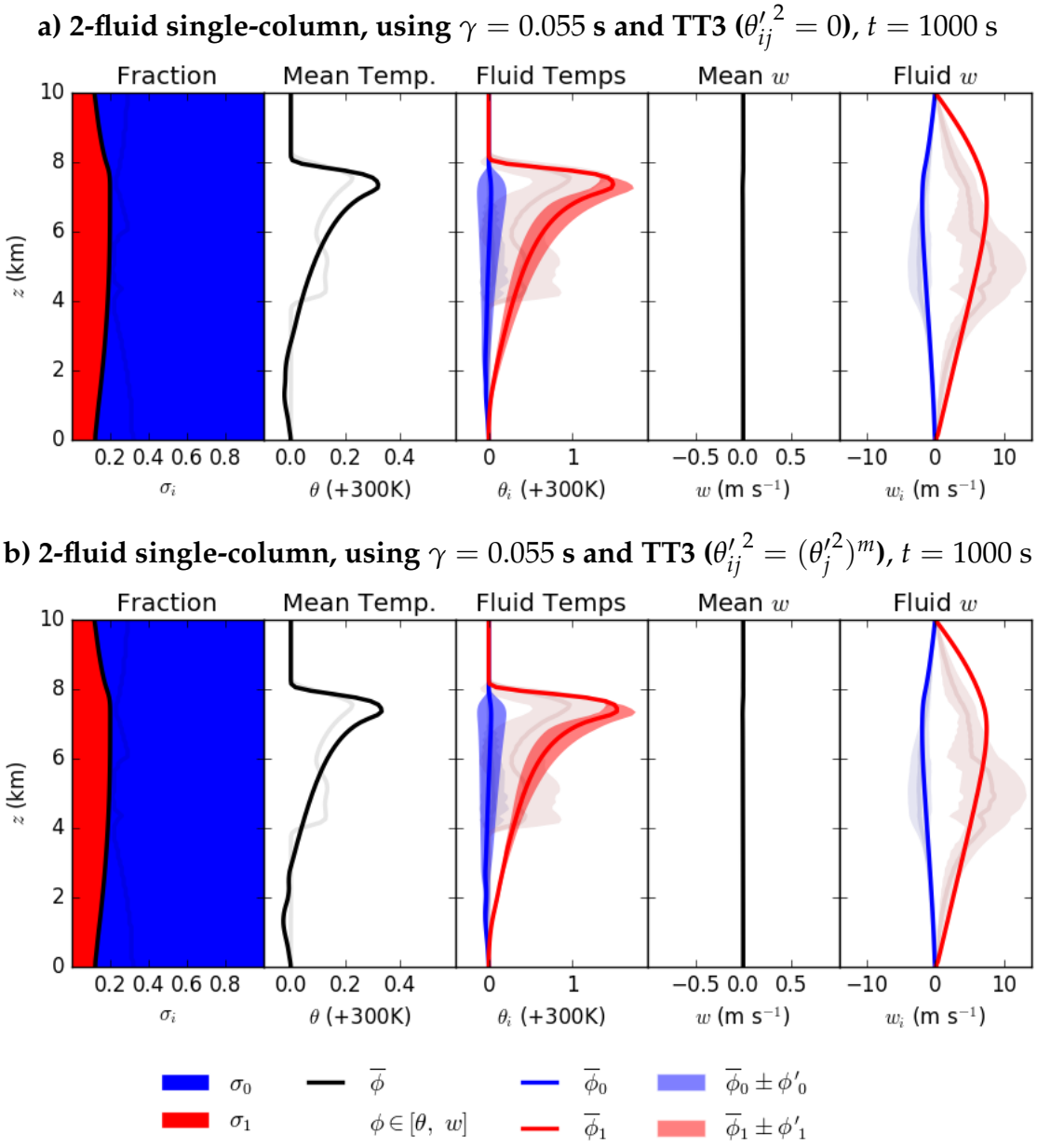

Figure 4.15: The two-fluid system after 1000 s using the pressure perturbation and divergence transfer terms. Temperature transfers are performed using the TT3 scheme which assumes that the temperature profiles in each fluid are Gaussian. Fluid 0 features are represented in blue and fluid 1 features in red. Solid lines show the mean quantities and the transparent shaded zones show the one-standard-deviation regions.

4.3.4 Performance with resolution

We have shown that the two-fluid model can accurately represent dry convection in a single-column, but how does the scheme compare with the single-fluid model across a wider range of resolutions?. We saw in figure 4.1 that the single-fluid equations (without a convection parameterisation) are ineffective in simulating the rising bubble at coarse resolutions, including the grey zone ($\Delta x \sim [1, 100]$ km). With the multi-fluid

scheme, we want to achieve a better-or-equal representation of the heat transport for each resolution, but it should be noted that this is an unfair comparison. In particular, one cannot make any direct comparison with the single-column, single-fluid scheme (without parameterisation) because the hot anomalies are not able to move from their initial conditions. This is not representative of global circulation models without convection parameterisation, where convection is allowed to manifest at the grid scale which transports heat vertically (albeit with unrealistic vertical fluxes; Bechtold et al., 2001; Han and Pan, 2011). Any single-column two-fluid simulations should therefore be compared with the multi-column cases with a single fluid.

Figure 4.16 shows the 2-fluid mean temperature profiles at $t = 1000$ s using the TT1 (mean) transfer scheme across a wide range of resolutions. This includes well-resolved, grey-zone and single-column simulations.

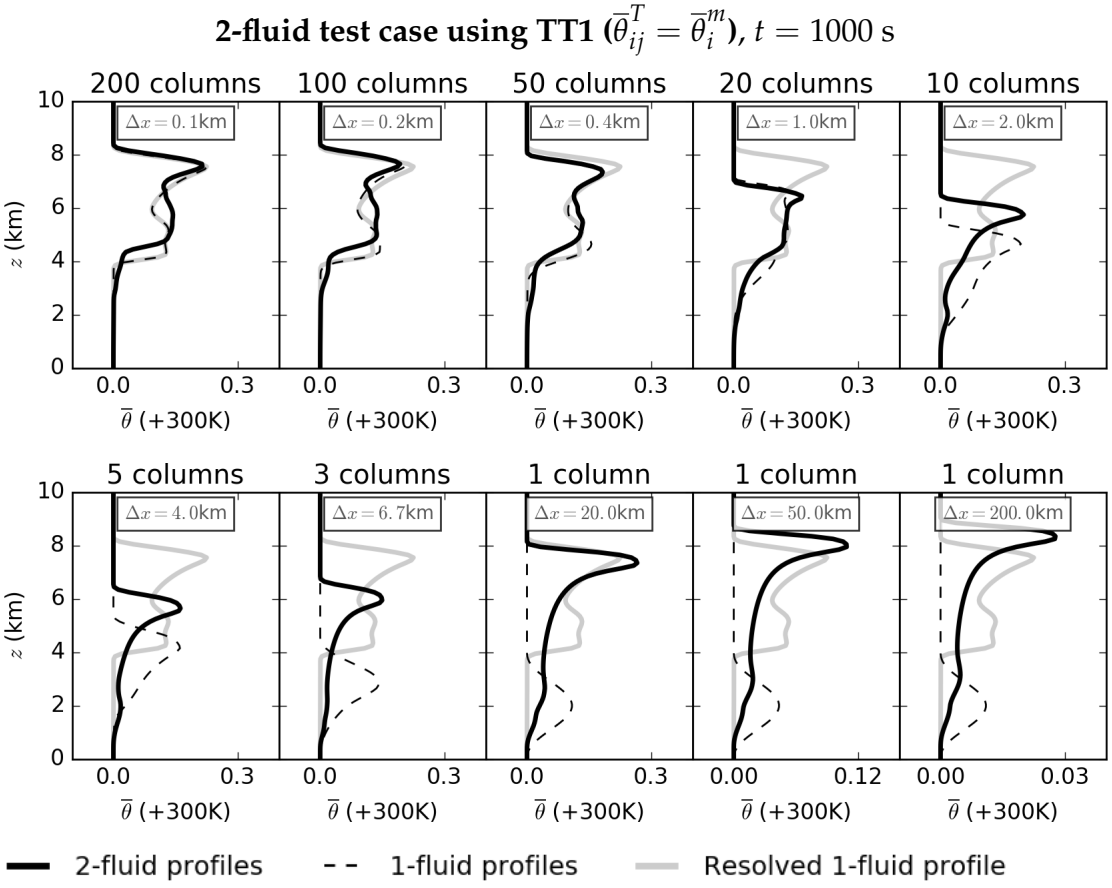

Figure 4.16: The mean temperature profiles (black) of the 2-fluid simulations with TT1 transfers over various resolutions. The grey line shows the temperature profile of the single-fluid scheme with a resolution of $\Delta x = 0.1$ km. The dashed line shows the performance of the 1-fluid scheme at the labelled resolution.

The 2-fluid scheme performs similarly or better than the single-fluid simulations.

We note that there are small discrepancies with the single-fluid results with 200 columns where they should ideally be identical. These differences are caused by the pressure perturbation term as the velocity divergence is not exactly zero. The 2-fluid scheme performs far better at all grey-zone resolutions relative to the single-fluid scheme, with improved heat transport properties. This is because the two fluids are able to move past each other which is particularly important in the single-column case. Nevertheless, the warm bubble falls $1-2$ km short of the $z = 8$ km target at resolutions $\Delta x = [1, 6.7]$ km. The 2-fluid scheme yields the greatest improvement using a single-column set-up as we have tuned our scheme according to single-column analysis in sections 4.1.3, 4.1.4 and 4.2.5. Greater heat transport is observed using wider column widths ($\Delta x > 20$ km) but similar effects are observed using wider domains in the resolved single-fluid test case.

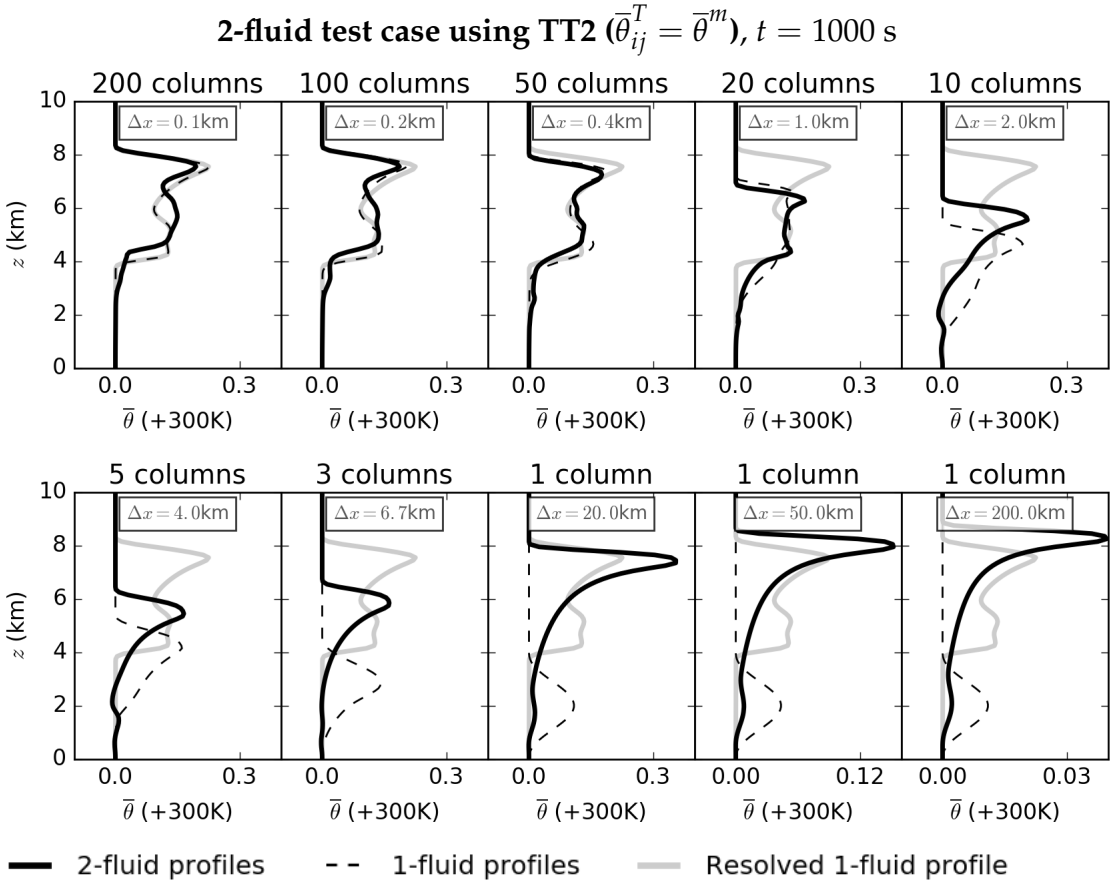

Figure 4.17: The mean temperature profiles (black) of the 2-fluid simulations with TT2 temperature transfers over various resolutions. The grey line shows the temperature profile of the single-fluid scheme with a resolution of $\Delta x = 0.1$ km. The dashed line shows the performance of the 1-fluid scheme at the labelled resolution.

Figure 4.17 shows the potential temperature profiles using the TT2 transfer method for potential temperature. By using the TT2 scheme for the potential temperature, potential temperature maximum is noticeably larger than resolved single fluid test case

(also shown in figure 4.14.b). The scheme produces unbounded temperatures in the 5-column and 10-column cases where $\overline{\theta} < 300$ K.

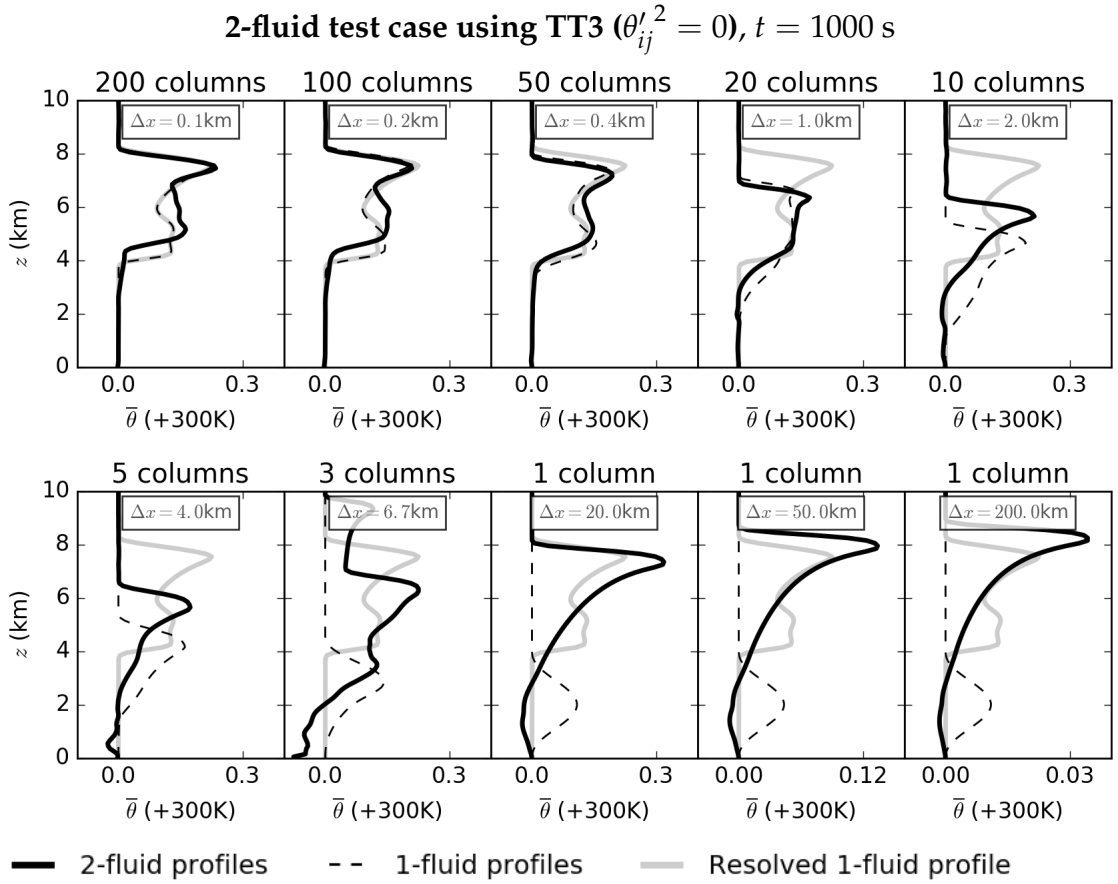

Figure 4.18: The mean temperature profiles (black) of the 2-fluid simulations with TT3 temperature transfers over various resolutions. The grey line shows the temperature profile of the single-fluid scheme with a resolution of $\Delta x = 0.1$ km. The dashed line shows the performance of the 1-fluid scheme at the labelled resolution.

The mean potential temperature profiles for the TT3 ($\theta'^2_{ij} = 0$) scheme are shown in figure 4.18. The profiles are similar to the TT1 and TT2 simulations for high resolutions, although unbounded temperatures exist for all simulations coarser than $\Delta x = 2$ km. Unlike schemes TT1 and TT2, the TT3 ($\theta'^2_{ij} = 0$) achieves heat transport beyond $z = 7$ km for the 3-column simulation, making it the best-performing scheme at this resolution.

Figure 4.19.a shows the RMS error of the temperature profiles relative to the resolved single-fluid temperature ($\overline{\theta}_{\mathrm{HA}}$) at $t = 1000$ s for all temperature transfer methods. The RMS error of the single-fluid scheme relative to highest resolution single-fluid simulation ($\Delta x = 100$ m) is shown by the thick black line. All of the 2-fluid schemes have a smaller RMS error relative to the single-fluid scheme for coarse resolutions (less than 20 columns). We note a sharp decrease in accuracy of all schemes as they approach the grey

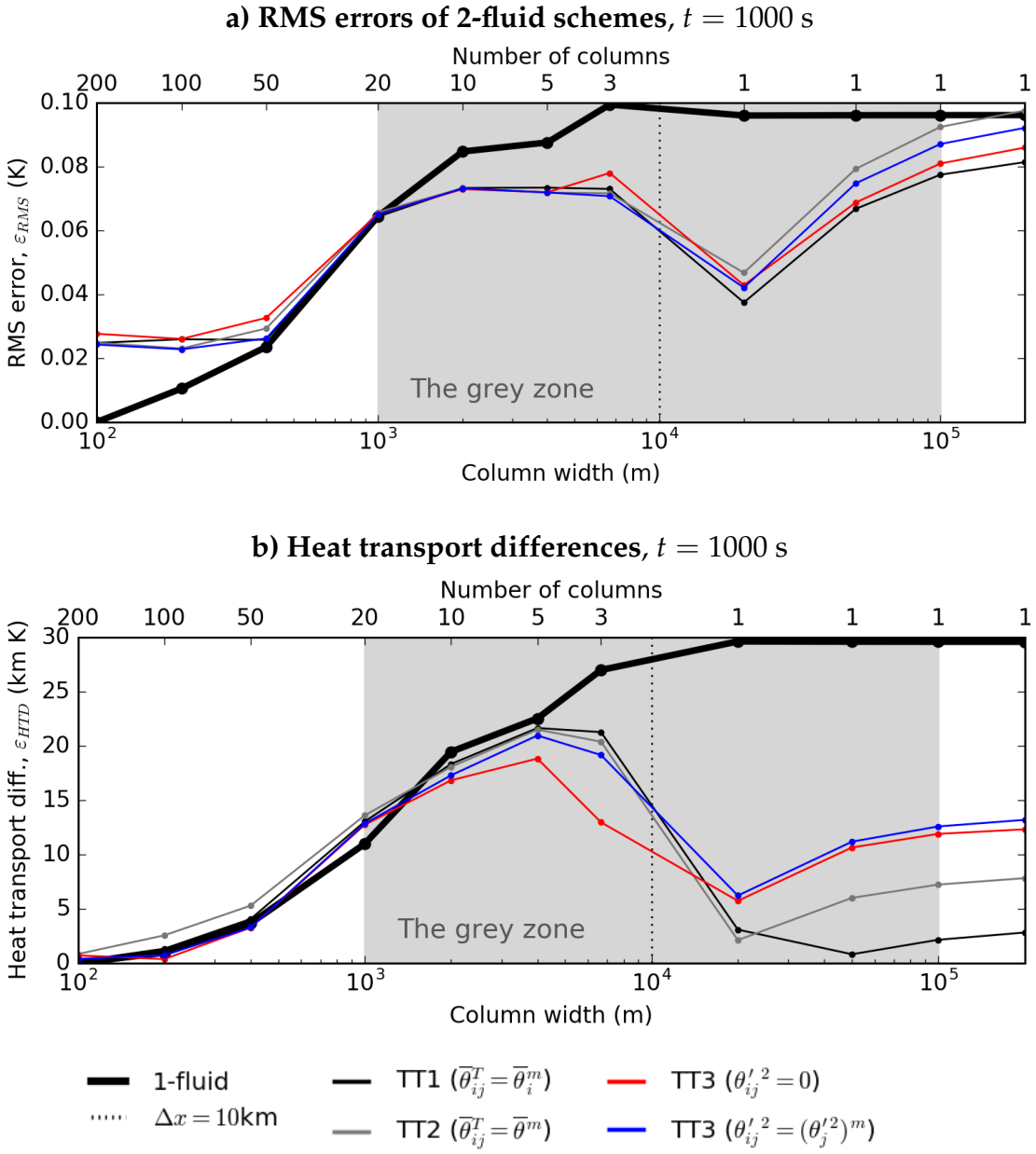

Figure 4.19: The RMS errors of the mean temperature profiles relative to the resolved single-fluid θ at $t = 1000$ s (panel a) and the heat transport difference relative to the resolved single-fluid case (panel b). The thick black line shows the RMS error of the single-fluid scheme over the range of resolutions. The grey region indicates the approximate grey-zone of the test case which is an order of magnitude greater and smaller than the largest circulation (10 km).

zone (defined as an order of magnitude above and below the largest circulation in the test case which is 10 km). As we have tuned the pressure perturbation constant (γ) for the 20 km-wide single-column, the error is larger for wider single-column simulations due to overshooting the 8 km level - although the heat transport properties are very similar. To illustrate this, we also present a measure of the heat transport in figure 4.19.b

which we define as

$$\varepsilon_{\mathrm{HTD}} = \left| \frac{1}{V_{Tot}} \int_{0\mathrm{km}}^{10\mathrm{km}} z\bar{\theta}^{1000} \, A \, dz - \frac{1}{V_{Tot}} \int_{0\mathrm{km}}^{10\mathrm{km}} z\bar{\theta}_{\mathrm{HA}}^{1000} \, A \, dz \right|, \tag{4.42}$$

which measures the heat transport difference relative to the resolved single fluid simulation ($\bar{\theta}_{\mathrm{HA}}^{1000}$). This metric is similar to the time integral of the traditional measure of heat transport ($\int \overline{w'\theta'} dV$) and better showcases the advantages of the 2-fluid schemes. In particular, the 2-fluid single-column set-ups perform better than the single-fluid scheme at any grey-zone resolution. The TT1 scheme (mean temperature) has the best heat transport properties across most single-column set-ups and the TT3 scheme (Gaussian-based with $\theta_{ij}'^{\,2} = 0$) performs best at multi-column grey-zone resolutions.

The 2-fluid schemes are also successful in approximately maintaining the heat transport properties above $\Delta x = 10^4$ km, suggesting that the scheme is scale aware to some extent. But as we have seen in figures 4.16 and 4.17, the accuracy and heat transport properties still need drastic improvement in the 5-20 column range. Moreover, additional constraints should be added so that the scheme exactly approaches the single-fluid solution for high resolution.

These results demonstrate that a 2-fluid scheme can be used to simulate dry convection over a wide range of resolutions, although further work can still be done to improve the heat transport in multi-column grey-zone set-ups.

4.4 Summary and conclusions

We have demonstrated the need for a convection scheme or parameterisation due to the poor performance of the single-fluid scheme in the grey zone for the rising bubble test case (figures 4.1 and 4.19). By applying a conditional filter to the resolved fields ($w \leq 0$ m s^{-1} and $w > 0$ m s^{-1} for fluids 0 and 1 respectively), we were able to average over updraft and downdraft regions to analyse their properties (figure 4.3). These conditionally averaged profiles were used to identify differences in the fluid pressures (figure 4.4) - this can be partially modelled using a fluid pressure anomaly term proportional to the velocity divergence. We also compared various mass transfer parameterisations to model entrainment and detrainment and found that the velocity-convergence-based transfer effectively represented the circulations present in the rising bubble test case (figure 4.5).

We performed a similar analysis for the transfer of fluid properties in entraining and

detraining regions and decided that we should transfer the fluid properties at the fluid interface. This is straightforward for the velocity transfers as we defined the interface at $w = 0$ m s^{-1}. As we do not know the values of the potential temperature at the fluid boundary, we proposed three temperature transfer types:

- **TT1**, which assumes that the mean temperature of each fluid is transferred (as in chapter 3), meaning the fluid temperature profiles are delta functions and have no sub-filter-scale variability. We noted that the mean fluid property transfers from chapter 3 cause the individual velocities and temperatures to converge to the total mean cell temperature (if large transfers occur for a long period of time, as in figure 4.8). The scheme also performed poorly in representing the diagnosed temperature transfers in our analysis from section 4.2.5. However, the scheme still managed to replicate the heat transport properties of the single-fluid test case (see figures 4.14 and 4.19).

- **TT2**, which assumes that the mean temperature of the entire cell is transferred - an approximation for the interface temperature. This scheme assumes some sub-filter-scale temperature distribution but does not define what this profile looks like. The scheme gave better concordance with the diagnosed temperature transfers than the TT1 scheme, especially when you average over all timesteps (figure 4.9.c). The scheme also performs well in the 2-fluid rising bubble simulations but produces significantly higher temperature maxima than the horizontally-averaged resolved test case. TT2 is also unbounded and produces undesirable artefacts in the temperature profile at some resolutions.

- **TT3**, which assumes Gaussian temperature profiles for each fluid. The regions of the temperature profiles transferred are dependent on a Gaussian reference profile with mean $\overline{\theta}_{ij}$ (determined by the transfer rate, S_{ij}) and variance θ'^2_{ij}. We proposed two variations of this scheme which assign different values of the reference profile variance:

  - $\theta'^2_{ij} = 0$: This means that the reference profile is a delta function located at $\overline{\theta}_{ij}$. Anything above $\overline{\theta}_{01}$ is transferred from fluid 0 to 1 and anything below $\overline{\theta}_{10}$ is transferred from fluid 1 to 0. These transferred profiles are not continuous which means that approximating the new profiles as Gaussian's is inaccurate (figure 4.7.a). This transfer method gave good concordance with the diagnosed temperature transfer in figure 4.9.c and yielded satisfactory temperature profiles in the 2-fluid simulations. This 2-fluid scheme was also the only one to transport the heat anomaly above 7 km in the three-column model.
  - $\theta'^2_{ij} = (\theta'^2_{ij})^m$: This means that the reference profile can have a non-zero variance which means that the hottest fluid 0 regions and the coolest fluid 1 regions are more likely to be transferred. This produces a much smoother trans-

ferred profile, as shown in figure 4.7.b. The scheme produced the best concordance with the diagnosed temperature transfers in figures 4.9.b and 4.9.c, and performed similarly to the other 2-fluid schemes for the rising bubble test cases showcased in figure 4.19.

Both of the TT3 schemes produce unbounded temperatures but the total temperature variance over all fluids is conserved. The TT3 schemes also require knowledge of the temperature variance, the variance must either be treated as a prognostic variable or diagnosed each timestep. We have chosen to treat the variance prognostically by advecting it with the velocity field but this adds extra computational cost to the 2-fluid scheme.

By using the pressure perturbation term from section 4.1.3 to stabilise the 2-fluid equations and the velocity-convergence mass transfer from section 4.1.4 to represent entrainment and detrainment, the 2-fluid scheme outperforms the 10-column single-fluid scheme for all grey-zone resolutions.

It is not yet clear which temperature transfer method is better for a 2-fluid model as each scheme has its advantages. As all tranfer schemes generally yield similar results, the TT1 and TT2 schemes work best relative to their computational cost. The Gaussian-based TT3 scheme may become more accurate if variance source and sink terms are included which conserve the total temperature variance over the domain (as in Tan et al., 2018). The TT3 scheme may be particularly useful in modelling the rising bubble test case in the multi-column grey zone set-ups.

This study has demonstrated that the two-fluid scheme is capable of modelling dry convection, but further studies must be completed before the scheme can be used in weather and climate models. Greater consistency for the heat transport at multi-column grey-zone resolutions must be achieved. The inclusion of moisture is also critical in order to model convective clouds - the moist rising bubble test case described in Bryan and Fritsch (2002) could be used as a benchmark for a moist 2-fluid model. The resulting multi-fluid scheme must then be tested, tuned and compared with existing convection parameterisations over a large sample of test cases, and must fulfil the following requirements in future studies:

- When confined to a single column, multi-fluid convection should perform as well as existing parameterisations when using a coarse resolution (multiple convective plumes per column) and large timestep (longer than the circulation turnover time). This was the case in Tan et al. (2018) and Thuburn et al. (2019), where both schemes were compared to existing EDMF schemes. No studies have thus far simulated multi-fluid, moist, deep convection in a single column. In the case where there

are clusters of convective plumes in a column as well as large areas of (initially) stable atmosphere, the multi-fluid scheme should accurately model the compensating subsidence over regions where there is no convection. This may require an accurate model of the sub-filter-scale variability to determine the number of convective plumes per column and their horizontal distributions. Alternatively, assuming that the downdraft fluid subsides uniformly (like in figure 4.14) may be sufficient in most circumstances.

- Multi-fluid convection schemes should perform better than existing parameterisations when:
  - The timestep is comparable to (or smaller than) the convective circulation turnover time.
    In this case, the convective memory of the multi-fluid scheme will allow for the accurate evolution of convective plumes (which is not present in traditional parameterisations).
  - The multi-fluid scheme is not restricted to one column.
    This means that compensating subsidence is not confined to one column and convective plumes can propagate to adjacent columns. This effect is significant when the horizontal length scale of convection is comparable to (or greater than) the column width.

  As an example, the multi-fluid method should show superior performance for moist deep convection when $\Delta x < 5$ km (using the ARM[1] case; Stokes and Schwartz, 1994, for example), and for shallow convection when $\Delta x < 0.5$ km (using the BOMEX[2] case study; Holland and Rasmusson, 1973, for example).

- Convergence should be achieved at high resolution, which is a common issue in existing parameterisations (Arakawa, 2004; Holloway et al., 2014). A moist multi-fluid scheme should converge to the real solution at high resolution, much like the dry convection case presented in figure 4.16.

- Multi-fluid schemes should accurately maintain the labelling of the fluids according to their definition. In our case, this means ensuring falling air is always labelled as fluid 0 and rising air as fluid 1 (like in figures 4.14 and 4.15). This may help to accurately model the life cycle of clouds, as well as oscillating air in the form of gravity waves.

[1] Atmospheric Radiation Measurement
[2] Barbados Oceanographic and Meteorological Experiment

Chapter 5

Summary and Conclusions

5.1 Summary

Atmospheric convection is parameterised in most operational weather and climate models because the horizontal length scales of convective clouds have historically been much smaller than the grid spacing. Recent advances in computational power have allowed models to run at higher resolutions such that the grid lengths are within an order of magnitude of the widths of shallow and deep convective clouds in some cases. This is the convective modelling grey zone, where the resolution is still too coarse to fully resolve the clouds, but also too fine to make common parameterisation assumptions such as neglecting net mass transport by convection. In chapter 1, we summarised some common and some new parameterisation techniques such as bulk and stochastic schemes. A common issue with these schemes is the lack of mass transport by convection, as well as no convective memory or scale awareness.

The multi-fluid technique (which uses conditional filtering) is a potential candidate for improving the representation of convection in models. The method separates regions of the atmosphere into different fluid components (updraft and downdraft regions in this case), each with their own prognostic equations. All fluids are therefore treated consistently and are defined everywhere, which means that convection is always simulated by the dynamical core and the convective fluid is not restricted to a single column (unlike most parameterisations). Net mass transport by convection is therefore represented with the multi-fluid method.

The multi-fluid equations are known to be unstable if they share the same pressure (Stewart and Wendroff, 1984). Thuburn et al. (2019) noted that the instability takes the form of a Kelvin-Helmholtz instability in the incompressible 2-fluid equations for convection. In chapter 2, we extended their analysis and found that using pressure differences proportional to velocity convergence (also used in chapter 4) significantly damped the unstable modes. The instability was completely removed by using transfer terms between fluids which are also proportional to convergence.

In chapter 3, we derived and analysed various numerical schemes for transferring mass between fluids for regions of entraining or detraining air. We assumed that the mass transferred carries the mean temperature and velocity of the fluid from which it originated. From a total of twenty numerical schemes, an implicit scheme was found to have all of the stated desirable numerical properties: positive mass, bounded velocities and temperatures, potential and internal energy conservation, and kinetic energy diminishing for all timesteps. Another scheme which conducted mass transfers explicitly (but velocity/temperature transfers implicitly) was also found to have these properties when the mass fraction transferred was limited to be less than one - this is the scheme used in Weller and McIntyre (2019).

In chapter 4, we conditionally averaged the single-fluid rising bubble test case using a vertical velocity filter to get the diagnosed vertical profiles for our 2-fluid system (where fluid 0 is the downdraft fluid and fluid 1 is the updraft fluid). These conditionally averaged profiles were used to show that differences in pressure between the two fluids exist, which can be approximated by modelling a pressure perturbation in each fluid with $\pi_i' = -\gamma \boldsymbol{\nabla}.\boldsymbol{u}_i$. We also diagnosed where (and how strongly) entrainment and detrainment should occur by comparing the movement of the fluid interface in the resolved single-fluid test case with the advection of the single-column 2-fluid scheme (for a given timestep). We found that a transfer proportional to the velocity convergence was an accurate representation of the entrainment and detrainment but additional transfers may be required to move buoyant air into the updraft fluid. Similar analyses were performed for the the transfer of potential temperature in regions of entrainment and detrainment. The performance of the scheme which transfers mass with the mean fluid temperature (from chapter 3) was compared with three other methods which assumed sub-filter variability within each fluid - these three schemes performed best in the analysis of the rising bubble test case when compared with the diagnosed potential temperature transfer terms.

Using the schemes from chapters 3 and 4, we simulated the two-fluid rising bubble test case over a wide range of resolutions. All 2-fluid schemes performed better than the single-fluid scheme in the grey zone (less than twenty columns). The 2-fluid schemes accurately transported heat for the single-column simulations, which can be partly attributed to the tuning of parameters to single column cases. Vertical heat transport was less accurate for the multi-fluid grey-zone simulations, but the use of two fluids was an improvement over the single-fluid scheme in the grey zone.

5.2 Conclusions, implications and future work

In this thesis, we set out to create a two-fluid model of dry convection, and to understand the challenges involved in creating a multi-fluid convection scheme. In this section we will discuss the various challenges in multi-fluid convection modelling which we have addressed, as well as the hurdles which must be overcome for an operational multi-fluid convection model for weather and climate forecasts.

5.2.1 Stability of the multi-fluid equations and the single pressure assumption

Multi-fluid systems with a shared pressure are known to be unstable (Stewart and Wendroff, 1984). In an incompressible, two-fluid system, the instability takes the form of a Kelvin-Helmholtz instability (Thuburn et al., 2019), similar to the form of equation 1.31. Additional coupling terms which represent sub-grid- and sub-filter-scale motions are therefore needed to stabilise the multi-fluid equations.

Thuburn et al. (2018) suggested that drag can be used to parameterise pressure differences but Weller and McIntyre (2019) noted that drag coupled the fluids too strongly, forcing the fluids to move as one. Thuburn et al. (2019) diffused the vertical velocity to stabilise their 2-fluid convective boundary layer scheme, but this method can generate large errors in high resolution simulations. In chapter 2, the two-fluid stability analysis from Thuburn et al. (2019) was extended using pressure differences between fluids proportional to convergence. The additional pressure term was shown to significantly suppress the Kelvin-Helmholtz-like instability, although it did not completely eliminate it. Chapter 4 helped clarify why this may be the case:

- Figure 4.4 showed that significant pressure differences between fluids exist for the rising bubble test case. Using a pressure perturbation proportional to velocity convergence ($\pi_i' = -\gamma \boldsymbol{\nabla}.\boldsymbol{u}_i$) was shown to be a good approximation for the conditionally averaged pressure differences.
- When using this pressure approximation without mass transfers, the fluids begin to "bunch up" near the boundaries which causes discontinuities to form where the fluid volume fraction tends towards one (figure 4.12).

By adding a mass exchange term which is also proportional to convergence, the two-fluid scheme in section 4.3 was stable and prevented the build up of fluid in one location. This allowed the fluids to move past each other. This transfer term was shown to fully stabilise the incompressible 2-fluid system in chapter 2, as well as accurately represent the fluid-relabelling in the rising bubble test case (section 4.1.4) and radiative

convective equilibrium test cases (Weller et al., 2020).

The chosen stabilisation techniques have been largely successful for the two-fluid model presented in this thesis. However, different stabilisation terms should be tested when different fluid definitions are adopted. It should also be noted that an exact comparison between the stability analysis from chapter 2 and simulations in chapter 4 cannot be made. Not only does chapter 2 analyse an incompressible system, but there is also no dependence on buoyancy which may affect stability. Moreover, the proposed pressure perturbation term for each fluid does not conserve total energy. In future studies, energy sinks due to the pressure term should be a source for turbulent kinetic energy (as noted in Weller et al., 2020), which will also aid in the accurate modelling of sub-filter-scale variability.

5.2.2 Entrainment and detrainment in multi-fluid convection

An accurate representation of entrainment and detrainment is needed for a multi-fluid convection scheme. In chapter 2, we showed that transferring mass when a fluid is converging stabilises the system. Moreover, the mass transfer diagnosis in chapter 4 showed that entrainment into fluid 1 should occur when $\boldsymbol{\nabla}.\boldsymbol{u}_0 < 0$ and detrainment out of fluid 1 should occur when $\boldsymbol{\nabla}.\boldsymbol{u}_1 < 0$. These transfer rates are similar to the dynamical entrainment described in studies such as Houghton and Cramer (1951) and De Rooy et al. (2013), where the entrainment is proportional to $\partial w_1/\partial z$ in a single column set-up. The convergence based transfer rate for the multi-fluid equations is also used in Weller et al. (2020). However, this parameterisation for entrainment and detrainment does not capture all of the diagnosed behaviour in the rising bubble test case when comparing against the movement fluid interface in the resolved single-fluid simulation. The transfer terms should also move buoyant air into the updraft fluid and negatively buoyant air into the downdraft fluid, which was not necessary in this study because we initialised the hottest regions in the updraft fluid. It should also be noted that the entrainment and detrainment parameterisations change with different definitions of the fluids, meaning new diagnostics should be performed if a different fluid filter is chosen.

The way in which the fluid properties are transferred in entraining or detraining regions also needs to be considered. In Weller and McIntyre (2019) and Thuburn et al. (2019), transferred mass takes the mean temperature of the fluid from which it originated (known as the upwind approximation; De Rooy et al., 2013). Weller and McIntyre (2019) also transfer the mean velocity whereas Thuburn et al. (2019) detrain the mean fluid 1 vertical velocity but entrain $\frac{1}{2}(w_0 + w_1)$ which can be close to zero. The velocity transferred in chapter 4 is similar to Thuburn et al. (2019), but we have specifically chosen to transfer $w = 0\,\mathrm{ms}^{-1}$ in both fluids as this is the value defined at the

fluid interface. We tested a variety of potential temperature transfer methods in chapter 4, including transferring the mean of each fluid, transferring the mean temperature of the cell, and using transfers based on Gaussian temperature pdfs for each fluid. The schemes which performed well in the temperature transfer analysis (section 4.2.5) did not yield an obvious benefit in the 2-fluid simulations (section 4.3). Thuburn et al. (2019) also reported that using the potential temperature transfers which were most consistent with their LES diagnostics produced large errors in their temperature profiles - transferring the mean temperatures yielded more consistent results. It is therefore difficult to conclude which temperature transfer method is best for the multi-fluid equations. Transferring the mean temperature was adequate in the rising bubble test case, but more transfer analyses should be conducted over a broader set of test cases as well as over a greater range of grey zone resolutions.

Our results in chapter 3 also showed that the numerical implementation of a multi-fluid transfer scheme should be carefully considered. Only a small subset of the possible numerical schemes are conservative and numerically stable. It may be intuitive to implement a transfer scheme in which all prognostic variables are treated explicitly or all terms treated implicitly, but these schemes are among those which are not conservative and cause increases in the kinetic energy. Chapter 3 (as well as McIntyre et al., 2020) describes the numerical schemes which should be used for accurately modelling the rising bubble test cases, but more test cases with analytic solutions should be analysed in order to better understand which scheme is generally the most accurate. It should be noted that the aforementioned schemes can also be adjusted for transferring non-mean quantities, used in chapter 4 as well as Weller et al. (2020).

5.2.3 Multi-fluid scheme performance in the grey zone

In chapter 4, we were successful in accurately modelling dry convection in a single-column 2-fluid scheme in the grey zone, and Thuburn et al. (2019) also modelled the dry convective boundary layer using a single-column 2-fluid scheme. In chapter 4 we found that tuning parameters for a single-column 2-fluid scheme is not sufficient for an accurate 2-fluid model across all resolutions. This suggests that the assumptions for the pressure differences and mass transfer terms are not giving a complete representation of the sub-grid-scale physics or are not accurately labelling the fluids. For example, there may be regions of the updraft fluid moving downwards (or the downdraft fluid moving upwards) in the multi-column case. Additional assumptions for entrainment, detrainment and sub-filter-scale variability may therefore be needed for consistent behaviour across coarse and fine resolutions.

Future studies should therefore focus on building multi-fluid convection schemes which are accurate for multi-column grey-zone resolutions. Additional analysis should be conducted, focussing on why the 3-column and 5-column set-ups in chapter 4 (for example) do not perform as well as the single-column case.

5.2.4 Other challenges for multi-fluid convection

As well as the main challenges discussed in this thesis, there are other aspects of the multi-fluid framework which must be addressed in order to produce an operational multi-fluid scheme for weather forecasting and climate modelling:

- **How do we deal with the large Courant number velocities in the z-direction?**
  In single-fluid dynamical cores, the mean vertical velocity for a cell is usually small, as stationary air and downdrafts tend to cancel out the large vertical velocities in convective updrafts. But in our 2-fluid framework, fluid 1 only contains regions of air which are rising, resulting in velocities with large Courant numbers in the vertical. A separate advection scheme which can handle fast velocities may therefore be needed in the z-direction. Implicit advection and semi-Lagrangian advection are potential candidates.

- **How will moisture be modelled?**
  We have not conducted moist multi-fluid convection simulations in this study, and it is not yet clear how moisture will be incorporated into a multi-fluid scheme. Although it would be logical to have all liquid water in the updraft fluid for convective clouds, it would not be a valid assumption for stratiform clouds.
  A variety of prognostic multi-fluid moisture schemes should be tested in future multi-fluid convection studies. The performance of these schemes can be tested using the moist rising bubble test case (Bryan and Fritsch, 2002) as well as test cases based on field studies such as BOMEX (the Barbados Oceanographic and Meteorological Experiment, Holland and Rasmusson, 1973). By analysing moist convection for such test cases, it will be possible to determine which moisture schemes most accurately model convective clouds and other processes in a multi-fluid framework.

- **To what extent should sub-filter-scale variability be modelled?**
  We have discussed the effect of assuming sub-filter variability in the fluid potential temperature distributions for the transfer terms, which yielded no obvious benefit in the 2-fluid rising bubble simulations in section 4.3. This may be because we did not include turbulent sources and sinks in the budget equations for the

temperature variance. It is unclear how much benefit a scheme with sub-filter-scale variability (e.g. double-moment) would provide or how accurate we can expect a single-moment multi-fluid scheme to be. Perhaps a double-moment multi-fluid scheme would drastically improve the heat transport properties for the multi-column grey-zone set-ups, but any improvement from such a scheme must be measured relative to the increase in computational cost (as stated by Yano et al., 2018). As a multi-fluid scheme is already more expensive than a single-fluid dynamical core, improvements from a double-moment scheme may be limited relative to the computational cost.

- **Is the $w = 0$ ms^{-1} fluid filter the best definition for multi-fluid convection?**
  In chapter 4, we decided to conditionally average based on the sign of the vertical velocity, but there are other ways of filtering the atmosphere (such as Efstathiou et al., 2019, who include moisture in their filter). Different fluid filters should be tested, especially once moisture is incorporated into the multi-fluid scheme.

- **Is the multi-fluid method worth the cost and resources?**
  We have already discussed how a multi-fluid scheme is more expensive than traditional dynamical cores, but also how the 2-fluid dry convection scheme provides considerable improvements in accuracy across the grey zone (section 4.3). Another issue is the need to overhaul existing code infrastructures to implement multi-fluid convection, unlike conventional convection parameterisations which are often modular and can therefore be replaced more easily. With computational power continuously improving with time, modelling convection explicitly (described in section 1.3.1) may become the preferred method before an operational multi-fluid convection model has been produced, which would allow for the existing models to remain largely unchanged.

All of these issues should be addressed in future studies.

5.2.5 Final remarks

The results presented in this thesis have demonstrated that multi-fluid schemes have the potential to improve grey-zone convection modelling. By analysing simplified equation sets, producing numerically stable schemes for entrainment and detrainment, and analysing conditionally averaged test cases, we have been able to produce a 2-fluid dry convection scheme which transports heat more accurately than a single-fluid model in the grey zone.

We have only analysed dry systems and have not compared the dry multi-fluid scheme with existing parameterisation techniques. We have, however, identified

various issues and challenges which must be addressed for an operational moist multi-fluid convection model such as handling large Courant numbers and modelling sub-filter-scale variability.

Overall, our results show that the multi-fluid method is an exciting new field of convection modelling which could accurately model dry, shallow and deep convection in a single framework and over a large range of resolutions.

Appendix A

Numerical properties of transfer schemes

Here we derive the conservation, boundedness and energy properties of the transfer schemes analysed in chapter 3. These properties are important for a stable numerical method.

A.1 Conservation properties

By multiplying equations 3.13 by 3.16 and summing over both fluid components we get the total mass-weighted properties:

$$\begin{aligned}\eta_0^{n+1}\phi_0^{n+1} + \eta_1^{n+1}\phi_1^{n+1} &= \eta_0^{n+1}\left[(1-\nu_{A10}^{q,r})\phi_0^m + \nu_{A10}^{q,r}\phi_1^m\right] + \eta_1^{n+1}\left[(1-\nu_{A01}^{q,r})\phi_1^m + \nu_{A01}^{q,r}\phi_0^m\right] \\ &= \eta_0^m\phi_0^m + \eta_1^m\phi_1^m - N_{01}\phi_0^m - N_{10}\phi_1^m,\end{aligned} \tag{A.1}$$

where

$$N_{ij} \equiv \lambda_{Cij}\eta_i^m - \lambda_{Cji}\eta_j^m + \nu_{Aji}^{q,r}\eta_i^{n+1} - \nu_{Aij}^{q,r}\eta_j^{n+1}. \tag{A.2}$$

For conservation of internal energy/momentum, we require that $N_{01}\phi_0^m + N_{10}\phi_1^m = 0$. As ϕ_0^m and ϕ_1^m are independent, we additionally impose that $N_{ij} = 0$ for conservation.

Setting $\alpha_A = 0$ and $r = n+1$

By using $\alpha_A = 0$ and $r = n+1$, $\nu_{Aij}^{q,r}\eta_j^{n+1}$ becomes $\Delta t S_{ij}\eta_i^q$ which gives us

$$N_{ij} = \lambda_{Cij}\eta_i^m - \lambda_{Cji}\eta_j^m + \Delta t S_{ji}\eta_j^q - \Delta t S_{ij}\eta_i^q. \tag{A.3}$$

Setting $\alpha_C = 0$ and $q = m$ means that $\lambda_{Cij} = \Delta t S_{ij}$ which results in $N_{ij} = 0$, meaning scheme 1 is conservative. If instead we use $\alpha_C = 1$ and $q = n + 1$ (scheme 3), we get

$$\begin{aligned} N_{ij} &= \lambda_{Cij}\eta_i^m - \lambda_{Cji}\eta_j^m + \Delta t S_{ji}\left[(1-\lambda_{Cji})\eta_j^m + \lambda_{Cij}\,\eta_i^m\right] - \Delta t S_{ij}\left[(1-\lambda_{Cij})\eta_i^m + \lambda_{Cji}\eta_j^m\right] \\ &= \lambda_{Cij}\eta_i^m - \lambda_{Cji}\eta_j^m + \lambda_{Cji}\eta_j^m - \lambda_{Cij}\eta_i^m \\ &= 0. \end{aligned} \tag{A.4}$$

Setting $\alpha_A = 1$ and $r = m$

By instead using $\alpha_A = 1$ and $r = m$ (and expanding the η_i^{n+1} terms in equation A.2 to get η_i^m terms), we get

$$N_{ij} = -\frac{1}{1 + \Delta t S_{ij}\frac{\eta_i^q}{\eta_j^m} + \Delta t S_{ji}\frac{\eta_j^q}{\eta_i^m}}\left[\lambda_{Cij}\eta_i^m - \lambda_{Cji}\eta_j^m + \Delta t S_{ji}\eta_j^q - \Delta t S_{ij}\eta_i^q\right]. \tag{A.5}$$

The terms in the parentheses are the same as equation A.3. This means that $N_{ij} = 0$ if $\alpha_C = 0$ and $q = m$ (scheme 2) or if $\alpha_C = 1$ and $q = n + 1$ (scheme 4).

A.2 Boundedness properties

For a 2-fluid system, bounded velocity transfer terms can be generalised by

$$\begin{aligned} \boldsymbol{u}_0^{n+1} &= (1-\beta_{10})\boldsymbol{u}_0^m + \beta_{10}\boldsymbol{u}_1^m, \\ \boldsymbol{u}_1^{n+1} &= (1-\beta_{01})\boldsymbol{u}_1^m + \beta_{01}\boldsymbol{u}_0^m, \end{aligned} \tag{A.6}$$

where $0 \leq \beta_{ij} \leq 1$ ensures the new velocities are bounded. Method 1 has $\beta_{ij} = \nu_{Mij}^{q,r}$ (defined in equation 3.17). $\nu_{Mij}^{q,r}$ is clearly positive given positive mass and transfer rates. To investigate whether $\nu_{Mij}^{q,r} \leq 1$, we make the denominator small (the worst case scenario) such that $S_{ji} = 0\ \mathrm{s}^{-1}$. This gives

$$\begin{aligned} \nu_{Mij}^{q,r} = \frac{\Delta t S_{ij}\frac{\eta_i^q}{\eta_j^r}}{1 + \alpha_M \Delta t S_{ij}\frac{\eta_i^q}{\eta_j^r}} &\leq 1 \\ \Delta t S_{ij}\frac{\eta_i^q}{\eta_j^r} &\leq \frac{1}{1-\alpha_M}. \end{aligned} \tag{A.7}$$

This boundedness condition is guaranteed if $\alpha_M = 1$. A special case also exists for scheme 1 where $\alpha_C = \alpha_M = 0$, $q = m$, $r = n + 1$ and the boundedness condition is

$\Delta t S_{ij}\eta_i^m/\eta_j^{n+1} \leq 1$. Given that $\eta_j^{n+1} = (1-\Delta t S_{ji})\eta_j^m + \Delta t S_{ij}\eta_i^m \geq \Delta t S_{ij}\eta_i^m$, the scheme is bounded for $\Delta t S_{ij} \leq 1$.

When $\alpha_M = \alpha_C$, method 2 has $\beta_{ij} = \frac{\lambda_{Cij}\eta_i^m}{\lambda_{Cij}\eta_i^m + (1-\lambda_{Cji})\eta_j^m}$ which is bounded if $0 \leq \lambda_{Cij} \leq 1$. This is always true for $\Delta t S_{ij} \leq 1$, although boundedness is also guaranteed for $\Delta t S_{ij} > 1$ when $\alpha_C = \alpha_M = 1$.

A.3 Energy properties

For method 2, the total momentum is conserved if the new momenta ($\boldsymbol{F}_i^{n+1}$) satisfy

$$\begin{aligned} \boldsymbol{F}_0^{n+1} &= (1-\lambda_{M01})\boldsymbol{F}_0^m + \lambda_{M10}\boldsymbol{F}_1^m, \\ \boldsymbol{F}_1^{n+1} &= (1-\lambda_{M10})\boldsymbol{F}_1^m + \lambda_{M01}\boldsymbol{F}_0^m, \end{aligned} \tag{A.8}$$

where $\boldsymbol{F}_i^m \equiv \eta_i^m \boldsymbol{u}_i^m$. The new kinetic energy after transfers have been applied is found by multiplying equations A.6 and A.8 and summing over all fluids:

$$\frac{1}{2}\boldsymbol{u}_0^{n+1}.\boldsymbol{F}_0^{n+1} + \frac{1}{2}\boldsymbol{u}_1^{n+1}.\boldsymbol{F}_1^{n+1} = \frac{1}{2}\boldsymbol{u}_0^m.\boldsymbol{F}_0^m + \frac{1}{2}\boldsymbol{u}_1^m.\boldsymbol{F}_1^m - \Delta K, \tag{A.9}$$

where $\Delta K \equiv \frac{1}{2}\left(\boldsymbol{u}_0^m - \boldsymbol{u}_1^m\right).\left(\mu_{01}\boldsymbol{u}_0^m - \mu_{10}\boldsymbol{u}_1^m\right)$ and $\mu_{ij} \equiv \left[\lambda_{Mij}(1-\beta_{ij}-\beta_{ji}) + \beta_{ji}\right]\eta_i^m$. When $\mu_{01} = \mu_{10}$ and $\mu_{01} \geq 0$, the kinetic energy will never increase. For method 2 (and when $\alpha_C = \alpha_M$), μ_{ij} is given by

$$\mu_{ij} = \frac{\eta_i^m\eta_j^m\left[(1-\lambda_{Cij})\,\lambda_{Cij}\,\eta_i^m + (1-\lambda_{Cji})\,\lambda_{Cji}\,\eta_j^m\right]}{\left[\lambda_{Cij}\,\eta_i^m + (1-\lambda_{Cji})\,\eta_j^m\right]\left[\lambda_{Cji}\,\eta_j^m + (1-\lambda_{Cij})\,\eta_i^m\right]}, \tag{A.10}$$

which is symmetric and always positive meaning this scheme never produces positive energy changes.

Such a proof is less trivial for method 1 as these schemes conserve momentum differently compared to equation A.8 - $\eta_0 u_1$ and $\eta_1 u_0$ terms are also present with method 1. Instead, the energy changes are calculated over a large range of parameter space and are shown in figure 3.2.a.

Appendix B

Numerical adjustments for an operator-split Crank-Nicolson multi-fluid scheme

The numerical multi-fluid scheme used for this study follows the implementation by Weller and McIntyre (2019), with the exception of operator-split transfers. For a fluid property such as temperature or velocity (ϕ) the solution for the Crank-Nicolson scheme (before transfers) is given by

$$\phi_i^m = \phi_i^n + \Delta t \left[(1-\alpha) \left(\frac{\partial \phi_i}{\partial t} \right)^n + \alpha \left(\frac{\partial \phi_i}{\partial t} \right)^m \right], \tag{B.1}$$

where α is the off-centering coefficient and the $\partial\phi_i/\partial t$ terms represent the advection and F_ϕ in equation 3.10. As $\left(\frac{\partial \phi_i}{\partial t}\right)^n$ is stored from the previous timestep, we must ensure that it remains consistent with the fluid properties when transfers are made. This is done by computing

$$\begin{aligned} \left(\frac{\partial \phi_0}{\partial t} \right)^{n+1} &= (1 - \nu_{A10}^{q,r}) \left(\frac{\partial \phi_0}{\partial t} \right)^m + \nu_{A10}^{q,r} \left(\frac{\partial \phi_1}{\partial t} \right)^m, \\ \left(\frac{\partial \phi_1}{\partial t} \right)^{n+1} &= (1 - \nu_{A01}^{q,r}) \left(\frac{\partial \phi_1}{\partial t} \right)^m + \nu_{A01}^{q,r} \left(\frac{\partial \phi_0}{\partial t} \right)^m, \end{aligned} \tag{B.2}$$

for method 1 schemes and

$$\begin{aligned} \left(\frac{\partial \phi_0}{\partial t} \right)^{n+1} &= \frac{(1 - \lambda_{A01})\, \eta_0^m \left(\frac{\partial \phi_0}{\partial t} \right)^m + \lambda_{A10}\, \eta_1^m \left(\frac{\partial \phi_1}{\partial t} \right)^m}{\eta_0^{n+1}}, \\ \left(\frac{\partial \phi_1}{\partial t} \right)^{n+1} &= \frac{(1 - \lambda_{A10})\, \eta_1^m \left(\frac{\partial \phi_1}{\partial t} \right)^m + \lambda_{A01}\, \eta_0^m \left(\frac{\partial \phi_0}{\partial t} \right)^m}{\eta_1^{n+1}}, \end{aligned} \tag{B.3}$$

for method 2 schemes. $(\partial\phi_i/\partial t)^{n+1}$ is therefore stored for the next timestep (and is not used to calculate ϕ_i^{n+1}). Absence of these terms lead to errors in the numerical solution when using operator-split transfers, especially when a fluid has a small volume fraction

or if large transfers are conducted. These terms are not necessary if the Crank-Nicolson off-centering coefficient is set to $\alpha = 1$ but the scheme will be limited to first-order accuracy in time.

Appendix C

Integrals for Gaussian-based potential temperature transfers between fluids

In chapter 4, we derive transfers for the potential temperature in entraining and detraining regions which assume a Gaussian temperature distribution in each fluid. This allows the hottest air to be transferred out of fluid 0 and the coolest air out of fluid 1. In this section, we present the integrals of the temperature distributions needed for the derivation in chapter 4.

C.1 Error function times Gaussian

By integrating

$$I = A \int_{-\infty}^{\infty} \exp\left(-Bx^2\right) \operatorname{erf}\left(Cx + D\right) dx, \tag{C.1}$$

where A, C, D and E are constants, we get

$$I = A\sqrt{\frac{\pi}{B}} \operatorname{erf}\left(D\sqrt{\frac{B}{B + C^2}}\right). \tag{C.2}$$

Therefore, when we have

$$I = \int_{-\infty}^{\infty} \frac{1}{2}\left[1 + \operatorname{erf}\left(\frac{\theta_0 - \overline{\theta}_1}{\sqrt{2}\theta_1'}\right)\right] \frac{1}{\sqrt{2\pi}\theta_0'} \exp\left[-\frac{(\theta_0 - \overline{\theta}_0)^2}{2{\theta_0'}^2}\right] d\theta_0, \tag{C.3}$$

we can make the substitution $\theta \equiv \theta_0 - \overline{\theta}_0$, giving us

$$I = \int_{-\infty}^{\infty} \frac{1}{2}\left[1 + \operatorname{erf}\left(\frac{\theta_0 + \overline{\theta}_0 - \overline{\theta}_1}{\sqrt{2}\theta_1'}\right)\right] \frac{1}{\sqrt{2\pi}\theta_0'} \exp\left[-\frac{\theta^2}{2{\theta_0'}^2}\right] d\theta. \tag{C.4}$$

Here we have $A = \frac{1}{2\theta_0'\sqrt{2\pi}}$, $C = \frac{1}{2\theta_0'^2}$, $D = \frac{1}{\sqrt{2}\theta_1'}$, $E = \frac{\bar{\theta}_1 - \bar{\theta}_0}{\sqrt{2}\theta_1'}$ which results in

$$I = \frac{1}{2}\left[1 + \operatorname{erf}\left(\frac{\bar{\theta}_0 - \bar{\theta}_1}{\sqrt{2}\sqrt{\theta_0'^2 + \theta_1'^2}}\right)\right]. \tag{C.5}$$

C.2 Mean of error function times Gaussian

We have the integral

$$I = A\int_{-\infty}^{\infty} x \exp\left(-Bx^2\right) \operatorname{erf}\left(Cx + D\right) dx, \tag{C.6}$$

where A, C, D and E are constants. Ng and Geller (1969) provides integral tables for error functions, including one for the above integral if $E = 0$. But no integral is given for the full integrand. Moreover, we can not use integration by parts due to ambiguity of the integration constant from $\int \exp\left(-Cx^2\right) \operatorname{erf}\left(Dx + E\right) dx$. We therefore use the below method.

Let us define

$$y = e^{-Bx^2} \operatorname{erf}\left(Cx + D\right). \tag{C.7}$$

Using the product rule, the differential is

$$\begin{aligned} \frac{dy}{dx} &= -2Bxe^{-Bx^2} \operatorname{erf}\left(Cx + D\right) + \frac{2C}{\sqrt{\pi}} e^{-Bx^2} e^{-(Cx+D)^2} \\ &= -2Bxe^{-Bx^2} \operatorname{erf}\left(Cx + D\right) + \frac{2C}{\sqrt{\pi}} e^{-H} e^{-F(x+G)^2}, \end{aligned} \tag{C.8}$$

where $F = B + C^2$, $G = \frac{CD}{B+C^2}$ and $H = \frac{BD^2}{B+C^2}$. This gives us an expression for our desired integrand:

$$xe^{-Bx^2} \operatorname{erf}\left(Cx + D\right) = \frac{C}{B\sqrt{\pi}} e^{-H} e^{-F(x+G)^2} - \frac{1}{2B}\frac{dy}{dx}. \tag{C.9}$$

Integrating over all space we get

$$\begin{aligned} \int_{-\infty}^{\infty} xe^{-Bx^2} \operatorname{erf}\left(Cx + D\right) dx &= \frac{C}{B\sqrt{\pi}} e^{-H} \int_{-\infty}^{\infty} e^{-F(x+G)^2} dx - \frac{1}{2B} \underbrace{\int_{-\infty}^{\infty} \frac{dy}{dx} dx}_{[y]_{-\infty}^{\infty} = 0} \\ &= \frac{C}{B\sqrt{\pi}} e^{-H} \sqrt{\frac{\pi}{F}} \\ &= \frac{C}{B}\sqrt{\frac{1}{B + C^2}} \exp\left(-\frac{BD^2}{B + C^2}\right). \end{aligned} \tag{C.10}$$

As a sanity check, this solution reduces to that of Ng and Geller (1969) when $D = 0$.

When we have $B = \frac{1}{2\theta_0'^2}$, $C = \frac{1}{\sqrt{2}\theta_1'}$ and $D = \frac{\bar{\theta}_0 - \bar{\theta}_1}{\sqrt{2}\theta_1'}$, we get the solution

$$I = 2\theta_0'^2 \sqrt{\frac{\theta_0'^2}{\theta_0'^2 + \theta_1'^2}} \exp\left[-\frac{(\bar{\theta}_0 - \bar{\theta}_1)^2}{2(\theta_0'^2 + \theta_1'^2)}\right]. \tag{C.11}$$

C.3 Second-order moment of error function times Gaussian

We have the second-order moment integral given by

$$I = A \int_{-\infty}^{\infty} x^2 \exp\left(-Bx^2\right) \operatorname{erf}(Cx + D)\, dx, \tag{C.12}$$

where A, C, D and E are constants. Using the same method as section C.2, we define

$$y = xe^{-Bx^2} \operatorname{erf}(Cx + D). \tag{C.13}$$

By differentiating, we get

$$\begin{aligned} \frac{dy}{dx} &= e^{-Bx^2} \operatorname{erf}(Cx + D) - 2Bx^2 e^{-Bx^2} \operatorname{erf}(Cx + D) + \frac{2C}{\sqrt{\pi}} x e^{-Bx^2} e^{-(Cx+D)^2} \\ &= e^{-Bx^2} \operatorname{erf}(Cx + D) - 2Bx^2 e^{-Bx^2} \operatorname{erf}(Cx + D) + \frac{2C}{\sqrt{\pi}} x e^{-H} e^{-F(x+G)^2}, \end{aligned} \tag{C.14}$$

where $F = B + C^2$, $G = \frac{CD}{B+C^2}$ and $H = \frac{BD^2}{B+C^2}$. Rearranging, we get

$$x^2 e^{-Bx^2} \operatorname{erf}(Cx + D) = \frac{1}{2B} e^{-Bx^2} \operatorname{erf}(Cx + D) + \frac{C}{B\sqrt{\pi}} x e^{-H} e^{-F(x+G)^2} - \frac{1}{2B} \frac{dy}{dx}. \tag{C.15}$$

Integrating over all space therefore gives us

$$\begin{aligned}\int_{-\infty}^{\infty} x^2 e^{-Bx^2}\operatorname{erf}(Cx+D)\,dx &= \frac{1}{2B}\int_{-\infty}^{\infty} e^{-Bx^2}\operatorname{erf}(Cx+D)\,dx \\ &\quad + \frac{C}{B\sqrt{\pi}}e^{-H}\int_{-\infty}^{\infty} x e^{-F(x+G)^2}dx - \frac{1}{2B}\underbrace{\int_{-\infty}^{\infty}\frac{dy}{dx}dx}_{[y]_{-\infty}^{\infty}=0} \\ &= \frac{1}{2B}\sqrt{\frac{\pi}{B}}\operatorname{erf}\left(D\sqrt{\frac{B}{B+C^2}}\right) - \frac{C}{B\sqrt{\pi}}e^{-H}G\sqrt{\frac{\pi}{F}} \\ &= \frac{1}{2B}\sqrt{\frac{\pi}{B}}\operatorname{erf}\left(D\sqrt{\frac{B}{B+C^2}}\right) - G\frac{C}{B}\sqrt{\frac{1}{B+C^2}}\exp\left(-\frac{BD^2}{B+C^2}\right).\end{aligned} \tag{C.16}$$

C.4 Integrals for the mean fluid properties

The integrals necessary for finding the new mean potential temperature ($\overline{\theta}_i^{n+1}$) in section 4.2.3 are presented here. The mean potential temperature of the region transferred from fluid 0 to fluid 1 is given by

$$\begin{aligned}\int_{-\infty}^{\infty}\theta\,\Theta_{01}^m\,d\theta &= \int_{-\infty}^{\infty}\theta\,\frac{1}{2}\left[1+\operatorname{erf}\left(\frac{\theta-\overline{\theta}_{01}^m}{\sqrt{2}{\theta'_{01}}^m}\right)\right]\frac{1}{\sqrt{2\pi}{\theta'_0}^m}\exp\left[-\frac{(\theta-\overline{\theta}_0^m)^2}{2({\theta'_0}^2)^m}\right]d\theta \\ &= \frac{1}{2}\overline{\theta}_0^m + \frac{1}{2{\theta'_0}^m\sqrt{2\pi}}\underbrace{\int_{-\infty}^{\infty}\theta\operatorname{erf}\left(\frac{\theta-\overline{\theta}_{01}^m}{\sqrt{2}{\theta'_{01}}^m}\right)\exp\left[-\frac{(\theta-\overline{\theta}_0^m)^2}{2({\theta'_0}^2)^m}\right]d\theta}_{I_1}.\end{aligned} \tag{C.17}$$

By making the substitution $\theta_0 = \theta - \overline{\theta}_0^m$, I_1 becomes

$$I_1 = \int_{-\infty}^{\infty}(\theta_0+\overline{\theta}_0^m)\operatorname{erf}\left(\frac{\theta_0+\overline{\theta}_0^m-\overline{\theta}_{01}^m}{\sqrt{2}{\theta'_{01}}^m}\right)\exp\left[-\frac{(\theta_0^m)^2}{2({\theta'_0}^2)^m}\right]d\theta_0. \tag{C.18}$$

Using identities C.2 and C.10 (in appendices C.1 and C.2 respectively), we get

$$\begin{aligned}\frac{1}{2{\theta'_0}^m\sqrt{2\pi}}I_1 &= \frac{1}{2}\overline{\theta}_0^m\operatorname{erf}\left(\frac{\overline{\theta}_0^m-\overline{\theta}_{01}^m}{\sqrt{2}\sqrt{({\theta'_0}^2)^m+({\theta'_{01}}^2)^m}}\right) \\ &\quad + {\theta'_0}^m\frac{1}{\sqrt{2\pi}}\sqrt{\frac{({\theta'_0}^2)^m}{({\theta'_0}^2)^m+({\theta'_{01}}^2)^m}}\exp\left[-\frac{1}{2}\frac{(\overline{\theta}_0^m-\overline{\theta}_{01}^m)^2}{({\theta'_0}^2)^m+({\theta'_1}^2)^m}\right].\end{aligned} \tag{C.19}$$

We can now write the mean of the transferred region as

$$\int_{-\infty}^{\infty} \theta\, \Theta_{01}^m \, d\theta = \frac{1}{2}\overline{\theta}_0^m \left[1 + \operatorname{erf}\left(\frac{\overline{\theta}_0^m - \overline{\theta}_{01}^m}{\sqrt{2}\sqrt{(\theta_0'^2)^m + (\theta_{01}'^2)^m}}\right)\right] + \theta_0'^m \frac{1}{\sqrt{2\pi}} \sqrt{\frac{(\theta_0'^2)^m}{(\theta_0'^2)^m + (\theta_{01}'^2)^m}} \exp\left[-\frac{1}{2}\frac{(\overline{\theta}_0^m - \overline{\theta}_{01}^m)^2}{(\theta_0'^2)^m + (\theta_{01}'^2)^m}\right]. \tag{C.20}$$

Applying the same procedure to the region transferred from fluid 1 to fluid 0 gives us:

$$\int_{-\infty}^{\infty} \theta\, \Theta_{10}^m \, d\theta = \frac{1}{2}\overline{\theta}_1^m \left[1 - \operatorname{erf}\left(\frac{\overline{\theta}_1^m - \overline{\theta}_{10}^m}{\sqrt{2}\sqrt{(\theta_1'^2)^m + (\theta_{10}'^2)^m}}\right)\right] - \theta_1'^m \frac{1}{\sqrt{2\pi}} \sqrt{\frac{(\theta_1'^2)^m}{(\theta_1'^2)^m + (\theta_{10}'^2)^m}} \exp\left[-\frac{1}{2}\frac{(\overline{\theta}_1^m - \overline{\theta}_{10}^m)^2}{(\theta_1'^2)^m + (\theta_{10}'^2)^m}\right]. \tag{C.21}$$

C.5 Integrals for the fluid variances

The integrals necessary for finding the new potential temperature variance ($(\theta_i'^2)^{n+1}$) in section 4.2.3 are presented here. The potential temperature variance of the region transferred from fluid 0 to fluid 1 is given by

$$\int_{-\infty}^{\infty} \theta^2 \Theta_{01}^m \, d\theta = \frac{1}{2}\left[(\theta_0'^2)^m + (\overline{\theta}_0^m)^2\right] + \frac{1}{2\theta_0'^m\sqrt{2\pi}} \underbrace{\int_{-\infty}^{\infty} \theta^2 \operatorname{erf}\left(\frac{\theta - \overline{\theta}_{01}^m}{\sqrt{2}\theta_{01}'^m}\right) \exp\left[-\frac{(\theta - \overline{\theta}_0^m)^2}{2(\theta_0'^2)^m}\right] d\theta}_{I_2}. \tag{C.22}$$

By making the substitution $\theta_0 = \theta - \overline{\theta}_0^m$, I_2 becomes

$$I_2 = \int_{-\infty}^{\infty} \left[\theta_0^2 + 2\overline{\theta}_0^m\theta_0 + (\overline{\theta}_0^m)^2\right] \operatorname{erf}\left(\frac{\theta_0 + \overline{\theta}_0^m - \overline{\theta}_{01}^m}{\sqrt{2}\theta_{01}'^m}\right) \exp\left[-\frac{(\theta_0^m)^2}{2(\theta_0'^2)^m}\right] d\theta_0. \tag{C.23}$$

By using identities C.2, C.10 and C.16 (in appendices C.1, C.2 and C.3 respectively), we get

$$\begin{aligned}\frac{1}{2{\theta'_0}^m\sqrt{2\pi}}I_2 = \frac{1}{2}\left[({\theta'_0}^2)^m + (\overline{\theta}_0^m)^2\right]\operatorname{erf}\left(\frac{\overline{\theta}_0^m - \overline{\theta}_{01}^m}{\sqrt{2}\sqrt{({\theta'_0}^2)^m + ({\theta'_{01}}^2)^m}}\right)\\ + 2\overline{\theta}_0^m{\theta'_0}^m\frac{1}{\sqrt{2\pi}}\sqrt{\frac{({\theta'_0}^2)^m}{({\theta'_0}^2)^m + ({\theta'_{01}}^2)^m}}\exp\left[-\frac{1}{2}\frac{(\overline{\theta}_0^m - \overline{\theta}_{01}^m)^2}{({\theta'_0}^2)^m + ({\theta'_{01}}^2)^m}\right]\\ - (\overline{\theta}_0^m - \overline{\theta}_{01}^m){\theta'_0}^m\frac{1}{\sqrt{2\pi}}\left(\frac{({\theta'_0}^2)^m}{({\theta'_0}^2)^m + ({\theta'_{01}}^2)^m}\right)^{\frac{3}{2}}\exp\left[-\frac{1}{2}\frac{(\overline{\theta}_0^m - \overline{\theta}_{01}^m)^2}{({\theta'_0}^2)^m + ({\theta'_{01}}^2)^m}\right].\end{aligned} \tag{C.24}$$

Integral C.22 is therefore given by

$$\begin{aligned}\int_{-\infty}^{\infty}\theta^2\Theta_{01}^m\,d\theta = \frac{1}{2}\left[({\theta'_0}^2)^m + (\overline{\theta}_0^m)^2\right]\left[1 + \operatorname{erf}\left(\frac{\overline{\theta}_0^m - \overline{\theta}_{01}^m}{\sqrt{2}\sqrt{({\theta'_0}^2)^m + ({\theta'_{01}}^2)^m}}\right)\right]\\ + 2\overline{\theta}_0^m{\theta'_0}^m\frac{1}{\sqrt{2\pi}}\sqrt{\frac{({\theta'_0}^2)^m}{({\theta'_0}^2)^m + ({\theta'_{01}}^2)^m}}\exp\left[-\frac{1}{2}\frac{(\overline{\theta}_0^m - \overline{\theta}_{01}^m)^2}{({\theta'_0}^2)^m + ({\theta'_{01}}^2)^m}\right]\\ - (\overline{\theta}_0^m - \overline{\theta}_{01}^m){\theta'_0}^m\frac{1}{\sqrt{2\pi}}\left(\frac{({\theta'_0}^2)^m}{({\theta'_0}^2)^m + ({\theta'_{01}}^2)^m}\right)^{\frac{3}{2}}\exp\left[-\frac{1}{2}\frac{(\overline{\theta}_0^m - \overline{\theta}_{01}^m)^2}{({\theta'_0}^2)^m + ({\theta'_{01}}^2)^m}\right]\end{aligned} \tag{C.25}$$

By applying the same methods, we can also calculate the potential temperature variance of the region transferred from fluid 1 to fluid 0

$$\begin{aligned}\int_{-\infty}^{\infty}\theta^2\Theta_{10}^m\,d\theta = \underbrace{\frac{1}{2{\theta'_1}^m\sqrt{2\pi}}\int_{-\infty}^{\infty}\theta^2\,\exp\left[-\frac{(\theta-\overline{\theta}_1)^2}{2{\theta'_1}^{m2}}\right]\,d\theta}_{\frac{1}{2}\left[({\theta'_1}^2)^m + (\overline{\theta}_1^m)^2\right]}\\ - \frac{1}{2{\theta'_1}^m\sqrt{2\pi}}\underbrace{\int_{-\infty}^{\infty}\theta^2\operatorname{erf}\left(\frac{\theta-\overline{\theta}_{10}}{\sqrt{2}\theta'_{10}}\right)\exp\left[-\frac{(\theta-\overline{\theta}_1)^2}{2{\theta'_1}^{m2}}\right]\,d\theta}_{I_3}.\end{aligned} \tag{C.26}$$

By making the substitution $\theta_1 = \theta - \overline{\theta}_1^m$, I_3 becomes

$$I_3 = \int_{-\infty}^{\infty}\left[\theta_1^2 + 2\overline{\theta}_1^m\theta_1 + (\overline{\theta}_1^m)^2\right]\,\operatorname{erf}\left(\frac{\theta_1 + \overline{\theta}_1 - \overline{\theta}_{10}}{\sqrt{2}\theta'_{10}}\right)\exp\left[-\frac{\theta_1^2}{2{\theta'_1}^{m2}}\right]\,d\theta_1. \tag{C.27}$$

By using identities C.2, C.10 and C.16 (in appendices C.1, C.2 and C.3 respectively), we get

$$\begin{aligned}\frac{1}{2{\theta'_1}^m\sqrt{2\pi}}I_3 = &-\frac{1}{2}\left[({\theta'_1}^2)^m + (\overline{\theta}_1^m)^2\right]\operatorname{erf}\left(\frac{\overline{\theta}_{10}-\overline{\theta}_1}{\sqrt{2}\sqrt{{\theta'_{10}}^2+{\theta'_1}^2}}\right)\\ &+2\overline{\theta}_1\theta'_1\frac{1}{\sqrt{2\pi}}\sqrt{\frac{{\theta'_1}^2}{{\theta'_1}^2+{\theta'_{10}}^2}}\exp\left[-\frac{(\overline{\theta}_1-\overline{\theta}_{10})^2}{2({\theta'_1}^2+{\theta'_{10}}^2)}\right]\\ &+(\overline{\theta}_{10}^m-\overline{\theta}_1^m)\theta'_1\frac{1}{\sqrt{2\pi}}\left(\frac{{\theta'_1}^2}{{\theta'_1}^2+{\theta'_{10}}^2}\right)^{\frac{3}{2}}\exp\left[-\frac{(\overline{\theta}_1-\overline{\theta}_{10})^2}{2({\theta'_1}^2+{\theta'_{10}}^2)}\right].\end{aligned} \tag{C.28}$$

Integral C.26 is therefore given by

$$\begin{aligned}\int_{-\infty}^{\infty}\theta^2\Theta_{10}^m\,d\theta = &\frac{1}{2}\left[({\theta'_1}^2)^m + (\overline{\theta}_1^m)^2\right]\left[1-\operatorname{erf}\left(\frac{\overline{\theta}_1-\overline{\theta}_{10}}{\sqrt{2}\sqrt{{\theta'_1}^2+{\theta'_{10}}^2}}\right)\right]\\ &-2\overline{\theta}_1\theta'_1\frac{1}{\sqrt{2\pi}}\sqrt{\frac{{\theta'_1}^2}{{\theta'_1}^2+{\theta'_{10}}^2}}\exp\left[-\frac{(\overline{\theta}_1-\overline{\theta}_{10})^2}{2({\theta'_1}^2+{\theta'_{10}}^2)}\right]\\ &-(\overline{\theta}_{10}^m-\overline{\theta}_1^m)\theta'_1\frac{1}{\sqrt{2\pi}}\left(\frac{{\theta'_1}^2}{{\theta'_1}^2+{\theta'_{10}}^2}\right)^{\frac{3}{2}}\exp\left[-\frac{(\overline{\theta}_1-\overline{\theta}_{10})^2}{2({\theta'_1}^2+{\theta'_{10}}^2)}\right].\end{aligned} \tag{C.29}$$

Appendix D

Conditionally averaging high resolution data

By conditionally averaging resolved fields at cell centre values (based on the $w = 0\,\mathrm{ms}^{-1}$ fluid filter from equation 4.1, for example), we get a "zig-zag-like" boundary between fluids (see figure D.1.a). For the rising bubble test case in section 4, the resolved simulation has 200 cells in the horizontal, meaning the volume fraction (σ_i) will be incremented by factors of $1/200$ between vertical levels. These discontinuous jumps in volume fraction can cause noise in other fields, especially if these fields are dependent on the gradient of the mass or volume fraction. Here we propose a method for approximating the volume fraction for cells which intersect the fluid interface for smoother conditionally averaged volume fraction fields.

Let us assume that we have a cell with cell-centre position $\boldsymbol{x}_c$, vertical velocity w_c and gradient $\boldsymbol{\nabla} w$. The cell also has vertices $\boldsymbol{x}_{v,k}$, where k is the vertex index.

For a point on the surface of the fluid interface, $\boldsymbol{x}_w$, the following statement for the vertical velocity is true:

$$w(\boldsymbol{x}_w) = (\boldsymbol{x}_c - \boldsymbol{x}_w).\boldsymbol{\nabla} w = 0. \tag{D.1}$$

The above equation is satisfied using

$$\boldsymbol{x}_w = \boldsymbol{x}_c - w_c \frac{\boldsymbol{\nabla} w}{|\boldsymbol{\nabla} w|^2}. \tag{D.2}$$

The vertical velocities at the cell vertices are:

$$w(\boldsymbol{x}_{v_k}) = (\boldsymbol{x}_{v,k} - \boldsymbol{x}_w).\boldsymbol{\nabla} w. \tag{D.3}$$

If the product of any two vertex vertical velocities is negative (meaning a positive and negative w) then the fluid interface intersects the cell.

We calculate the distance of each vertex to the fluid interface using

$$d_k = \left| (\boldsymbol{x}_{v,k} - \boldsymbol{x}_w) . \frac{\boldsymbol{\nabla} w}{|\boldsymbol{\nabla} w|} \right| . \tag{D.4}$$

The mean distance of vertices with negative vertical velocities to the fluid interface is then

$$D_{w-} = \frac{1}{N_{w-}} \sum_{k \text{ where } w(\boldsymbol{x}_{v_k}) \leq 0} d_k, \tag{D.5}$$

and the mean distance of vertices with positive vertical velocities is

$$D_{w+} = \frac{1}{N_{w+}} \sum_{k \text{ where } w(\boldsymbol{x}_{v_k}) > 0} d_k, \tag{D.6}$$

where N_{w-} and N_{w+} are the number of vertices with negative and positive vertical velocities respectively. We can then use these mean distances to approximate the volume fraction of the cell:

$$\sigma_0 = \frac{D_{w-}}{D_{w-} + D_{w+}}, \tag{D.7}$$

$$\sigma_1 = \frac{D_{w+}}{D_{w-} + D_{w+}}. \tag{D.8}$$

Note that this is much simpler than calculating the volume each side of the interface for an arbitrary shaped cell.

Figure D.1 shows how the filter using equation D.7 (figure D.1.b) improves the smoothness of the conditionally averaged volume fraction field relative to the basic fluid filter from equation 4.1 (figure D.1.a). Figure D.2 compares the mass transfer analyses defined in section 4.1.4 using the standard $w = 0$ ms^{-1} filter (a) and the smoother filter (b). We note that there are sharp spikes in the diagnosed mass transfer profile in figure D.2.a (left). These spikes occur when a cell in the resolved simulation switches sign of the vertical velocity from time level n to $n + 1$, which causes a switch in fluid label for that cell. As there are only 200 cells in a horizontal layer, the change in the volume fraction is $\Delta\sigma_i = \pm 1/200$. This is a significant change when observing changes of the order 10^{-3} like in figure D.2.a. To counter this issue, we apply the smoother conditional averaging condition at the fluid boundaries using equation D.7 (figure D.2.b). The spikes above $z = 5$ km are no longer present, but the diagnosed transfer terms are still able to capture the movement of the fluid interfact in this region. Note that higher resolution single-fluid simulation could also be used for smoother conditionally averaged variables, but this would require a considerable increase in computational cost to achieve switches of σ_i less than 10^{-3}.

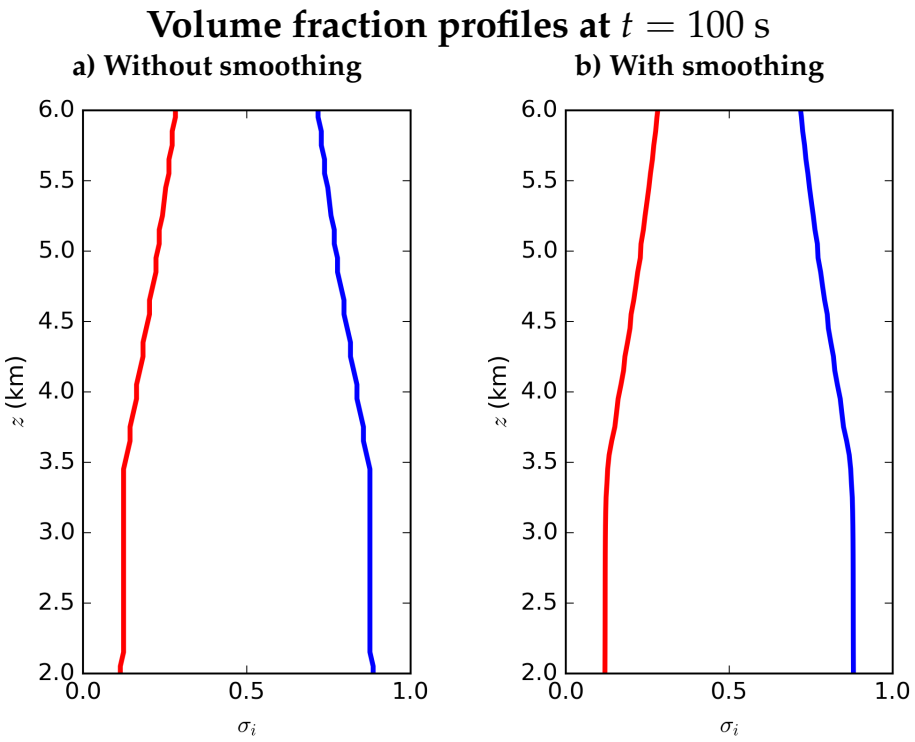

Figure D.1: The volume fraction fields for the conditionally averaged rising bubble test case at $t = 100$ s, where the downdraft volume fraction is given in blue and the updraft volume fraction in red. Panel a shows the volume fractions by using the $w = 0$ ms^{-1} filter only whereas smoothing has been applied in panel b (according to equation D.7) by approximating where the interface intersects the cells.

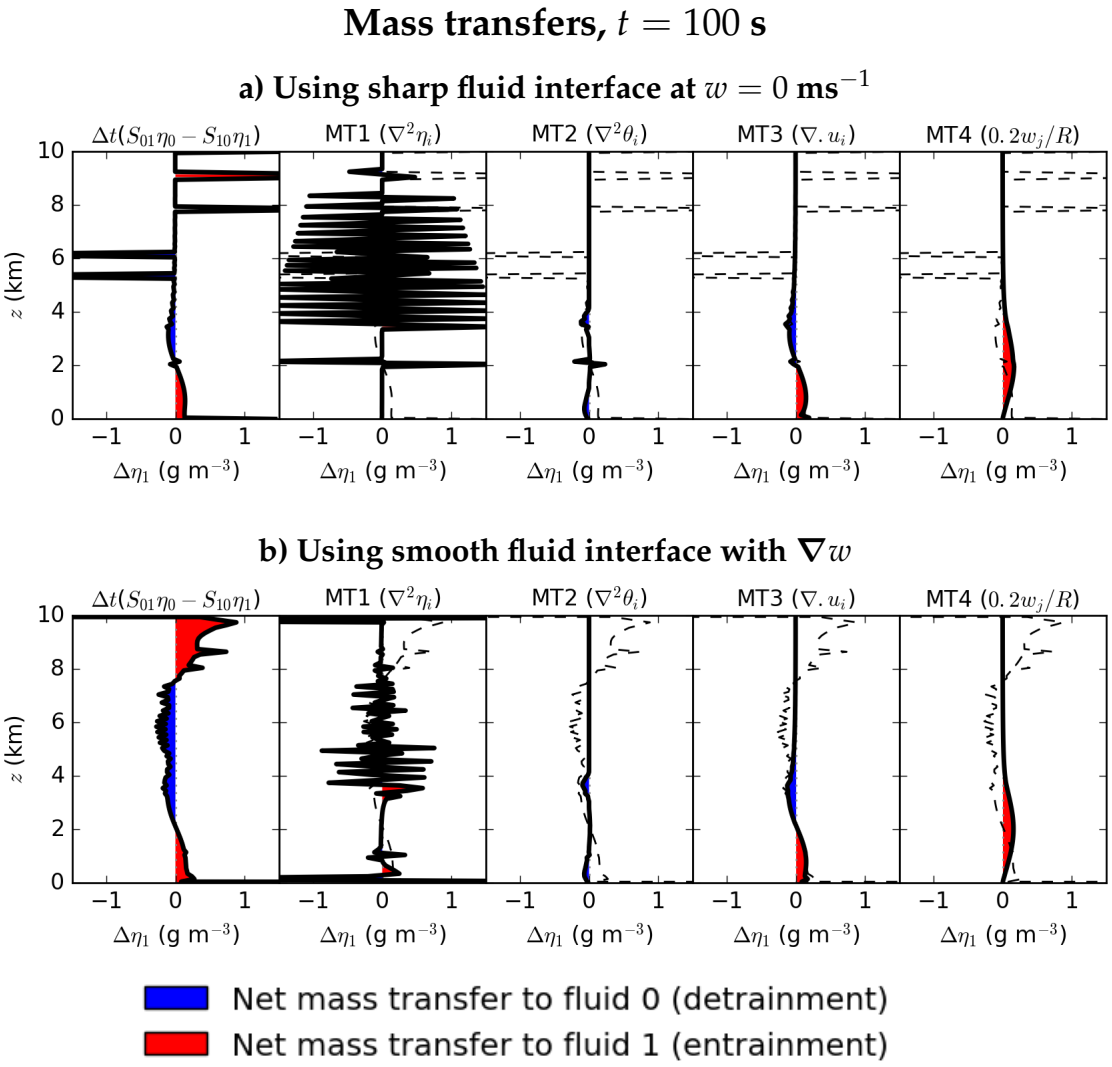

Figure D.2: The mass transfers for fluid 1 produced by MT1-MT4 over one timestep ($\Delta t = 1$ s) at various times. Also shown are the transfer needed to obtain the masses from the resolved filtered single-fluid test case (left). Gains in mass for fluids 0 and 1 are given by the blue and red regions respectively.

References

Ambaum, M., 2010: *Thermal Physics of the Atmosphere*. Advancing Weather and Climate Science, Wiley.

Arakawa, A., 2004: The cumulus parameterization problem: Past, present, and future. *Journal of Climate*, **17 (13)**, 2493–2525.

Arakawa, A., J.-H. Jung, and C.-M. Wu, 2011: Toward unification of the multiscale modeling of the atmosphere. *Atmospheric Chemistry and Physics*, **11 (8)**, 3731–3742.

Arakawa, A. and W. H. Schubert, 1974: Interaction of a cumulus cloud ensemble with the large-scale environment, part i. *Journal of the Atmospheric Sciences*, **31 (3)**, 674–701.

Arakawa, A. and C.-M. Wu, 2013: A unified representation of deep moist convection in numerical modeling of the atmosphere. part i. *Journal of the Atmospheric Sciences*, **70 (7)**, 1977–1992.

Baer, M. and J. Nunziato, 1986: A two-phase mixture theory for the deflagration-to-detonation transition (ddt) in reactive granular materials. *International journal of multiphase flow*, **12 (6)**, 861–889.

Bechtold, P., E. Bazile, F. Guichard, P. Mascart, and E. Richard, 2001: A mass-flux convection scheme for regional and global models. *Quarterly Journal of the Royal Meteorological Society*, **127 (573)**, 869–886.

Bechtold, P., N. Semane, P. Lopez, J.-P. Chaboureau, A. Beljaars, and N. Bormann, 2014: Representing equilibrium and nonequilibrium convection in large-scale models. *Journal of the Atmospheric Sciences*, **71 (2)**, 734–753.

Betts, A. and M. Miller, 1986: A new convective adjustment scheme. part ii: Single column tests using gate wave, bomex, atex and arctic air-mass data sets. *Quarterly Journal of the Royal Meteorological Society*, **112 (473)**, 693–709.

Betts, A. K., 1986: A new convective adjustment scheme. part i: Observational and theoretical basis. *Quarterly Journal of the Royal Meteorological Society*, **112 (473)**, 677–691.

Betts, A. K. and M. J. Miller, 1993: The betts-miller scheme. *The representation of cumulus convection in numerical models*, Springer, 107–121.

Bolton, T. and L. Zanna, 2019: Applications of deep learning to ocean data inference and subgrid parameterization. *Journal of Advances in Modeling Earth Systems*, **11 (1)**, 376–399.

Boutle, I., A. Finnenkoetter, A. Lock, and H. Wells, 2016: The london model: forecasting fog at 333 m resolution. *Quarterly Journal of the Royal Meteorological Society*, **142 (694)**, 360–371.

Bryan, G. H. and J. M. Fritsch, 2002: A benchmark simulation for moist nonhydrostatic numerical models. *Monthly Weather Review*, **130 (12)**, 2917–2928, doi:10.1175/1520-0493(2002)130¡2917:ABSFMN¿2.0.CO;2.

Chandrasekhar, S., 1961: *Hydrodynamic and hydromagnetic stability*. Oxford University Press.

Charney, J. G. and A. Eliassen, 1964: On the growth of the hurricane depression. *Journal of the Atmospheric Sciences*, **21 (1)**, 68–75.

Couvreux, F., F. Hourdin, and C. Rio, 2010: Resolved versus parametrized boundary-layer plumes. part i: A parametrization-oriented conditional sampling in large-eddy simulations. *Boundary-layer meteorology*, **134 (3)**, 441–458.

De Rooy, W. C., et al., 2013: Entrainment and detrainment in cumulus convection: An overview. *Quarterly Journal of the Royal Meteorological Society*, **139 (670)**, 1–19.

Deardorff, J., 1966: The counter-gradient heat flux in the lower atmosphere and in the laboratory. *Journal of the Atmospheric Sciences*, **23 (5)**, 503–506.

Donner, L. J., T. A. O'Brien, D. Rieger, B. Vogel, and W. F. Cooke, 2016: Are atmospheric updrafts a key to unlocking climate forcing and sensitivity? *Atmospheric Chemistry and Physics*, **16 (20)**, 12 983–12 992.

Dopazo, C., 1977: On conditioned averages for intermittent turbulent flows. *Journal of Fluid Mechanics*, **81 (3)**, 433–438, doi:10.1017/S0022112077002158.

Efstathiou, G. A., J. Thuburn, and R. J. Beare, 2019: Diagnosing coherent structures in the convective boundary layer by optimizing their vertical turbulent scalar transfer. *Boundary-Layer Meteorology*, 1–26.

Emanuel, K. A., 1994: *Atmospheric convection*. Oxford University Press on Demand.

Embid, P., J. Hunter, and A. Majda, 1992: Simplified asymptotic equations for the transition to detonation in reactive granular materials. *SIAM Journal on Applied Mathematics*, **52 (5)**, 1199–1237.

Fitch, A. C., 2019: An improved double-gaussian closure for the subgrid vertical velocity probability distribution function. *Journal of the Atmospheric Sciences*, **76 (1)**, 285–304.

Gentine, P., M. Pritchard, S. Rasp, G. Reinaudi, and G. Yacalis, 2018: Could machine learning break the convection parameterization deadlock? *Geophysical Research Letters*, **45 (11)**, 5742–5751.

Gerard, L. and J.-F. Geleyn, 2005: Evolution of a subgrid deep convection parametrization in a limited-area model with increasing resolution. *Quarterly Journal of the Royal Meteorological Society*, **131 (610)**, 2293–2312.

Gerard, L., J.-M. Piriou, R. Brožková, J.-F. Geleyn, and D. Banciu, 2009: Cloud and precipitation parameterization in a meso-gamma-scale operational weather prediction model. *Monthly Weather Review*, **137 (11)**, 3960–3977.

Gregory, D. and P. Rowntree, 1990: A mass flux convection scheme with representation of cloud ensemble characteristics and stability-dependent closure. *Monthly Weather Review*, **118 (7)**, 1483–1506.

Grell, G. A. and D. Dévényi, 2002: A generalized approach to parameterizing convection combining ensemble and data assimilation techniques. *Geophysical Research Letters*, **29 (14)**, 38–1.

Grell, G. A., S. R. Freitas, et al., 2014: A scale and aerosol aware stochastic convective parameterization for weather and air quality modeling. *Atmos. Chem. Phys*, **14 (10)**, 5233–5250.

Guelfi, A., et al., 2007: Neptune: a new software platform for advanced nuclear thermal hydraulics. *Nuclear Science and Engineering*, **156 (3)**, 281–324.

Guo, H., J.-C. Golaz, L. Donner, B. Wyman, M. Zhao, and P. Ginoux, 2015: Clubb as a unified cloud parameterization: Opportunities and challenges. *Geophysical Research Letters*, **42 (11)**, 4540–4547.

Han, J. and H.-L. Pan, 2011: Revision of convection and vertical diffusion schemes in the ncep global forecast system. *Weather and Forecasting*, **26 (4)**, 520–533.

Hanley, K., M. Whitall, A. Stirling, and P. Clark, 2019: Modifications to the representation of subgrid mixing in kilometre-scale versions of the unified model. *Quarterly Journal of the Royal Meteorological Society*.

Held, I. M., M. Zhao, and B. Wyman, 2007: Dynamic radiative–convective equilibria using gcm column physics. *Journal of the atmospheric sciences*, **64 (1)**, 228–238.

Holland, J. Z. and E. M. Rasmusson, 1973: Measurements of the atmospheric mass, energy, and momentum budgets over a 500-kilometer square of tropical ocean. *Mon. Wea. Rev*, **101 (1)**, 44–57.

Holloway, C. E., et al., 2014: Understanding and representing atmospheric convection across scales: Recommendations from the meeting held at dartington hall, devon, uk, 28–30 january 2013. *Atmospheric Science Letters*, **15 (4)**, 348–353.

Houghton, H. G. and H. E. Cramer, 1951: A theory of entrainment in convective currents. *Journal of Meteorology*, **8 (2)**, 95–102.

Kain, J. and J. Fritsch, 1992: The role of the convective "trigger function" in numerical forecasts of mesoscale convective systems. *Meteorology and Atmospheric Physics*, **49 (1-4)**, 93–106.

Kain, J. S. and J. M. Fritsch, 1990: A one-dimensional entraining/detraining plume model and its application in convective parameterization. *Journal of the Atmospheric Sciences*, **47 (23)**, 2784–2802.

Khairoutdinov, M., D. Randall, and C. DeMott, 2005: Simulations of the atmospheric general circulation using a cloud-resolving model as a superparameterization of physical processes. *Journal of the Atmospheric Sciences*, **62 (7)**, 2136–2154.

Khairoutdinov, M. F. and D. A. Randall, 2001: A cloud resolving model as a cloud parameterization in the ncar community climate system model: Preliminary results. *Geophysical Research Letters*, **28 (18)**, 3617–3620.

Khouider, B., J. Biello, A. J. Majda, et al., 2010: A stochastic multicloud model for tropical convection. *Communications in Mathematical Sciences*, **8 (1)**, 187–216.

Knight, C. G., et al., 2007: Association of parameter, software, and hardware variation with large-scale behavior across 57,000 climate models. *Proceedings of the National Academy of Sciences*, **104 (30)**, 12 259–12 264.

Kuell, V. and A. Bott, 2008: A hybrid convection scheme for use in non-hydrostatic numerical weather prediction models. *Meteorologische Zeitschrift*, **17 (6)**, 775–783.

Kwon, Y. C. and S.-Y. Hong, 2017: A mass-flux cumulus parameterization scheme across gray-zone resolutions. *Monthly Weather Review*, **145 (2)**, 583–598.

Lancz, D., B. Szintai, and R. Honnert, 2018: Modification of a parametrization of shallow convection in the grey zone using a mesoscale model. *Boundary-layer meteorology*, **169 (3)**, 483–503.

Landahl, M. T., E. Mollo-Christensen, and M. S. Korman, 1989: Turbulence and random processes in fluid mechanics. Acoustical Society of America.

Lappen, C.-L. and D. A. Randall, 2001: Toward a unified parameterization of the boundary layer and moist convection. part i: A new type of mass-flux model. *Journal of the atmospheric sciences*, **58 (15)**, 2021–2036.

Lean, H. W., P. A. Clark, M. Dixon, N. M. Roberts, A. Fitch, R. Forbes, and C. Halliwell, 2008: Characteristics of high-resolution versions of the met office unified model for forecasting convection over the united kingdom. *Monthly Weather Review*, **136 (9)**, 3408–3424, doi:10.1175/2008MWR2332.1.

Li, F., D. Rosa, W. D. Collins, and M. F. Wehner, 2012: "super-parameterization": A better way to simulate regional extreme precipitation? *Journal of Advances in Modeling Earth Systems*, **4 (2)**.

Lohmann, U., J. Feichter, C. C. Chuang, and J. E. Penner, 1999: Prediction of the number of cloud droplets in the echam gcm. *Journal of Geophysical Research: Atmospheres*, **104 (D8)**, 9169–9198.

Maher, P., G. K. Vallis, S. C. Sherwood, M. J. Webb, and P. G. Sansom, 2018: The impact of parameterized convection on climatological precipitation in atmospheric global climate models. *Geophysical Research Letters*, **45 (8)**, 3728–3736.

Malardel, S. and P. Bechtold, 2019: The coupling of deep convection with the resolved flow via the divergence of mass flux in the ifs. *Quarterly Journal of the Royal Meteorological Society*.

Manabe, S. and R. F. Strickler, 1964: Thermal equilibrium of the atmosphere with a convective adjustment. *Journal of the Atmospheric Sciences*, **21 (4)**, 361–385.

Matheou, G., D. Chung, L. Nuijens, B. Stevens, and J. Teixeira, 2011: On the fidelity of large-eddy simulation of shallow precipitating cumulus convection. *Monthly Weather Review*, **139 (9)**, 2918–2939.

McIntyre, W. A., H. Weller, and C. E. Holloway, 2020: Numerical methods for entrainment and detrainment in the multi-fluid euler equations for convection. *Quarterly Journal of the Royal Meteorological Society*, **146 (728)**, 1106–1120.

McTaggart-Cowan, R., et al., 2019: Modernization of atmospheric physics parameteriza-

tion in canadian nwp. *Journal of Advances in Modeling Earth Systems*.

Méchitoua, N., M. Boucker, J. Laviéville, J. Hérard, S. Pigny, and G. Serre, 2003: An unstructured finite volume solver for two-phase water-vapour flows based on an elliptic oriented fractional step method. *Proc. of The 10th International Topical Meeting on Nuclear Reactor Thermal-Hydraulics (NURETH-10), Seoul, Korea*.

Mellado, J.-P., C. Bretherton, B. Stevens, and M. Wyant, 2018: Dns and les for simulating stratocumulus: better together. *Journal of Advances in Modeling Earth Systems*, **10 (7)**, 1421–1438.

Mellor, G. L., 1977: The gaussian cloud model relations. *Journal of the Atmospheric Sciences*, **34 (2)**, 356–358.

Milbrandt, J. A., S. Bélair, M. Faucher, M. Vallée, M. L. Carrera, and A. Glazer, 2016: The pan-canadian high resolution (2.5 km) deterministic prediction system. *Weather and Forecasting*, **31 (6)**, 1791–1816.

Neggers, R., A. Siebesma, and H. Jonker, 2002: A multiparcel model for shallow cumulus convection. *Journal of the atmospheric sciences*, **59 (10)**, 1655–1668.

Ng, E. W. and M. Geller, 1969: A table of integrals of the error functions. *Journal of Research of the National Bureau of Standards B*, **73 (1)**, 1–20.

Nielsen, M. A., 2015: *Neural networks and deep learning*, Vol. 25. Determination press San Francisco, CA, USA:.

O'Gorman, P. A. and J. G. Dwyer, 2018: Using machine learning to parameterize moist convection: Potential for modeling of climate, climate change, and extreme events. *Journal of Advances in Modeling Earth Systems*, **10 (10)**, 2548–2563.

Pergaud, J., V. Masson, S. Malardel, and F. Couvreux, 2009: A parameterization of dry thermals and shallow cumuli for mesoscale numerical weather prediction. *Boundary-layer meteorology*, **132 (1)**, 83.

Petch, J., A. Brown, and M. Gray, 2002: The impact of horizontal resolution on the simulations of convective development over land. *Quarterly Journal of the Royal Meteorological Society: A journal of the atmospheric sciences, applied meteorology and physical oceanography*, **128 (584)**, 2031–2044.

Plant, R., 2010: A review of the theoretical basis for bulk mass flux convective parameterization. *Atmospheric Chemistry and Physics*, **10 (8)**, 3529–3544.

Plant, R. and G. C. Craig, 2008: A stochastic parameterization for deep convection based on equilibrium statistics. *Journal of the Atmospheric Sciences*, **65 (1)**, 87–105.

Rasp, S., M. S. Pritchard, and P. Gentine, 2018: Deep learning to represent subgrid processes in climate models. *Proceedings of the National Academy of Sciences*, **115 (39)**, 9684–9689.

Rayleigh, 1882: Investigation of the character of the equilibrium of an incompressible heavy fluid of variable density. *Proceedings of the London Mathematical Society*, **s1-14 (1)**, 170–177.

Ringler, T. D., J. Thuburn, J. B. Klemp, and W. C. Skamarock, 2010: A unified approach

to energy conservation and potential vorticity dynamics for arbitrarily-structured c-grids. *Journal of Computational Physics*, **229 (9)**, 3065–3090.

Satoh, M., B. Stevens, F. Judt, M. Khairoutdinov, S.-J. Lin, W. M. Putman, and P. Düben, 2019: Global cloud-resolving models. *Current Climate Change Reports*, 1–13.

Saurel, R. and R. Abgrall, 1999: A multiphase godunov method for compressible multifluid and multiphase flows. *Journal of Computational Physics*, **150 (2)**, 425–467.

Schneider, T., S. Lan, A. Stuart, and J. Teixeira, 2017: Earth system modeling 2.0: A blueprint for models that learn from observations and targeted high-resolution simulations. *Geophysical Research Letters*, **44 (24)**, 12–396.

Schroeder, D. V., 2000: *An introduction to thermal physics*. Pearson.

Sharp, D. H., 1983: Overview of rayleigh-taylor instability. Tech. rep., Los Alamos National Lab., NM (USA).

Shohat, J. A. and J. D. Tamarkin, 1943: *The problem of moments*. 1, American Mathematical Soc.

Siebesma, A. P., P. M. Soares, and J. Teixeira, 2007: A combined eddy-diffusivity mass-flux approach for the convective boundary layer. *Journal of the atmospheric sciences*, **64 (4)**, 1230–1248.

Simpson, J. and V. Wiggert, 1969: Models of precipitating cumulus towers. *Mon. Wea. Rev*, **97 (7)**, 471–489.

Soares, P., P. Miranda, A. Siebesma, and J. Teixeira, 2004: An eddy-diffusivity/mass-flux parametrization for dry and shallow cumulus convection. *Quarterly Journal of the Royal Meteorological Society: A journal of the atmospheric sciences, applied meteorology and physical oceanography*, **130 (604)**, 3365–3383.

Sommeria, G. and J. Deardorff, 1977: Subgrid-scale condensation in models of non-precipitating clouds. *Journal of the Atmospheric Sciences*, **34 (2)**, 344–355.

Stewart, H. B. and B. Wendroff, 1984: Two-phase flow: models and methods. *Journal of Computational Physics*, **56 (3)**, 363–409.

Stirling, A. and R. Stratton, 2012: Entrainment processes in the diurnal cycle of deep convection over land. *Quarterly Journal of the Royal Meteorological Society*, **138 (666)**, 1135–1149.

Stokes, G. M. and S. E. Schwartz, 1994: The atmospheric radiation measurement (arm) program: Programmatic background and design of the cloud and radiation test bed. *Bulletin of the American Meteorological Society*, **75 (7)**, 1201–1222.

Stull, R. B., 1988: *An Introduction to Boundary Layer Meteorology*, Vol. 13. Springer Science & Business Media.

Swann, H., 2001: Evaluation of the mass-flux approach to parametrizing deep convection. *Quarterly Journal of the Royal Meteorological Society*, **127 (574)**, 1239–1260.

Tan, Z., C. M. Kaul, K. G. Pressel, Y. Cohen, T. Schneider, and J. Teixeira, 2018: An extended eddy-diffusivity mass-flux scheme for unified representation of subgrid-scale turbulence and convection. *Journal of Advances in Modeling Earth Systems*.

Taylor, G. I., 1950: The instability of liquid surfaces when accelerated in a direction perpendicular to their planes. i. *Proceedings of the Royal Society of London. Series A. Mathematical and Physical Sciences*, **201 (1065)**, 192–196.

Thomson, W., 1871: Hydrokinetic solutions and observations. *The London, Edinburgh, and Dublin Philosophical Magazine and Journal of Science*, **42 (281)**, 362–377.

Thuburn, J., G. A. Efstathiou, and R. J. Beare, 2019: A two-fluid single-column model of the dry, shear-free, convective boundary layer. *Quarterly Journal of the Royal Meteorological Society*.

Thuburn, J. and G. K. Vallis, 2018: Properties of conditionally filtered equations: Conservation, normal modes, and variational formulation. *Quarterly Journal of the Royal Meteorological Society*, **144 (714)**, 1555–1571.

Thuburn, J., H. Weller, G. K. Vallis, R. J. Beare, and M. Whitall, 2018: A framework for convection and boundary layer parameterization derived from conditional filtering. *Journal of the Atmospheric Sciences*, **75 (3)**, 965–981.

Tiedtke, M., 1989: A comprehensive mass flux scheme for cumulus parameterization in large-scale models. *Monthly Weather Review*, **117 (8)**, 1779–1800.

von Helmholtz, H., 1868: *über discontinuirliche Flüssigkeits-Bewegungen*. Akademie der Wissenschaften zu Berlin.

Weller, H., W. McIntyre, and D. Shipley, 2020: Multifluids for representing subgrid-scale convection. *Journal of Advances in Modeling Earth Systems*, **12 (8)**, e2019MS001 966.

Weller, H. and W. A. McIntyre, 2019: Numerical solution of the conditionally averaged equations for representing net mass flux due to convection. *Quarterly Journal of the Royal Meteorological Society*, **145 (721)**, 1337–1353.

Willett, M. and M. Whitall, 2017: A simple prognostic based convective entrainment rate for the unified model: Description and tests. Tech. rep., Forecasting Research Tech. Rep. 617, Met Office.

Yanai, M., S. Esbensen, and J.-H. Chu, 1973: Determination of bulk properties of tropical cloud clusters from large-scale heat and moisture budgets. *Journal of the Atmospheric Sciences*, **30 (4)**, 611–627.

Yano, J.-I., F. Guichard, J.-P. Lafore, J.-L. Redelsperger, and P. Bechtold, 2004: Estimations of mass fluxes for cumulus parameterizations from high-resolution spatial data. *Journal of the atmospheric sciences*, **61 (7)**, 829–842.

Yano, J.-I. and R. Plant, 2012: Convective quasi-equilibrium. *Reviews of Geophysics*, **50 (4)**.

Yano, J.-I., et al., 2018: Scientific challenges of convective-scale numerical weather prediction. *Bulletin of the American Meteorological Society*, **99 (4)**, 699–710.

Youngs, D. L., 1989: Modelling turbulent mixing by rayleigh-taylor instability. *Physica D: Nonlinear Phenomena*, **37 (1-3)**, 270–287.